BEHAVIOR OF LAMINATED COMPOSITE STRUCTURES SUBJECTED TO LOW VELOCITY IMPACT

A Thesis Submitted to the

Graduate School of Natural and Applied Sciences of

Dokuz Eylül University

In Partial Fulfillment of the Requirements for

the Degree of Doctor of Philosophy in Mechanical Engineering, Mechanics Program

by

Züleyha ASLAN

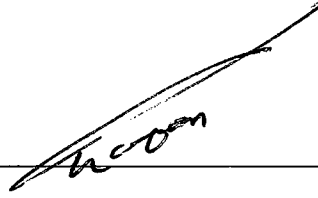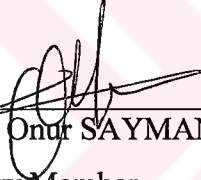January, 2002

İZMİR

Ph.D. THESIS EXAMINATION RESULT FORM

We certify that we have read the thesis, entitled **"Behavior of laminated composite structures subjected to low velocity impact"** completed by **Züleyha ASLAN** under supervision of **Assoc. Prof. Dr. Ramazan KARAKUZU** and that in our opinion it is fully adequate, in scope and in quality, as a thesis for the degree of Doctor of Philosophy.
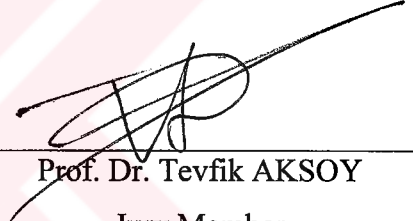
Assoc. Prof. Dr. Ramazan KARAKUZU

Supervisor
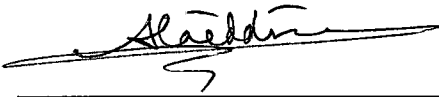
Prof. Dr. Onur SAYMAN

Jury Member

(Thesis Committee Member)

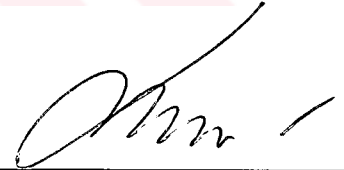Prof. Dr. Tevfik AKSOY

Jury Member

(Thesis Committee Member)

Prof. Dr. Alaeddin ARPACI

Jury Member

Prof. Dr. Sami AKSOY

Jury Member

Approved by the

Graduate School of Natural and Applied Sciences

Prof. Dr. Cahit HELVACI

Director

ACKNOWLEDGEMENTS

ABSTRACT

The purpose of this thesis is the evaluation of the dynamic behavior of fiber-reinforced laminated composites under low velocity impact. An experimental and numerical investigation has been carried out to study the transient response of E-glass/epoxy composite. The numerically computed contact force history is compared with the same experimental results. The importance of the impact velocity, the impactor mass, the dimensions and the thickness of the composite plate are determined for laminated composites subjected to low velocity impact.

A vertical drop-weight testing machine is developed in the Mechanical Laboratory for the low velocity impact test. Affixed to the drop-weight device, a piezoelectric force transducer, localized in the hemispherical impactor nose, yields the complete force versus time history of the impact event. Impact tests are performed at increasing impact velocities 1 m/sec, 2 m/sec and 3 m/sec, and impactor masses of 135 g and 2600 g. The studies have been carried out with plate dimensions of 150 mm by 150 mm, 150 mm by 100 mm and 150 mm by 50 mm with two opposite sides clamped and the other two free and the impact load is applied at the center of each plate. Unidirectional and woven fiber form is selected for laminated composite materials with different stacking sequence.

A numerical evaluation of these specimens is also carried out by using 3DIMPACT transient dynamic finite element analysis code. The contact force between the impactor and the composite plate, maximum transverse deflection at the center of the plate, stresses and strains during impact are plotted, as functions of time and the predicted delamination sizes of composites are determined numerically. Finally, results are obtained by numerical simulation and experimental testing of the dynamic behavior of composite material and an approach to the problem of optimum design of composite plates subjected to low velocity impact is presented.

ÖZET

Bu tezin amacı, düşük hızlı darbeye maruz fiber takviyeli tabakalı kompozitlerin dinamik davranışını değerlendirmektir. Cam fiber/epoksi kompozitinin zamana bağlı analizi üzerine deneysel ve nümerik araştırma yapılmıştır. Nümerik olarak hesaplanan temas kuvveti-zaman değerleri, deneysel sonuçlar ile karşılaştırılmıştır. Düşük hızlı darbeye maruz tabakalı kompozitlerde darbe hızının, darbe kütlesinin, kompozit plağın boyutlarının ve kalınlığının önemi belirlenmiştir.

Düşey konumlandırılmış bir ağırlık düşürme test makinası, düşük hızlı darbe testleri yapmak üzere Mekanik Laboratuvarında geliştirilmiştir. Ağırlık düşürme cihazının yarı küresel uçlu kafa kısmına yerleştirilmiş bir piezoelektrik kuvvet ölçer darbe esnasındaki kuvvet-zaman diagramını verir. Darbe testleri 1 m/sn, 2 m/sn ve 3 m/sn' lik artan darbe hızlarında ve 135 g ve 2600 g'lık darbe kütlelerinde yapılmıştır. Karşılıklı iki tarafı ankastre ve diğer iki tarafı serbest olan 150 mm'ye 150 mm, 150 mm'ye 100 mm ve 150 mm'ye 50 mm'lik plak boyutları ile deneyler yapılmıştır ve darbe yükü her bir plağın merkezine uygulanmıştır. Farklı yığılım dizilerine sahip tabakalı kompozit malzemelerde tek yönlü ve örgü fiber formu seçilmiştir.

Zamana bağlı dinamik sonlu eleman analizi yapabilen 3DIMPACT programını kullanarak tabakalı kompozitlerin nümerik değerlendirmesi de yapılmıştır. Kompozit plak ve vurucu kafa arasındaki temas kuvveti, plağın merkezindeki maksimum düşey yerdeğiştirme, darbe esnasındaki gerilmeler ve birim şekil değişimleri zamanın fonksiyonu olarak elde edilmiş ve numerik hesaplamalarla kompozit tabakaların ayrışma büyüklükleri belirlenmiştir. Sonuç olarak, kompozit malzemenin dinamik davranışı üzerine deneysel testler ve nümerik simülasyon ile sonuçlar elde edilmiş ve düşük hızlı darbeye maruz kompozit plakların optimum dizayn problemine bir yaklaşım sunulmuştur.

CONTENTS

Chapter One

INTRODUCTION

Chapter Two

MACROMECHANICAL BEHAVIOR OF A LAMINATE

Chapter Three
NUMERICAL PROCEDURE

Chapter Four
MATERIAL

Chapter Five
IMPACT TESTING APPARATUS

Chapter Six
RESULTS AND DISCUSSION

Chapter Seven
CONCLUSIONS AND RECOMMENDATIONS

Chapter Eight
REFERENCES

Chapter Nine
APPENDIXES

LIST OF TABLES

LIST OF FIGURES

CHAPTER ONE
INTRODUCTION

1.1 Overview

Composite laminates are used in many engineering applications, which expose them impact by foreign objects. Impact-induced damage may arise during manufacture, maintenance and service operation. An example of in-service impact occurs during aircraft takeoffs and landings, when stones and other small debris from the runway are propelled at high velocities by the tires. During the manufacturing process or during maintenance, tools can be dropped on the structure. In this case, impact velocities are small but the mass of the projectile is larger. Laminated composite structures are more susceptible to impact damage than a similar metallic structure. In composite structures, impacts create internal damage that often cannot be detected by visual inspection. This internal damage can cause severe reductions in strength and can grow under load. Therefore, the effects of foreign object impacts on composite structures must be understood, and proper measures should be taken in the design process to account for these expected events. Concerns about the effects of impacts on the performance of composite structures have been a factor in limiting the use of composite materials. For these reasons, the problem of low velocity impact of composite structures represents significant practical and theoretical interest.

Numerous experimental and analytical techniques have been developed to study the dynamic response of composite structures subjected to transient dynamic loading. Some of the prominent work in this area is briefly mentioned in the following. The first attempts to characterize composite materials under dynamic loading were carried out by Rotem & Lifshitz (1971), Lifshitz (1976), and Sierakowski et al. (1971). Sierakowski & Chaturvedi (1997) and Abrate (1998) bring the developments in various testing methods and impact modeling.

Theoretical calculations have been carried out to predict the impact response. Sun & Chattopadhyay (1975) and Dobyns (1981) used the plate equations developed by Whitney & Pagano (1970) to analyze a simply supported, specially orthotropic plate subjected to central impact. Green (1992,1993) employed wave propagation theory to evaluate the stress field under impact. Christoforou & Yiğit (1996) studied the transverse impact of a simply supported composite beam using the momentum balance method. Sankar (1992) presented semi-empirical formulae for predicting impact characteristics such as peak force, contact duration, and peak strain on back surface. Qian & Swanson (1990) used a Rayleigh-Ritz procedure to obtain an approximate solution for the impact response of rectangular plates with clamped edges.

Low velocity impact response of laminated plates was investigated analytically by Ramkumar & Chen (1982), Sun & Jih (1995) and Abatan et al. (1998). An approximate solution for the prediction of plate response to low velocity impact was presented by Gong & Lam (1999). This solution includes the combined action of the plate and stiffeners as well as the effects of the contact and transverse shear deformation. The response of hybrid laminated composite plates subjected to low velocity impact was investigated using shear deformation theory by Lee et al. (1997). Kim & Kang (2001) developed a new analytical method for predicting the impact force from the dynamic strain of composite plates subjected to transverse impact. For this, two assumptions were introduced in their study. Firstly, the impact force and dynamic strain can be separated into frequency and amplitude. Secondly, the amplitude of the impact force corresponds to that of the dynamic strain at any frequency.

Goo & Kim (1997) studied dynamic contact analysis of laminated composite plates under low-velocity impact. Simple laws, such as the modified Hertz contact law, have been used to impose the dynamic contact condition of composite laminates. An analytical model for the impact response of laminated composite plates was presented by Pierson & Vaziri (1996). The governing equations, which apply to small deflection elastic response of specially orthotropic laminates, include

the combined effects of shear deformation, rotary inertia, and the nonlinear Hertzian contact law.

Theoretical and experimental work has also been conducted. Lal (1982, 1983) performed an experimental and analytical study on the transverse impact behavior of graphite/epoxy laminates. The large deflection theory of plates was used to predict the load deflection characteristics during the impact event. A simple energy dissipation model was developed to predict the residual strength of the specimens after impact. Kistler & Waas (1998) investigated impact response of cylindrically curved laminates including a large deformation scaling. Results from a nonlinear analysis and experimental drop weight impact tests were evaluated in their studies. Their parametric study identifies impact energy and momentum scaling relationships with mass and velocity. Dynamic responses of composite sandwich plate impacted by a rigid ball were investigated numerically and experimentally by Lee et al. (1993). A refined formulation of composite sandwich plate was employed to study the dynamic response of impacted sandwich plate. Wang & Vukhanh (1994) investigated low velocity impact in carbon fiber, PEEK cross ply laminates using two simple approaches.

Various researchers have developed the three dimensional finite element models to investigate impact. Incorporating the work of Yang & Sun (1982) and Tan & Sun (1985), Chen & Sun (1985) studied impact on flat laminates under initial stress using the finite element method with a Newmark time integration algorithm. The merit of this three-dimensional numerical model is that it can provide the detailed information about the local stresses and strains under impactor, which are key factors to produce initial damages in materials. Thereby, it is possible to capture the formation of impact-induced damages, if very fine mesh is used. The drawback of this approach is that its computational demands can be exorbitant as pointed out by Davies & Zhang (1995).

Besant et al. (2001) studied finite element modeling of low velocity impact of composite sandwich panels. Their study outlines a finite element procedure for

predicting the behavior under low velocity impact of sandwich panels consisting of brittle composite skins supported by a ductile core. Belingardi et al. (1998) studied numerical simulation of fragmentation of composite material plates due to impact. A new method for simple prediction of the impact force history on composite laminates subjected to low-velocity impact was proposed by Choi & Hong (1994). Frequency characteristics of the numerical impact force history were investigated from modal analysis and compared with the natural frequencies of the system in which the mass of an impactor was lumped with the plate.

Finite element procedures were used in conjunction with a numerical algorithm to compute the impact response of a graphite-epoxy laminated beam subjected to tensile initial stresses by Sankar & Sun (1985). The effect of initial stresses on the contact duration, impact force, coefficient of restitution, and bending and shear stresses were evaluated. Chandrashekhara et al. (1998) developed a method of determining the contact force on laminated composite plates subjected low velocity impact using the finite element method and a neural network. Birman et al. (1996) presented an approach to the problem of optimum design of composite plates subjected to low-velocity impact. The deflections and stresses are reduced by employing prestrained shape memory alloy (SMA) fibers which are in the martensitic phase when embedded within the plate. Sun & Liou (1989) investigated laminated composite plates under impact dynamic loading using a three-dimensional hybrid stress finite element method.

Finite element analysis of a laminated composite plate subjected to circularly distributed central impact loading was carried out by Aggour & Sun (1988). A finite element displacement model, which includes the effects of transverse shear deformation and rotary inertia, was used along with Hamilton's principle to drive the finite element matrices. Three dimensional finite element and dynamic analysis of composite laminate subjected to impact was made by Lee et al. (1984). Central difference method was employed in their analysis.

Finite element analysis were conducted to analyze the dynamic response of an unbalanced sandwich beam, a balanced sandwich beam, and a balanced sandwich plate subject to a low energy impact by Kwon & Wojcik (1998). The nonlinear impact response of laminated composite cylindrical and doubly curved shells was analyzed using a modified Hertzian contact law by Chandrashekhara & Schroeder (1995). A finite element model was developed based on Sander's shell theory and includes shear deformation effects and non-linearity due to large deflection in their studies.

Some simple, but efficient theoretical and energetic approximation methods have also been presented to deal with this problem [(Cairns & Lagece, 1989), (Christoforou & Swanson, 1991)]. While these methods can provide the accurate global impact response behavior of composite laminates and employ a small amount of numerical computation, its extension for tackling more complex problems becomes very difficult.

Numerous researchers have used instrumented impact test apparatus to study the impact characteristics of different laminated composites. Chang & Sun (1989) determined the dynamic impact forces on a composite laminate by using experimentally generated Green's functions and signal deconvolutions. Jih & Sun (1993) studied experimentally prediction of delamination in composite laminates subjected to low velocity impact. They found that the results of the drop weight impact tests indicated that low velocity impact-induced delamination could be predicted by using the static interlaminar fracture toughness in conjunction with the static linear beam model. Doyle (1987) and Prasad et al. (1994) have determined the contact force history from strain gauge measurements.

An experimental technique for time-resolved characterization of the mechanical response and induced damage of fiber-reinforced composite laminates during low-velocity transverse impact was presented by Park et al (2000). Their configuration uses a three-point bend fixture in a split Hopkinson pressure bar (SHPB) apparatus for controlled loading and real-time diagnosis. The impact energy absorption

characteristics of glass epoxy composites and glass polyester composites with respect to fiber volume fraction were investigated by the instrumented Charpy impact test method by Lee & Cheon (2001). Using their experimental results, the impact absorption characteristics of glass fiber composites such as fiber breakage and fiber pull-out and delamination were evaluated.

The behavior of different E-glass/epoxy laminated composites plates has been experimentally studied under impact of aluminum projectile at low velocities (0.53-3.1 m/sec) by Mili & Necib (2001). They used a drop weight impact machine and evaluated the effects of the projectile velocities and lamination sequences on composite plates behavior. Mantena et al. (2001) described a test methodology used for characterizing different glass-resin composite systems with respect to their low-velocity impact response, dynamic modulus and inherent damping properties.

Experimental impact data for a carbon fiber reinforced polymer were presented showing damage modes produced by different specimen dynamic response to impact by Bland & Dear (2001). Real time observations of the impact events have provided an insight into the impact processes that are a key to explaining the damage inflicted for different impact conditions in their studies. Rydin & Karbhari (1998) studied partitioning energy during low-velocity impact of RTM fiber-reinforced composites. Investigation of instrumented drop tower impact of resin transfer molded composite plates indicates that the initial reaction to dynamic out-of plane loading was well behaved until decoupling commences between local and global plate reactions.

An experimental investigation has been carried out to study the dynamic behavior of composite profiles made by pultrusion by Chotard & Benzeggagh (1998). The resulting data from the drop-weight tests provide specific information about the effect of the impactor velocity, the impactor mass and the impactor nose radius, all of which have a great influence on the impact response of these profiles. Scarponi et al. (1996) evaluated the behavior of fiber-reinforced composites and sandwich panels for aeronautical applications under impact. Experimental tests were performed on several specimen configurations, based on different quasi-isotropic lay-up and

materials such CFRP, CFRTP and a syntactic foam as the core of sandwich panels. Wu & Shyu (1993) presented experimental results for contact and low-velocity impact responses of composite laminates by rigid spheres.

Low velocity impact tests were performed on graphite-fabric/epoxy specimens of various thicknesses, with an instrumented drop-weight apparatus by Caprino et al. (1999). From the load/displacement curves recorded during impact, the influence of material thickness on the main parameters involved in the impact phenomenon was evaluated. Siow & Shim (1998) presented an experimental study of several parameters that govern the impact response of a woven carbon-fiber epoxy laminate subjected to low velocity impact.

The damage of composite structures to impact events is one of the most important aspects of behavior that inhibits more widespread application of composite materials. Understanding the deformation and damage mechanisms involved in the impact of composite targets is important in the effective design of a composite structure. A prerequisite for increasing the use of composite materials is the need to predict damage from low velocity impact.

Many researchers have employed experimental and numerical approaches to evaluate impact damage to composite materials [(Kim & Sham, 2000), (Naik et al., 2000), (Hou et al., 2000), (Davies et al., 1996), (Joshi & Sun, 1985), (Sohn et al., 2000), (Sjögren et al., 2001), (Hu et al., (1999)]. An integrated modeling and testing procedure for carbon/epoxy composite plates has been developed to evaluate the impact damage initiation and propagation by Luo et al. (1999). Analytical models were suggested for prediction of impact damage initiation and growth during quasi-static response caused by large impactors by Olsson (2001). The critical load for delamination growth was found almost insensitive to geometry and boundary conditions and the critical energy for delamination growth was separated in bending, shear and indentation contributions in his study. An experimental investigation to establish data for validation of residual strength models for impacted composite panels was carried out Asp et al. (2001).

Delamination due to low-velocity impact of simply supported graphite/epoxy cross-ply laminate beams and plates was investigated by Razi & Kobayashi (1993). Both quasi-static and low-velocity impact testing were carried out in their studies. For each loading condition, finite element analysis and experiments were performed to study damage growth and distributions. The delamination process in thin composite plates subjected to low-velocity impact was simulated using a specially developed 2D cohesive/volumetric finite element scheme by Geubelle & Baylor (1998). Cohesive elements were introduced along the boundaries of the inner layers and inside the transverse plies to simulate the spontaneous initiation and propagation of transverse matrix cracks and delamination fronts.

Freitas et al. (2000) studied numerical evaluation of failure mechanisms on composite specimens subjected to impact loading. Their results showed that the delaminated area due to impact loading depends on the number of interfaces between plies. Nonlinear finite element analysis was used for the estimation of damage due to low velocity impact loading of laminated composite circular plates by Sridhar & Rao (1995). A numerical model based on the finite element displacement method that includes the effects of transverse shear deformation and a failure algorithm that describes the energy dissipation during the impact damage process has been developed by Oguibe & Webb (1999). Choi et al. (1991 b) used the dynamic finite element method coupled with failure analysis to predict threshold of impact damage and initiation of delamination.

1.2 Objectives and Scope of the Present Research

The impact behavior of composite materials has been studied with different scientific approaches and on different materials. The influence of impact and material parameters on the composite laminate response is one of these approaches. These parameters are numerous and hard to discriminate. Examples of these parameters are the impact velocity, specimen-stacking sequence, impactor mass, specimen geometry, impactor size or the impact energy.

The determination of the contact force on laminated composite plates subjected to low velocity impact is the focus of the present study. The effect of impact velocity and impactor mass is evaluated. In addition, the importance of the in plane dimensional and thickness effect of the composite structure is evaluated. Since there are a few numbers of investigations regarding the performance of composite materials and structures at different sizes [(Liu et al., 1998), (Batdorf, 1989), (Found et al., 1997) and (Shadid et al., 1995)], it has been concluded that the size effects should be carefully examined in material characterizations and structural designs.

Most of the work has been carried out on laminated structures or plates made up of high performance composite materials such as carbon/epoxy or kevlar/epoxy. However, a few numbers of studies have dealt with the mechanical behavior of E-glass/fiber reinforced laminated composite materials subjected to impact loading. Therefore, the present study is mainly concerned with E-glass/epoxy laminated composites.

In this study, the impact tests are conducted with a vertical drop-weight testing machine developed in the Mechanical Laboratory. A numerical evaluation of laminated E-glass/epoxy composite is carried out using 3DIMPACT transient dynamic finite element analysis code from F.K. Chang [(Choi & Chang, 1992), (Choi et al., 1991 b), (Wu & Chang, 1989)]. This computer code was made by Hyung Yun Choi & Fu-Kuo Chang at the Department of Aeronautics and Astronautics in Stanford University and modified by Seng Guan Lee & Iqbal Shadid.

The importance of the impact velocity, impactor mass, in-plane dimensional and thickness effects of the composite structure are evaluated. The transient contact forces between the impactor and the laminated composite plate, stresses and strains during impact and the maximum transverse deflection at the center are found. The delamination shape and sizes of laminated E-glass/epoxy composites resulting from point-nose impact are predicted numerically.

CHAPTER TWO

MACROMECHANICAL BEHAVIOR OF A LAMINATE

2.1 Introduction

A laminate is a collection of laminae stacked to achieve the desired stiffness and thickness. For example, unidirectional fiber-reinforced laminae can be stacked so that the fibers in each lamina are oriented in the same or different directions as seen in Figure 2.1. The sequence of various orientations of a fiber-reinforced composite layer in a laminate is termed the lamination scheme or stacking sequence. The layers are usually bonded together with the same matrix material as that in a lamina.
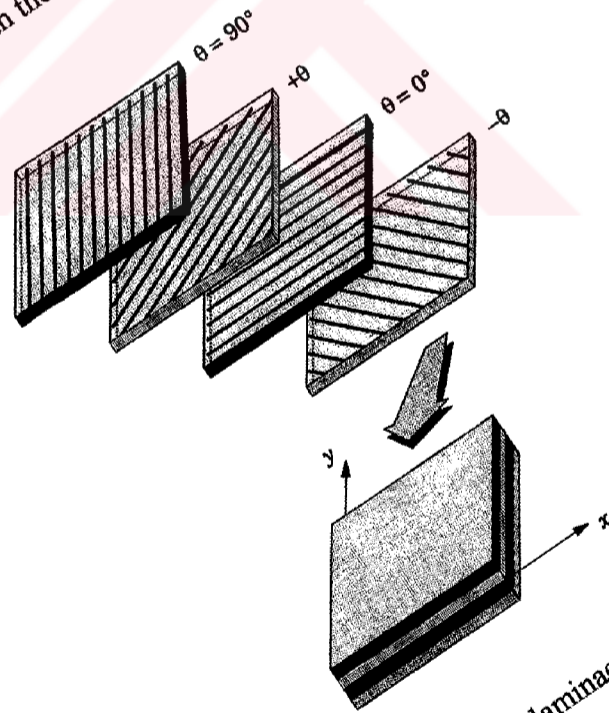
Figure 2.1 A laminate made up of laminae with different fiber orientations.

A unidirectional laminate (i.e., all laminae have the same fiber orientation) will be very strong along the fiber direction and weak in the transverse direction. The laminate will be weak in shear also. If a laminate has layers with fibers oriented at 30^0 or 45^0, it can take shear loads. The lamination scheme and material properties of individual lamina provide an added flexibility to designers to tailor the stiffness and strength of the laminate to match the structural requirements. Laminated composite structures also have disadvantages. Because of the mismatch of material properties between layers, the shear stresses produced between the layers, especially at the edges of a laminate, may cause delamination.

2.2 Constitutive Equations of a Lamina

2.2.1 Generalized Hooke's Law

In formulating the constitutive equations of a lamina it is assumed that:
(i)   a lamina is a continuum, i.e., no gaps or empty spaces exist.
(ii)   a lamina behaves as a linear elastic material.
The generalized Hooke's law for an anisotropic material under isothermal conditions is given by

$$\sigma_{ij} = C_{ijkl}\varepsilon_{kl} \tag{2.1}$$

or in contracted notation

$$\sigma_i = C_{ij}\varepsilon_j \tag{2.2}$$

where σ_{ij} (σ_i) are the stress components, ε_{ij} (ε_i) are the strain components, and C_{ij} are the material coefficients, all referred to an orthogonal Cartesian coordinate system (x_1,x_2,x_3) fixed in the body. Often fiber-reinforced lamina are characterized as orthotropic, i.e., the material has three orthogonal planes of material symmetry. If the coordinate planes are chosen parallel to the three orthogonal planes of material symmetry, the stress-strain relations and strain-stress relations can be written as

12

$$\begin{Bmatrix} \sigma_1 \\ \sigma_2 \\ \sigma_3 \\ \sigma_4 \\ \sigma_5 \\ \sigma_6 \end{Bmatrix} = \begin{bmatrix} C_{11} & C_{12} & C_{13} & 0 & 0 & 0 \\ C_{12} & C_{22} & C_{23} & 0 & 0 & 0 \\ C_{13} & C_{23} & C_{33} & 0 & 0 & 0 \\ 0 & 0 & 0 & C_{44} & 0 & 0 \\ 0 & 0 & 0 & 0 & C_{55} & 0 \\ 0 & 0 & 0 & 0 & 0 & C_{66} \end{bmatrix} \begin{Bmatrix} \varepsilon_1 \\ \varepsilon_2 \\ \varepsilon_3 \\ \varepsilon_4 \\ \varepsilon_5 \\ \varepsilon_6 \end{Bmatrix} \qquad \begin{aligned} \sigma_1 &= \sigma_{11} \\ \sigma_2 &= \sigma_{22} \\ \sigma_3 &= \sigma_{33} \\ \sigma_4 &= \sigma_{23} \\ \sigma_5 &= \sigma_{13} \\ \sigma_6 &= \sigma_{12} \end{aligned} \qquad (2.3)$$

$$\begin{Bmatrix} \varepsilon_1 \\ \varepsilon_2 \\ \varepsilon_3 \\ \varepsilon_4 \\ \varepsilon_5 \\ \varepsilon_6 \end{Bmatrix} = \begin{bmatrix} S_{11} & S_{12} & S_{13} & 0 & 0 & 0 \\ S_{12} & S_{22} & S_{23} & 0 & 0 & 0 \\ S_{13} & S_{23} & S_{33} & 0 & 0 & 0 \\ 0 & 0 & 0 & S_{44} & 0 & 0 \\ 0 & 0 & 0 & 0 & S_{55} & 0 \\ 0 & 0 & 0 & 0 & 0 & S_{66} \end{bmatrix} \begin{Bmatrix} \sigma_1 \\ \sigma_2 \\ \sigma_3 \\ \sigma_4 \\ \sigma_5 \\ \sigma_6 \end{Bmatrix} \qquad \begin{aligned} \varepsilon_1 &= \varepsilon_{11} \\ \varepsilon_2 &= \varepsilon_{22} \\ \varepsilon_3 &= \varepsilon_{33} \\ \varepsilon_4 &= 2\varepsilon_{23} \\ \varepsilon_5 &= 2\varepsilon_{13} \\ \varepsilon_6 &= 2\varepsilon_{12} \end{aligned} \qquad (2.4)$$

where S_{ij} denote the compliance coefficients, $[S] = [C]^{-1}$.

A unidirectional fiber-reinforced lamina is treated as an orthotropic material whose material symmetry planes are parallel and transverse to the fiber direction. The material coordinate axis x_1 is taken to be parallel to the fiber, the x_2-axis transverse to the fiber direction in the plane of the lamina, and the x_3-axis is perpendicular to the plane of the lamina (see Figure 2.2). The orthotropic material properties of a lamina are obtained either by the theoretical approach or by laboratory testing.
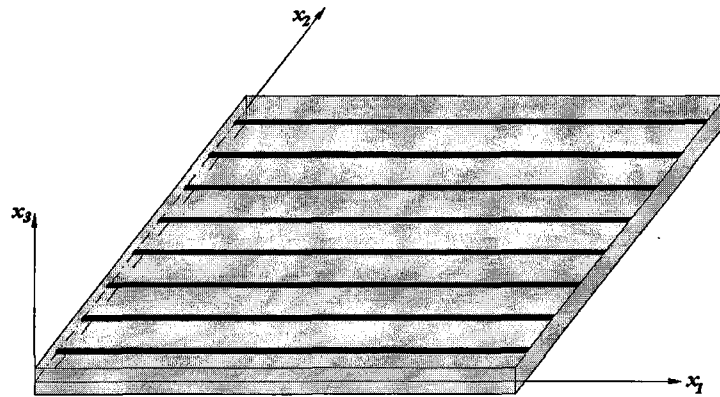
Figure 2.2 A unidirectional fiber-reinforced lamina with the material coordinate system (x_1, x_2, x_3).

2.2.2 Engineering Constants of Orthotropic Materials

The constitutive equations for a material which has three orthogonal planes of material property symmetry (i.e., orthotropic materials), referred to the principal material directions, are given by Eq. (2.3) and (2.4). The material stiffness coefficients C_{ij} can be expressed in terms of engineering constants, i.e., Young's moduli, Poisson's ratios, and shear moduli. The strain-stress relations can be expressed in matrix form, using the single-subscript notation, as

$$
\begin{Bmatrix} \varepsilon_1 \\ \varepsilon_2 \\ \varepsilon_3 \\ \varepsilon_4 \\ \varepsilon_5 \\ \varepsilon_6 \end{Bmatrix} =
\begin{bmatrix}
\dfrac{1}{E_1} & \dfrac{-\upsilon_{21}}{E_2} & \dfrac{-\upsilon_{31}}{E_3} & 0 & 0 & 0 \\
\dfrac{-\upsilon_{12}}{E_1} & \dfrac{1}{E_2} & \dfrac{-\upsilon_{32}}{E_3} & 0 & 0 & 0 \\
\dfrac{-\upsilon_{13}}{E_1} & \dfrac{-\upsilon_{23}}{E_2} & \dfrac{1}{E_3} & 0 & 0 & 0 \\
0 & 0 & 0 & \dfrac{1}{G_{23}} & 0 & 0 \\
0 & 0 & 0 & 0 & \dfrac{1}{G_{13}} & 0 \\
0 & 0 & 0 & 0 & 0 & \dfrac{1}{G_{12}}
\end{bmatrix}
\begin{Bmatrix} \sigma_1 \\ \sigma_2 \\ \sigma_3 \\ \sigma_4 \\ \sigma_5 \\ \sigma_6 \end{Bmatrix}
\qquad (2.5)
$$

Comparing Eq.(2.5) with Eq. (2.4), we conclude that the 6x6 matrix in Eq. (2.5) is the compliance matrix $[S]$. Since the compliance matrix $[S]$ is the inverse of the stiffness matrix $[C]$ in Eq. (2.3), and because the inverse of a symmetric matrix is symmetric, it follows that the compliance matrix $[S]$ is also a symmetric matrix.

2.3 Transformation of Stresses and Strains

The coordinate system used in the solution of a problem, in general, does not coincide with the material coordinate system. Further, composite laminates have several layers, each with different orientation of their material coordinates with respect to the laminate coordinates. Thus, there is a need to establish transformation relations among stresses and strains in one coordinate system to the corresponding quantities in another coordinate system. These relations can be used to transform

constitutive equations from the material coordinates to the coordinates used in the solution of a problem.

Let (x,y,z) denote the coordinates used in the solution of a problem, and let (x_1,x_2,x_3) be the principal material coordinates such that (x_1,x_2,x_3) is obtained from (x,y,z) by rotating the xy-plane counterclockwise (when looking down on the lamina) by an angle θ about the z-axis (see Figure 2.3). Conversely, (x,y,z) is obtained from (x_1,x_2,x_3) by rotating the x_1x_2-plane clockwise by an angle θ.

The relationship between the components of stress in the two coordinate systems is given by

$$\begin{Bmatrix} \sigma_{xx} \\ \sigma_{yy} \\ \sigma_{zz} \\ \sigma_{yz} \\ \sigma_{xz} \\ \sigma_{xy} \end{Bmatrix} = \begin{bmatrix} \cos^2\theta & \sin^2\theta & 0 & 0 & 0 & -2\sin\theta\cos\theta \\ \sin^2\theta & \cos^2\theta & 0 & 0 & 0 & 2\sin\theta\cos\theta \\ 0 & 0 & 1 & 0 & 0 & 0 \\ 0 & 0 & 0 & \cos\theta & \sin\theta & 0 \\ 0 & 0 & 0 & -\sin\theta & \cos\theta & 0 \\ \sin\theta\cos\theta & -\sin\theta\cos\theta & 0 & 0 & 0 & \cos^2\theta - \sin^2\theta \end{bmatrix} \begin{Bmatrix} \sigma_1 \\ \sigma_2 \\ \sigma_3 \\ \sigma_4 \\ \sigma_5 \\ \sigma_6 \end{Bmatrix} \qquad (2.6)$$

or

$$\{\sigma\}_p = [T]\{\sigma\}_m \qquad (2.7)$$
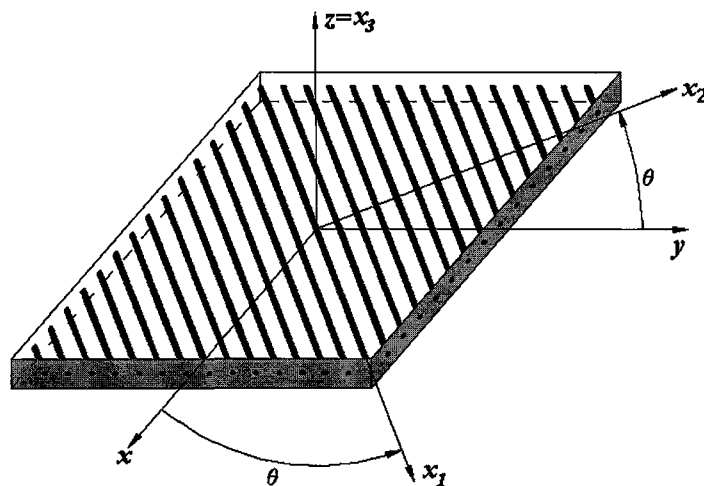
Figure 2.3 A fiber-reinforced lamina with global and material coordinate systems.

$\{\sigma_{ij}\}_m$ are the components of the stress tensor in the material coordinates, whereas $\{\sigma_{ij}\}_p$ are the components of the same stress tensor in the problem coordinates.

The inverse relationship between $\{\sigma\}_m$ and $\{\sigma\}_p$ is given by

$$\begin{Bmatrix} \sigma_1 \\ \sigma_2 \\ \sigma_3 \\ \sigma_4 \\ \sigma_5 \\ \sigma_6 \end{Bmatrix} = \begin{bmatrix} \cos^2\theta & \sin^2\theta & 0 & 0 & 0 & 2\sin\theta\cos\theta \\ \sin^2\theta & \cos^2\theta & 0 & 0 & 0 & -2\sin\theta\cos\theta \\ 0 & 0 & 1 & 0 & 0 & 0 \\ 0 & 0 & 0 & \cos\theta & -\sin\theta & 0 \\ 0 & 0 & 0 & \sin\theta & \cos\theta & 0 \\ -\sin\theta\cos\theta & \sin\theta\cos\theta & 0 & 0 & 0 & \cos^2\theta-\sin^2\theta \end{bmatrix} \begin{Bmatrix} \sigma_{xx} \\ \sigma_{yy} \\ \sigma_{zz} \\ \sigma_{yz} \\ \sigma_{xz} \\ \sigma_{xy} \end{Bmatrix} \quad (2.8)$$

or

$$\{\sigma\}_m = [R]\{\sigma\}_p \quad\quad\quad (2.9)$$

where $[R] = [T]^{-1}$

Slight modification of the results in Eq. (2.6) and (2.8) will yield the proper relations for the engineering components of strains. We have

$$\begin{Bmatrix} \varepsilon_1 \\ \varepsilon_2 \\ \varepsilon_3 \\ \varepsilon_4 \\ \varepsilon_5 \\ \varepsilon_6 \end{Bmatrix} = \begin{bmatrix} \cos^2\theta & \sin^2\theta & 0 & 0 & 0 & \sin\theta\cos\theta \\ \sin^2\theta & \cos^2\theta & 0 & 0 & 0 & -\sin\theta\cos\theta \\ 0 & 0 & 1 & 0 & 0 & 0 \\ 0 & 0 & 0 & \cos\theta & -\sin\theta & 0 \\ 0 & 0 & 0 & \sin\theta & \cos\theta & 0 \\ -2\sin\theta\cos\theta & 2\sin\theta\cos\theta & 0 & 0 & 0 & \cos^2\theta-\sin^2\theta \end{bmatrix} \begin{Bmatrix} \varepsilon_{xx} \\ \varepsilon_{yy} \\ \varepsilon_{zz} \\ 2\varepsilon_{yz} \\ 2\varepsilon_{xz} \\ 2\varepsilon_{xy} \end{Bmatrix}$$

$$(2.10)$$

$$\{\varepsilon\}_p = [R]^T\{\varepsilon\}_m \quad\quad\quad (2.11)$$

$$\{\varepsilon\}_m = [T]^T\{\varepsilon\}_p \quad\quad\quad (2.12)$$

2.4 Transformation of Material Coefficients

The stress and strain transformation equations in (2.7), (2.9) and (2.10);

$$\{\sigma\}_p = [T]\{\sigma\}_m = [T][C]_m\{\varepsilon\}_m = [T][C]_m[T]^T\{\varepsilon\}_p \qquad (2.13)$$

where $[C]_m$ is the 6x6 material stiffness matrix in the material coordinates and $[T]$ is the transformation matrix defined in Eq. (2.7). Using Hooke's law in the problem coordinate system, we can write

$$\{\sigma\}_p = [C]_p\{\varepsilon\}_p \qquad (2.14)$$

Hence, it follows from Eq. (2.13) and (2.14) that ($[C]_p \equiv [\bar{C}]$ and $[C]_m \equiv [C]$)

$$[\bar{C}] = [T][C][T]^T \qquad (2.15)$$

Eq. (2.15) is valid for general constitutive matrix $[C]$ (i.e., for orthotropic as well as anisotropic). The transformed compliance coefficients $\bar{S}_{ij}$, referred to the (x,y,z) system, are related to the compliance coefficients S_{ij} in the material coordinates by Eq. (2.16) as follows:

$$[\bar{S}] = [R]^T[S][R] \qquad (2.16)$$

In general, for the kth layer of a laminate, the stress-strain relations in the laminate coordinate system can be written as (Reddy, 1997);

$$\{\sigma\}_p^{(k)} = [\bar{C}]^{(k)}\{\varepsilon\}_p^{(k)} \qquad (2.17)$$

$$\{\varepsilon\}_p^{(k)} = [\bar{S}]^{(k)}\{\sigma\}_p^{(k)} \qquad (2.18)$$

CHAPTER THREE

NUMERICAL PROCEDURE

3.1 Introduction

The numerical investigation of the response of laminated composite plate is carried out using 3DIMPACT computer code. A transient dynamic finite element analysis is used for studying the dynamic characteristics of laminated composite plates due to transverse foreign object impact. By using this computer code, numerous solutions could be generated for laminated composite plates with arbitrary ply orientations and thicknesses subjected to transverse impact.

The analysis can be used to calculate the contact force between the impactor and composite laminate, maximum transverse deflection at the center of composite plate during impact and the transient stress and strain distributions through the laminate thickness. Moreover, the computer code allows evaluation of delamination areas by means of suitable stress analysis and damage criteria.

An 8-point brick element with incompatible modes is used for numerical investigation. The direct Gauss quadrature integration scheme is used through the element thickness to account for the change in material properties from layer to layer within the element. The Newmark scheme is adopted to perform time integration from step to step. A contact law incorporated with the Newton-Raphson method is applied to calculate the contact force during impact. The analysis of stresses and strains in the laminates is based on 3-dimensional linear elasticity with the consideration that, in each layer, the materials are homogeneous and orthotropic.

3.2 Transient Dynamic Analysis

3.2.1 Statement of the Problem

Consider a rectangular plate (length L, width W, and thickness h) made of a continuous fiber-reinforced, organic matrix composite (Figure 3.1). The plate consists of N plies or laminae. Ply orientation is arbitrary and need not be symmetric with respect to the mid-surface of the plate. The plies need not be made of the same material, different plies may have different properties. Perfect bonding between each ply is assumed. The plate is supported along its two edges. Each edge may be either clamped or simply supported.

A solid object of mass m and velocity V impacts the center of the plate. The radius of the nose of the impactor is r (Figure 3.1). It is desired to determine the transient dynamic response of the plate during impact and to calculate the stresses and strains as functions of time inside the laminate.
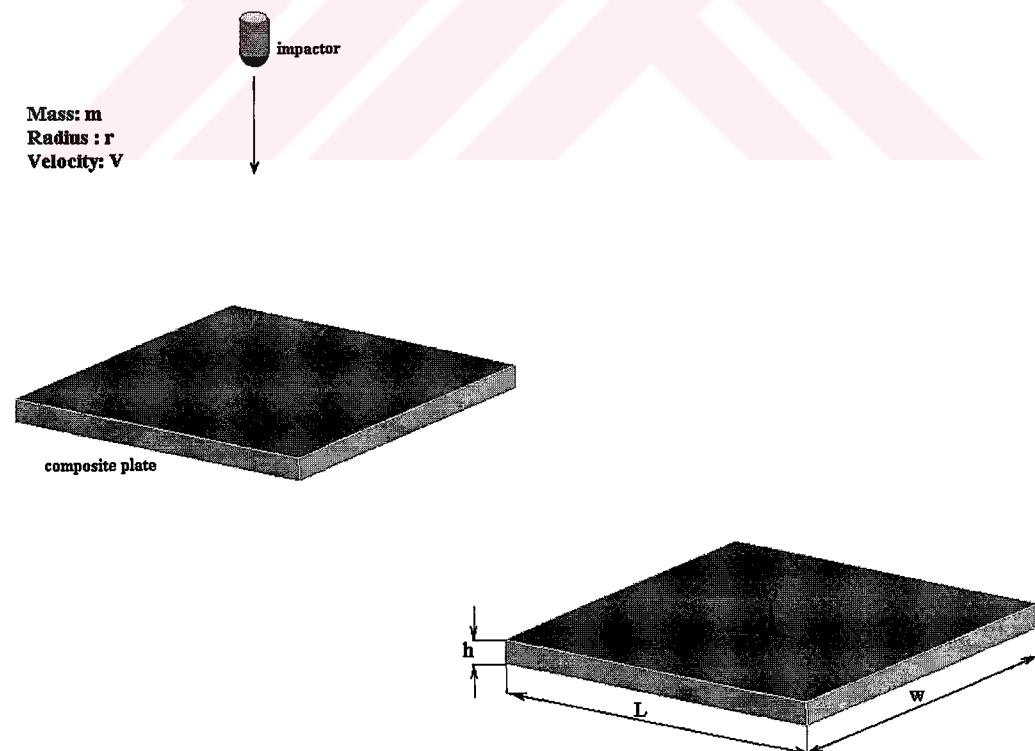
Figure 3.1 Description of the problem and the coordinate system.

3.2.2 Analysis

The analysis of stresses and strains in the laminates is based on 3-dimensional linear elasticity with the consideration that, in each layer, the materials are homogeneous and orthotropic. Accordingly, the equilibrium equations at instant *time=t* in variational form can be expressed as

$$0 = \int_{\Omega} w_i \rho u_{i,tt} dv + \int_{\Omega} e_{ij} E_{ijkl} \varepsilon_{kl} dv - \int_{\Gamma} w_i \sigma_{ij} n_j dA \qquad (3.1)$$

where σ_{ij} are the stresses, ε_{kl} are the strains, ρ is the density, $u_{i,tt}$ are the accelerations $(u_{i,tt} = \partial^2 u_i / \partial t^2)$, w_i are the arbitrary variational displacements, e_{ij} are the strains from the arbitrary variational displacements, Ω is the entire plate volume, Γ is the surface of the plate, n_j is the outward unit normal vector on the plate surface, and E_{ijkl} are the material properties of the laminates, which vary from layer to layer according to the ply orientation of the laminate.

In order to solve Eq. (3.1), the distribution of the contact force between the impactor and the impacted laminate has to be known first. The projectile is modeled as an elastic body with a spherical nose as shown in Figure 3.1. The contact force distribution during impact is simulated according to loading and unloading processes.

Upon loading (the contact force is increased), the contact force distribution is determined using the Hertzian contact law. Thus, the contact force can be related to the indentation depth α (the distance between the center of the projectile's nose and the mid-surface of the plate) by the expression

$$F = \kappa \alpha^{1.5} \qquad (3.2)$$

where κ is the modified constant of the Hertz contact theory proposed by Yang & Sun (1981).

$$\kappa = \frac{4}{3}\sqrt{r} \frac{1}{\left[(1-\nu_s^2)/E_s + 1/E_{yy}\right]} \qquad (3.3)$$

where r, ν_s, and E_s are the local radius, the Poisson's ratio, and the Young's modulus of the impactor respectively. E_{yy} is the transverse modulus normal to the fiber direction in the uppermost composite layer.

Upon unloading, the contact force is simulated by the following relation developed by Yang & Sun (1981).

$$f = f_m \left[\frac{\alpha - \alpha_0}{\alpha_m - \alpha_0}\right]^{2.5} \qquad (3.4)$$

where f_m is the maximum contact force just before unloading, α_m is the maximum indentation corresponding to f_m, and α_0 is the permanent indentation during this loading/unloading process. The permanent indentation can be determined from the following expressions

$$\alpha_0 = 0 \qquad \qquad \text{when } \alpha_m < \alpha_{cr}$$

$$\alpha_0 = \alpha_m \left[1 - \left(\frac{\alpha_{cr}}{\alpha_m}\right)^{2/5}\right] \qquad \text{when } \alpha_m \geq \alpha_{cr} \qquad (3.5)$$

where α_{cr} is the critical indentation, and is approximately 0.004 in. for glass/epoxy and 0.00316 in. for graphite/epoxy .

3.2.3 Finite Element Formulation

The stresses and strains in the laminates are calculated by a three-dimensional, transient, finite element method. The equations used in the numerical calculations are presented here.

3.2.3.1 Finite Element Model

In the finite element analysis, 8-node brick element is used (Figure 3.2). This type of element is found previously to be suitable for three-dimensional stress analyses of plates under transient conditions. To improve the accuracy in calculating the bending stiffnesses and the interlaminar shear stresses, and to minimize computer time, incompatible modes, introduced by Wilson et al. (1973), are added to the brick element shape functions. Thus, the displacements at any point in the laminate (u_1, u_2, u_3) are expressed as

$$u_q = \sum_{r=1}^{8} N_r u_{qr} + \sum_{s=1}^{3} S_s a_{qs} \qquad q = 1,2,3 \tag{3.6}$$

where u_{qr} are the displacements of nodal point r, and a_{qs} are variables of the incompatible modes in the x_q direction. The shape functions of the 8-node brick elements N_r ($r = 1{\sim}8$) and the shape functions of the incompatible modes S_s ($s=1{\sim}3$) are

$$N_1 = (1+\xi)(1+\eta)(1+\zeta)/8$$

$$N_2 = (1-\xi)(1+\eta)(1+\zeta)/8$$

$$N_3 = (1-\xi)(1-\eta)(1+\zeta)/8$$

$$N_4 = (1+\xi)(1-\eta)(1+\zeta)/8$$

$$N_5 = (1+\xi)(1+\eta)(1-\zeta)/8$$

$$N_6 = (1-\xi)(1+\eta)(1-\zeta)/8$$

$$N_7 = (1-\xi)(1-\eta)(1-\zeta)/8$$

$$N_8 = (1+\xi)(1-\eta)(1-\zeta)/8$$

$$S_1 = (1-\xi^2), \quad S_2 = (1-\eta^2), \quad S_3 = (1-\zeta^2) \tag{3.7}$$

ξ, η, and ζ are the natural coordinates for each element (Figure 3.2) whose values vary from -1 to $+1$. The coordinates (x_1, x_2, x_3) of any point inside the element are related to the natural coordinates through the shape functions

$$x_q = \sum_{r=1}^{8} N_r x_{qr} \qquad\qquad q = 1,2,3 \qquad\qquad (3.8)$$

where x_{qr} are the coordinates of nodal point r.

From Eq. (3.6) the strains at any point in the laminate can be written as

$$\{\varepsilon_{11} \quad \varepsilon_{22} \quad \varepsilon_{33} \quad 2\varepsilon_{23} \quad 2\varepsilon_{13} \quad 2\varepsilon_{12}\}^T = \{\varepsilon_{11} \quad \varepsilon_{22} \quad \varepsilon_{33} \quad \gamma_{23} \quad \gamma_{13} \quad \gamma_{12}\}^T$$

$$= \sum_{r=1}^{8} [B_r]\{u_{1r} \quad u_{2r} \quad u_{3r}\}^T + \sum_{s=1}^{3} [G_s]\{a_{1s} \quad a_{2s} \quad a_{3s}\}^T \qquad (3.9)$$

where ε_{11}, ε_{22} and ε_{33} are the normal strains, ε_{23}, ε_{13} and ε_{12} are the components of shear strain tensor, and γ_{23}, γ_{13} and γ_{12} are the engineering shear strains. The symbols $\{\ \}$ and $[\ ]$ represent vectors and matrices, respectively. The superscript T means transposition of a vector or a matrix. The $[B_r]$ and $[G_s]$ matrices are defined as

$$[B_r] = \begin{bmatrix} N_{r,1} & 0 & 0 & 0 & N_{r,3} & N_{r,2} \\ 0 & N_{r,2} & 0 & N_{r,3} & 0 & N_{r,1} \\ 0 & 0 & N_{r,3} & N_{r,2} & N_{r,1} & 0 \end{bmatrix}^T \quad r=1\sim8 \qquad (3.10)$$

$$[G_s] = \begin{bmatrix} S_{s,1} & 0 & 0 & 0 & S_{s,3} & S_{s,2} \\ 0 & S_{s,2} & 0 & S_{s,3} & 0 & S_{s,1} \\ 0 & 0 & S_{s,3} & S_{s,2} & S_{s,1} & 0 \end{bmatrix}^T \quad s=1\sim3 \qquad (3.11)$$
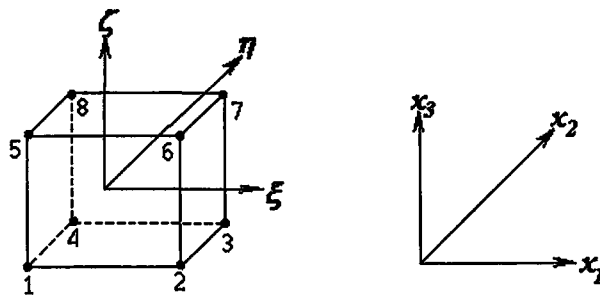
Figure 3.2 Schematic representation of the 8-node brick element.

The symbols $N_{r,i}$ and $S_{s,i}$ represent the derivates of the shape functions with respect to x_i ($N_{r,i} = \partial N_r / \partial x_i$, and $S_{s,i} = \partial S_s / \partial x_i$).

The stresses are related to the strains by the relation

$$\sigma_i = D_{ij}\varepsilon_j \qquad i,j=1\sim6 \tag{3.12}$$

D_{ij} is the elasticity matrix, which depends on the material properties and the ply orientation of the lamina. In writing Eq. (3.12) the following contracted notations are used:

$$\{\sigma_1 \quad \sigma_2 \quad \sigma_3 \quad \sigma_4 \quad \sigma_5 \quad \sigma_6\}^T \equiv \{\sigma_{11} \quad \sigma_{22} \quad \sigma_{33} \quad \tau_{23} \quad \tau_{13} \quad \tau_{12}\}^T \tag{3.13}$$

$$\{\varepsilon_1 \quad \varepsilon_2 \quad \varepsilon_3 \quad \varepsilon_4 \quad \varepsilon_5 \quad \varepsilon_6\}^T \equiv \{\varepsilon_{11} \quad \varepsilon_{22} \quad \varepsilon_{33} \quad \gamma_{23} \quad \gamma_{13} \quad \gamma_{12}\}^T \tag{3.14}$$

3.2.3.2 Governing Equations

By neglecting damping, the governing equation can be written as

$$[M]\{\ddot{d}\} + [K]\{d\} = \{F\} \tag{3.15}$$

where $[M]$ and $[K]$ are the mass and stiffness matrices, and $\{F\}, \{d\}$ and $\{\ddot{d}\}$ are the force, displacement and acceleration vectors, respectively.

The mass matrix $[M]$ is the sum of the element mass matrices $[M^e]$

$$[M] = \sum_{e=1}^{N_{el}} [M^e] \tag{3.16}$$

where N_{el} is the number of total elements. The element mass matrix is the sum of the element mass submatrices

$$\left[M^e\right] = \sum_{p=1}^{8}\sum_{r=1}^{8} \left[M^e\right]_{pr} \qquad\qquad (3.17)$$

In general, the element mass submatrices are

$$\left[M^e\right]_{pr} = \int_{V^e}\left[B_p\right]^T \rho\left[B_r\right]dv \quad p,r = 1{\sim}8 \qquad\qquad (3.18)$$

where V^e is the volume of the element, and ρ is the ply density. For computational convenience, it is assumed that the mass of the element is lumped equally in the nodal points. With this assumption the element mass matrices become

$$\left[M^e\right] = \frac{\rho V^e}{8}[I] \qquad\qquad (3.19)$$

where $[I]$ is a 24x24 unit matrix.

The stiffness matrix $[K]$ is the sum of the modified element stiffness matrices $[K^e]$ due to the incompatible modes

$$[K] = \sum_{e=1}^{N_{el}}\left[K^e\right] \qquad\qquad (3.20)$$

The modified element stiffness matrix is

$$\left[K^e\right] = \left[K^e_{dd}\right] - \left[K^e_{da}\right]\left[K^e_{aa}\right]^{-1}\left[K^e_{ad}\right] \qquad\qquad (3.21)$$

$\left[K^e_{dd}\right], \left[K^e_{aa}\right],$ and $\left[K^e_{ad}\right]$ are the sum of the element stiffness submatrices

$$\left[K^e_{dd}\right] = \sum_{p=1}^{8}\sum_{r=1}^{8} \left[K^e_{dd}\right]_{pr} \qquad\qquad (3.22)$$

$$[K_{da}^e] = \sum_{p=1}^{8} \sum_{\beta=1}^{3} [K_{da}^e]_{p\beta} \tag{3.23}$$

$$[K_{ad}^e] = \sum_{\alpha=1}^{3} \sum_{r=1}^{8} [K_{ad}^e]_{\alpha r} \tag{3.24}$$

$$[K_{aa}^e] = \sum_{\alpha=1}^{3} \sum_{\beta=1}^{3} [K_{aa}^e]_{\alpha\beta} \tag{3.25}$$

where

$$[K_{dd}^e]_{pr} = \int_{V^e} [B_p]^T [D][B_r] \mathrm{dv} \qquad p,r = 1 \sim 8 \tag{3.26}$$

$$[K_{da}^e]_{p\beta} = \int_{V^e} [B_p]^T [D][G_\beta] \mathrm{dv} \qquad p = 1 \sim 8 \ ; \ \beta = 1 \sim 3 \tag{3.27}$$

$$[K_{ad}^e]_{\alpha r} = \int_{V^e} [B_\alpha]^T [D][G_r] \mathrm{dv} \qquad \alpha = 1 \sim 3 \ ; \ r = 1 \sim 8 \tag{3.28}$$

$$[K_{aa}^e]_{\alpha\beta} = \int_{V^e} [G_\alpha]^T [D][G_\beta] \mathrm{dv} \qquad \alpha, \beta = 1 \sim 3 \tag{3.29}$$

The elasticity matrix $[D]$ in Eq. (3.26)-(3.29) depends on the material properties and the orientations of the plies through the thickness of the element. When the material properties and ply orientations are the same, the matrix $[D]$ in Eq. (3.26)-(3.29) remains constant during the integration process. If the material properties of ply orientations are different through the thickness of the element, elasticity matrix $[D]$ is a function of x_3 coordinate. Eq. (3.26)-(3.29) can be written explicitly as

$$[K_{dd}^e]_{pr} = \iint \left\{ \sum_{n=1}^{n_{ply}} \int_{x_3^n (bottom)}^{x_3^n (top)} [B_p]^T [D]_n [B_r] \mathrm{d}x_3 \right\} \mathrm{d}x_1 \mathrm{d}x_2 \qquad p,r = 1 \sim 8 \tag{3.30}$$

$$[K_{da}^e]_{p\beta} = \iint \left\{ \sum_{n=1}^{n_{ply}} \int_{x_3^n (bottom)}^{x_3^n (top)} [B_p]^T [D]_n [G_\beta] \mathrm{d}x_3 \right\} \mathrm{d}x_1 \mathrm{d}x_2 \qquad p = 1 \sim 8; \ \beta = 1 \sim 3 \tag{3.31}$$

$$[K_{ad}^e]_{\alpha r} = \iint \left\{ \sum_{n=1}^{n_{ply}} \int_{x_3^n (bottom)}^{x_3^n (top)} [B_\alpha]^T [D]_n [G_r] \mathrm{d}x_3 \right\} \mathrm{d}x_1 \mathrm{d}x_2 \qquad \alpha = 1 \sim 3; \ r = 1 \sim 8 \tag{3.32}$$

$$[K_{aa}^e]_{\alpha\beta} = \iint \left\{ \sum_{n=1}^{n_{ply}} \int_{x_3^n (bottom)}^{x_3^n (top)} [G_\alpha]^T [D]_n [G_\beta] \mathrm{d}x_3 \right\} \mathrm{d}x_1 \mathrm{d}x_2 \qquad \alpha, \beta = 1 \sim 3 \tag{3.33}$$

where n_{ply} is the number of plies of the element. x_3^n (bottom) and x_3^n (top) are the x_3 coordinates of the bottom and top of the nth ply. The elasticity matrix of the nth ply is $[D]_n$. The coordinates x_1, x_2, and x_3 are transformed and integrated in ξ, η, and ζ natural coordinates.

Eq.(3.21) is derived for static conditions by Taylor et al. (1976). As is shown in the following, it is also applicable to transient problems.

Application of the incompatible modes in transient problems

In transient problems, the equilibrium equations for each element can be written as

$$\begin{bmatrix} M^e & 0 \\ 0 & 0 \end{bmatrix} \begin{Bmatrix} \ddot{d}^e \\ \ddot{a}^e \end{Bmatrix} + \begin{bmatrix} K_{dd}^e & K_{da}^e \\ K_{ad}^e & K_{aa}^e \end{bmatrix} \begin{Bmatrix} d^e \\ a^e \end{Bmatrix} = \begin{Bmatrix} F^e \\ 0 \end{Bmatrix}$$

(3.34)

or

$$[M^e]\begin{Bmatrix} \ddot{d}^e \end{Bmatrix} + [K_{dd}^e]\{d^e\} + [K_{da}^e]\{a^e\} = \{F^e\}$$

(3.35)

$$[K_{ad}^e]\{d^e\} + [K_{aa}^e]\{a^e\} = 0$$

(3.36)

From Eq. (3.36),

$$\{a^e\} = -[K_{aa}^e]^{-1}[K_{ad}^e]\{d^e\}$$

(3.37)

By substituting Eq. (3.37) into Eq. (3.35),

$$[M^e]\begin{Bmatrix} \ddot{d}^e \end{Bmatrix} + ([K_{dd}^e] - [K_{da}^e][K_{aa}^e]^{-1}[K_{ad}^e])\{d^e\} = \{F^e\}$$

(3.38)

$[K^e]$ is defined as

$$[K^e] = [K^e_{dd}] - [K^e_{da}][K^e_{aa}]^{-1}[K^e_{ad}]$$ (3.39)

Then Eq. (3.38) becomes

$$[M^e]\left\{\ddot{d}^e\right\} + [K^e]\{d^e\} = \{F^e\}$$ (3.40)

With the present problem, the only load is the contact force caused by the impactor. It is defined a scalar force f which is a point force acting perpendicular to the plate at the contact point and has a magnitude equal to the contact force. The contact force vector $\{F\}$ is then written as

$$\{F\} = f\{U\}$$ (3.41)

$\{U\}$ is a unit vector whose component is -1 in the direction of the contact force. All other components of $\{U\}$ are zero.

At time $t+\Delta t$, Eq.(15) is written as

$$[M]\left\{\ddot{d}\right\}^{t+\Delta t} + [K]\{d\}^{t+\Delta t} = \{F\}^{t+\Delta t}$$ (3.42)

where the superscript refers to time. The Newmark method will be employed to obtain the solutions to this equation. Accordingly, the velocity and acceleration vectors at time $t+\Delta t$ are written as

$$\left\{\dot{d}\right\}^{t+\Delta t} = \left\{\dot{d}\right\}^{t} + (1-\lambda)\Delta t\left\{\ddot{d}\right\}^{t} + \lambda\Delta t\left\{\ddot{d}\right\}^{t+\Delta t}$$ (3.43)

$$\left\{\ddot{d}\right\}^{t+\Delta t} = \frac{1}{\beta\Delta t^2}\{d\}^{t+\Delta t} - \frac{1}{\beta\Delta t^2}\{d\}^{t} - \frac{1}{\beta\Delta t}\left\{\dot{d}\right\}^{t} - \frac{\left(\frac{1}{2}-\beta\right)}{\beta}\left\{\ddot{d}\right\}^{t}$$ (3.44)

The parameters β and λ are constants whose values depend on the finite difference scheme used in the calculations. Here it is used the constant-average acceleration method, which is implicit and unconditionally stable. For this method β is ¼ and λ is ½. Although the velocity vector is not required in Eq. (3.42), it is presented here because it will be needed subsequently. By substituting Eq. (3.44) into Eq. (3.42),

$$\left[\hat{K}\right]\{d\}^{t+\Delta t} = \left\{\hat{F}\right\}^{t+\Delta t} \tag{3.45}$$

where $\left[\hat{K}\right]$ is the effective stiffness matrix, and $\left\{\hat{F}\right\}^{t+\Delta t}$ is the effective force vector. These parameters are defined as

$$\left[\hat{K}\right] = \frac{1}{\beta \Delta t^2}[M] + [K] \tag{3.46}$$

$$\left\{\hat{F}\right\}^{t+\Delta t} = \{H\}^t + \{F\}^{t+\Delta t} \tag{3.47}$$

where $\{H\}^t$ is the following vector

$$\{H\}^t = [M]\left(\frac{1}{\beta\Delta^2}\{d\}^t + \frac{1}{\beta\Delta t}\{\dot{d}\}^t + \frac{1-2\beta}{2\beta}\{\ddot{d}\}^t\right) \tag{3.48}$$

Referring to Eq.(3.45), it is noted that the displacement, velocity, and acceleration at time t are known at every point inside the plate. Hence, the unknowns in Eq. (3.45) are the displacements vector $\{d\}^{t+\Delta t}$ and the force vector $\{F\}^{t+\Delta t}$. To determine these two unknowns, an additional expression is needed. This expression is developed below.

3.2.3.3 Solution Procedure

By combining Eq. (3.45) and (3.47), it is obtained

$$\left\{ \overset{\frown}{K} \right\} \{d\}^{t+\Delta t} = \{H\}^{t} + \{F\}^{t+\Delta t} \tag{3.49}$$

The displacement vector $\{d\}$ is expressed as the sum of the displacement due to the force $\{H\}$, and the contact force $\{F\}$

$$\{d\}^{t+\Delta t} = \{d\}_{H}^{t+\Delta t} + \{d\}_{F}^{t+\Delta t} \tag{3.50}$$

Eq. (3.49) and (3.50) give

$$\left[\overset{\frown}{K} \right] (\{d\}_{H}^{t+\Delta t} + \{d\}_{F}^{t+\Delta t}) = \{H\}^{t} + \{F\}^{t+\Delta t} \tag{3.51}$$

From Eq. (3.51)

$$\left[\overset{\frown}{K} \right] \{d\}_{H}^{t+\Delta t} = \{H\}^{t} \tag{3.52}$$

$$\left[\overset{\frown}{K} \right] \{d\}_{F}^{t+\Delta t} = \{F\}^{t+\Delta t} \tag{3.53}$$

It is wished to solve Eq.(3.52) and (3.53) for the displacement vectors $\{d\}_{H}$, and $\{d\}_{F}$. Note that the values of $\left[\overset{\frown}{K} \right]$ are known (see Eq. (3.46)). To proceed with the solution, it still must be specified the two force vectors $\{H\}$, and $\{F\}$ at every nodal point.

At each nodal point in the interior of the plate $\{F\}=0$ and $\{H\}$ is given by Eq. (3.48). At each nodal point on the top and bottom surfaces of the plate $\{F\}=0$ (except

at the point of impact where $\{F\} = f\{U\}$, [see Eq. (3.41)], and again $\{H\}$ is given by Eq. (3.48).

The solution of Eq. (3.52) and (3.53) now proceeds in two steps. First, the forces $\{H\}$ and the displacements $\{d\}_H$ are calculated from Eq. (3.48) and (3.52). This calculation is straightforward, since the mass matrix $[M]$, the time step Δt, as well as the displacement $\{d\}$, the velocity $\left\{\dot{d}\right\}$, and the acceleration $\left\{\ddot{d}\right\}$ at time t are all known.

Second, the contact force vector $\{F\}$ and the displacements $\{d\}_F$ are calculated as follows. At time $t+\Delta t$, Eq. (3.41) is written as

$$\{F\}^{t+\Delta t} = f^{t+\Delta t}\{U\} \tag{3.54}$$

where $f^{t+\Delta t}$ is the contact force at time $t+\Delta t$. Eq. (3.53) and (3.54) yield

$$\left[\hat{K}\right]\{d\}_F^{t+\Delta t} = f^{t+\Delta t}\{U\} \tag{3.55}$$

For a unit contact force ($f^{t+\Delta t} = 1$), Eq. (3.55) becomes

$$\left[\hat{K}\right]\{d\}_U^{t+\Delta t} = \{U\} \tag{3.56}$$

where $\{d\}_U^{t+\Delta t}$ is the displacement caused by the unit contact force. For a given effective stiffness matrix the displacement vector $\{d\}_U^{t+\Delta t}$ can be calculated from Eq. (3.56). From Eq. (3.55) and (3.56), it is seen that $\{d\}_F^{t+\Delta t}$ and $\{d\}_U^{t+\Delta t}$ are related by

$$\{d\}_F^{t+\Delta t} = f^{t+\Delta t}\{d\}_U^{t+\Delta t} \tag{3.57}$$

Eq. (3.50) and (3.57) give

$$\{d\}^{t+\Delta t} = \{d\}_H^{t+\Delta t} + f^{t+\Delta t}\{d\}_U^{t+\Delta t} \tag{3.58}$$

In Eq. (3.58), the unknowns are the displacement vector $\{d\}$ and the scalar contact force f at time $t+\Delta t$. In order to find these two unknowns, another expression for the contact force is required. During the loading and unloading processes the contact force is

$$f^{t+\Delta t} = \kappa(\alpha^{t+\Delta t})^{1.5} \qquad \text{during loading} \tag{3.59}$$

$$f^{t+\Delta t} = f_m\left(\frac{\alpha^{t+\Delta t} - \alpha_0}{\alpha_m - \alpha_0}\right)^{2.5} \qquad \text{during unloading} \tag{3.60}$$

$\kappa, f_m, \alpha_m,$ and α_0, are known as contacts defined previously and α is the indentation depth which varies with time. At time $t+\Delta t$ this depth is

$$\alpha^{t+\Delta t} = \delta_S^{t+\Delta t} - \delta_C^{t+\Delta t} \tag{3.61}$$

$\delta_C^{t+\Delta t}$ is the displacement of the center of the mid-surface of the plate in the direction of the impact. With the use of Eq. (3.58), δ_C can be expressed as

$$\delta_C^{t+\Delta t} = \delta_{CH}^{t+\Delta t} + f^{t+\Delta t}\delta_{CU}^{t+\Delta t} \tag{3.62}$$

where $\delta_C^{t+\Delta t}, \delta_{CH}^{t+\Delta t}$, and $\delta_{CU}^{t+\Delta t}$ are the magnitudes of the displacements at the center point of the mid-surface in the direction of impact at time $t+\Delta t$.

$\delta_S^{t+\Delta t}$ is the position of the center point of the impactor. At time $t+\Delta t$, the magnitude of $\delta_S^{t+\Delta t}$ is determined by Newton's second law

$$\delta_S^{t+\Delta t} = \int\limits_0^{t+\Delta t} \int\limits_0^{t+\Delta t} \frac{f}{m} \mathrm{d}t\, \mathrm{d}t \tag{3.63}$$

where f is the time varying contact force and m is the impactor mass.

By combining Eqs. (3.59)-(3.63), it is obtained the following expressions for the contact force:

$$f^{t+\Delta t} = \kappa \left(\int\limits_0^t \int\limits_0^t \frac{f}{m} \mathrm{d}t\, \mathrm{d}t - \delta_{CH}^{t+\Delta t} - f^{t+\Delta t} \delta_{CU}^{t+\Delta t} \right)^{1.5} \qquad \text{during loading} \tag{3.64}$$

$$f^{t+\Delta t} = f_m \left(\frac{\int\limits_0^t \int\limits_0^t \frac{f}{m} \mathrm{d}t\, \mathrm{d}t - \delta_{CH}^{t+\Delta t} - f^{t+\Delta t} \delta_{CU}^{t+\Delta t} - \alpha_0}{\alpha_m - \alpha_0} \right)^{2.5} \qquad \text{during unloading} \tag{3.65}$$

In the above expressions, for computational convenience, it is replaced the limits of the integrals $t+\Delta t$ by t. This implies that, in computing the contact force $f^{t+\Delta t}$, the value of δ_S at time $t+\Delta t$ is approximated by its value at time t.

The contact force $f^{t+\Delta t}$ is calculated either by Eq. (3.64) (during loading) or Eq. (3.65) (during unloading) by the Newton-Raphson method. Once the value of $f^{t+\Delta t}$ is known, the displacement vector $\{d\}$ at time $t+\Delta t$ is calculated from Eq. (3.58), and the velocity and acceleration vector at time $t+\Delta t$ are calculated from Eq. (3.43) and (3.44).

From the known displacements, the strains are calculated from Eq. (3.9), and, from the known strains, the stresses are obtained from Eq. (3.12).

The aforementioned procedure is repeated at each time step (Wu & Chang, 1989).

3.2.4 The Methods Employed in the Thesis

The equations of equilibrium governing the linear dynamic response of a system of finite elements can be written as

$$M\ddot{d} + C\dot{d} + Kd = F \tag{3.66}$$

where M, C, and K are the mass, damping, and stiffness matrices; F is the vector of externally applied loads; and $d, \dot{d},$ and $\ddot{d}$ are the displacements, velocity, and acceleration vectors of the finite element assemblage.

In direct integration the equations in (3.66) are integrated using a numerical step-by-step procedure, the term "direct" meaning that prior to the numerical integration, no transformation of the equations into a different form is carried out. There are a few commonly used effective direct integration methods such as the Central Difference Method, The Houbolt Method, The Wilson θ Method and The Newmark Method.

3.2.4.1 The Newmark Method

The following assumptions are used at The Newmark integration scheme:

$$\dot{d}^{t+\Delta t} = \dot{d}^{t} + \left[(1-\lambda)\ddot{d}^{t} + \lambda \ddot{d}^{t+\Delta t}\right]\Delta t \tag{3.67}$$

$$d^{t+\Delta t} = d^{t} + \dot{d}^{t}\Delta t + \left[\left(\frac{1}{2}-\beta\right)\ddot{d}^{t} + \beta \ddot{d}^{t+\Delta t}\right]\Delta t^2 \tag{3.68}$$

where λ and β are parameters that can be determined to obtain integration accuracy and stability. Newmark originally proposed as an unconditionally stable scheme the constant-average-acceleration method (also called trapezoidal rule), in which case λ = 1/2 and β = ¼ (see Figure 3.3).
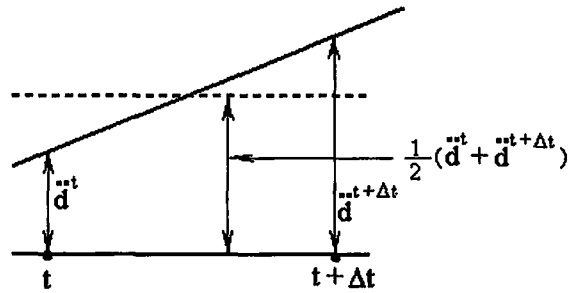
Figure 3.3 Newmark's constant-average-acceleration scheme.

In addition to Eq. (3.67) and (3.68), for solution of the displacements, velocities, and accelerations at time $t + \Delta t$, the equilibrium equations (3.66) at time $t + \Delta t$ are also considered:

$$M\ddot{d}^{t+\Delta t} + C\dot{d}^{t+\Delta t} + Kd^{t+\Delta t} = F^{t+\Delta t} \tag{3.69}$$

Solving from Eq. (3.68) for $\ddot{d}^{t+\Delta t}$ in terms of $d^{t+\Delta t}$ and then substituting for $\ddot{d}^{t+\Delta t}$ into Eq. (3.67), it is obtained equations for $\ddot{d}^{t+\Delta t}$ and $\dot{d}^{t+\Delta t}$, each in terms of the unknown displacements $d^{t+\Delta t}$ only. These two relations for $\dot{d}^{t+\Delta t}$ and $\ddot{d}^{t+\Delta t}$ are substituted into Eq.(3.69) to solve for $d^{t+\Delta t}$, after which, using Eq. (3.67) and (3.68), $\ddot{d}^{t+\Delta t}$ and $\dot{d}^{t+\Delta t}$ can also be calculated. The complete algorithm using the Newmark integration scheme is given in Table 3.1.

3.2.4.2 Implicit Integration

For nonlinear dynamic response calculations, a very common technique used is the trapezoidal rule, which is Newmark's method with $\lambda = 1/2$ and $\beta = \frac{1}{4}$, and this method is used to demonstrate the basic additional considerations involved in a nonlinear analysis.

Table 3.1 Step-by-step solution using Newmark integration method.

A. Initial calculations:

1. Form stiffness matrix K, mass matrix M, and damping matrix C.

2. Initialize d^0, $\dot{d}^0$, and $\ddot{d}^0$.

3. Select time step Δt and parameters β and λ and calculate integration constants:

$$\lambda \geq 0.50; \qquad \beta \geq 0.25(0.5 + \lambda)^2$$

$$a_0 = \frac{1}{\beta \Delta t^2}; \qquad a_1 = \frac{\lambda}{\beta \Delta t}; \qquad a_2 = \frac{1}{\beta \Delta t}; \qquad a_3 = \frac{1}{2\beta} - 1;$$

$$a_4 = \frac{\lambda}{\beta} - 1; \qquad a_5 = \frac{\Delta t}{2}\left(\frac{\lambda}{\beta} - 2\right); \qquad a_6 = \Delta t(1 - \lambda); \qquad a_7 = \lambda \Delta t$$

4. Form effective stiffness matrix $\hat{K}$: $\hat{K} = K + a_0 M + a_1 C$.

5. Triangularize $\hat{K}$: $\hat{K} = LDL^T$

B. For each time step:

1. Calculate effective loads at time $t + \Delta t$:

$$\hat{F}^{t+\Delta t} = F^{t+\Delta t} + M\left(a_0 d^t + a_2 \dot{d}^t + a_3 \ddot{d}^t\right) + C\left(a_1 d^t + a_4 \dot{d}^t + a_5 \ddot{d}^t\right)$$

2. Solve for displacements at time $t + \Delta t$:

$$LDL^T d^{t+\Delta t} = \hat{F}^{t+\Delta t}$$

3. Calculate accelerations and velocities at time $t + \Delta t$:

$$\ddot{d}^{t+\Delta t} = a_0\left(d^{t+\Delta t} - d^t\right) - a_2 \dot{d}^t - a_3 \ddot{d}^t$$

$$\dot{d}^{t+\Delta t} = \dot{d}^t + a_6 \ddot{d}^t + a_7 \ddot{d}^{t+\Delta t}$$

As in linear analysis, using implicit time integration, it is considered the equilibrium of the system at time $t + \Delta t$. This requires in nonlinear analysis that an iteration be performed. Using, for instance, the modified Newton-Raphson iteration, the governing equilibrium equations are (neglecting the effects of a damping matrix):

$$M \ddot{d}_{(k)}^{t+\Delta t} + K^t \Delta d_{(k)} = F^{t+\Delta t} - R_{(k-1)}^{t+\Delta t} \qquad (3.70)$$

The vector $F^{t+\Delta t}$ stores the externally applied nodal loads and $R^{t+\Delta t}$ is the vector of nodal point forces that are equivalent to the element stresses.

$$d_{(k)}^{t+\Delta t} = d_{(k-1)}^{t+\Delta t} + \Delta d_{(k)} \qquad (3.71)$$

Using the trapezoidal rule of time integration, the following assumptions are employed:

$$d^{t+\Delta t} = d^t + \frac{\Delta t}{2}\left(\dot{d}^t + \dot{d}^{t+\Delta t} \right) \qquad (3.72)$$

$$\dot{d}^{t+\Delta t} = \dot{d}^t + \frac{\Delta t}{2}\left(\ddot{d}^t + \ddot{d}^{t+\Delta t} \right) \qquad (3.73)$$

Using the relations in Eq. (3.71) to (3.73),

$$\ddot{d}_{(k)}^{t+\Delta t} = \frac{4}{\Delta t^2}\left(d_{(k-1)}^{t+\Delta t} - d^t + \Delta d_{(k)} \right) - \frac{4}{\Delta t}\dot{d}^t - \ddot{d}^t \qquad (3.74)$$

is obtained and substituting into Eq.(3.70), following equations are obtained,

$$\hat{K}^{t}\,\Delta d_{(k)} = F^{t+\Delta t} - R_{(k-1)}^{t+\Delta t} - M\left[\frac{4}{\Delta t^{2}}\left(d_{(k-1)}^{t+\Delta t} - d^{t}\right) - \frac{4}{\Delta t}\dot{d}^{t} - \ddot{d}^{t}\right] \tag{3.75}$$

$$\hat{K}^{t} = K^{t} + \frac{4}{\Delta t^{2}}M \tag{3.76}$$

The iterative equations in dynamic nonlinear analysis using implicit time integration are of the same form as the equations in static nonlinear analysis, except that both the coefficient matrix and the nodal point force vector contain contributions from the inertia of the system. It can be therefore directly concluded that all iterative solution strategies for static analysis are also directly applicable to the solution of Eq. (3.75). However, since the inertia of the system renders its dynamic response, in general, "more smooth" than its static response, convergence of the iteration can, in general, be expected to be more rapid than in static analysis, and the convergence behavior can be improved by decreasing Δt. The numerical reason for the better convergence characteristics in a dynamic analysis as Δt decreases lies in the contribution of the mass matrix to the coefficient matrix. This contribution increases and ultimately becomes dominant as the time step decreases.

In the first solutions of nonlinear dynamic finite element response, equilibrium iterations are not performed in the step-by-step incremental analysis; i.e., the relation in Eq. (3.75) is simply solved for k=1 and the incremental displacement $\Delta d^{(1)}$ is accepted as an accurate approximation to the actual displacement increment from time t to time $t+\Delta t$. However, it is then recognized that the iteration could actually be of utmost importance since any error admitted in the incremental solution at a particular time directly affects in a path-dependent manner the solution at any subsequent time. Indeed, because any nonlinear dynamic response is highly path-dependent, the analysis of a nonlinear dynamic problem requires iteration at each time step more stringently than does a static analysis (Bathe, 1996).

3.3 Failure Analysis

Since impact damage is a very complicated phenomenon, predicting impact damage requires a thorough understanding of the basic damage mechanism and mechanics governing the impact damage event. To achieve such understanding, Choi & Chang (1992) studied the impact damage.

It was considered that the sequence of the impact damage mechanisms in laminated composites with a brittle matrix could be described in general as follows:

Transverse impact first initiates critical matrix cracks in a layer within the laminate. Such cracks can generate delaminations immediately along the bottom or upper interface of the cracked layer, depending on the position of the layer in the laminate. As the duration of impact proceeds, additional matrix cracks can occur subsequently in the other layers and can produce additional delaminations along the other interfaces.

Accordingly, in order to predict accurately the impact damage, a model must be able to predict the initiation of the critical matrix cracks, estimate the extent of delamination, and follow the correct sequence of the impact damage mechanism. Accordingly, two failure criteria, critical matrix cracking criterion and impact-induced delamination criterion, are used in 3DIMPACT Computer Code.

3.3.1 Critical Matrix Cracking Criterion

In order to predict the occurrence of the critical matrix cracks, the matrix failure criterion proposed by Choi et al. (1991 b) is adopted to 3DIMPACT Computer Code. The criterion can be expressed as

$$\left(\frac{^n\overline{\sigma}_{yy}}{^nY}\right)^2 + \left(\frac{^n\overline{\sigma}_{yz}}{^nS_i}\right)^2 = e_M{}^2 \qquad \begin{array}{l} e_M \geq 1 \ \text{Failure} \\ e_M < 1 \ \text{No failure} \\ ^nY = {}^nY_t \ \text{if} \ \overline{\sigma}_{yy} \geq 0 \\ ^nY = {}^nY_c \ \text{if} \ \overline{\sigma}_{yy} \langle \ 0 \end{array} \qquad (3.77)$$

where the subscripts of x and y are the local coordinates of the nth layer parallel and normal to the fiber directions, respectively, and z is the out-of plane direction. S_i is the interlaminar shear strengths within the laminate under consideration, and Y_t and Y_c are the ply transverse tensile and compressive strengths, respectively. Unfortunately, the interlaminar shear strength within the laminate has not been well characterized in the literature and was frequently taken to be associated with in-plane shear strength. Therefore, the values of Y_t and S_i of nth ply are determined in this code from the empirical expressions proposed previously by Chang & Lessard (1991) with the following forms:

$$Y_t^n = Y_t^0\left(1 + A\frac{\sin(\Delta\theta)}{M^B}\right) \qquad (3.78)$$

$$S_i^n = S^0\left(1 + C\frac{\sin(\Delta\theta)}{M^D}\right) \qquad (3.79)$$

where $\Delta\theta$ is the minimum ply angle change between the nth ply or the ply group and its neighboring plies with different ply orientations, and M is the total number of the layers in the ply group that is considered. The ply group defines as the plies with the same ply orientations group together. Y_t^0 is the transverse tensile strength of a $[90_n]_s$ composite ($n{\geq}6$), and S^0 is the ply shear strength measured from a unidirectional composite with more than eight layers. A, B, C, and D are the empirical parameters which can be determined from experiments (Chang & Lessard, 1991). $\bar{\sigma}_{yz}$ and $\bar{\sigma}_{yy}$ are the averaged interlaminar and in-plane transverse stresses, respectively, within the nth ply which can be expresses as

$$\bar{\sigma}_{yz}^n = \frac{1}{h_n}\int_{t_{n-1}}^{t_n}\sigma_{yz}dz \qquad (3.80)$$

$$\bar{\sigma}_{yy}^n = \frac{1}{h_n}\int_{t_{n-1}}^{t_n}\sigma_{yy}dz \qquad (3.81)$$

where t_n and t_{n-1} are the upper and lower interfaces of the nth ply in the laminate and h_n is the thickness of the ply.

Whenever the calculated averaged stresses in any one of the plies in the laminate first satisfy the criterion ($e_M = 1$) during impact, initial impact damage is predicted. It is assumed then that the matrix crack will propagate throughout the thickness of the ply group, which contained the cracked ply. The time t corresponding to the initial damage is designated as t_M. A delamination can be immediately induced from the location of the matrix crack along the interfaces of the ply group. As the time increases ($t > t_M$) during impact, additional matrix cracking could be produced in the other layers. Hence, the criterion should continuously be applied to the other layers for determining any additional matrix failure. If no additional matrix cracking is found at any other layers during impact, then the impactor's velocity associated with the first matrix cracking is referred to as the impact velocity threshold, which is the velocity required to just cause the initial impact damage of the laminate.

3.3.2 Impact-Induced Delamination Criterion

Once a critical matrix crack is predicted in a ply within the laminate, a delamination can be initiated from the crack. To accurately simulate delamination propagation is very difficult and complicated, involving multiple dynamic crack propagation and delamination surfaces interaction.

Basically, there are two types of critical cracks initiating delamination resulting from impact (Choi et al., 1991 b): one can be referred to as the shear crack generating within the laminates and the other is referred to as the bending crack producing from bottom surfaces of the laminates as shown in Figure 3.4. In order to effectively estimate the extent of the delamination growth, it would be necessary to include the basic governing parameters controlling the delamination propagation in the model. The delamination resulting from point-nose impact appears generally in a peanut shape as shown in Figure 3.5. The longitudinal axis of the delamination tends to the orient itself in the direction parallel to the fiber direction of the bottom layer

below the interface. In general, once a delamination is initiated from a critical matrix crack, it could grow much more extensively along the fiber direction than in the transverse direction of the bottom layer at the interface. This may provide an explanation why delamination appears to be in a peanut shape in laminated composites.
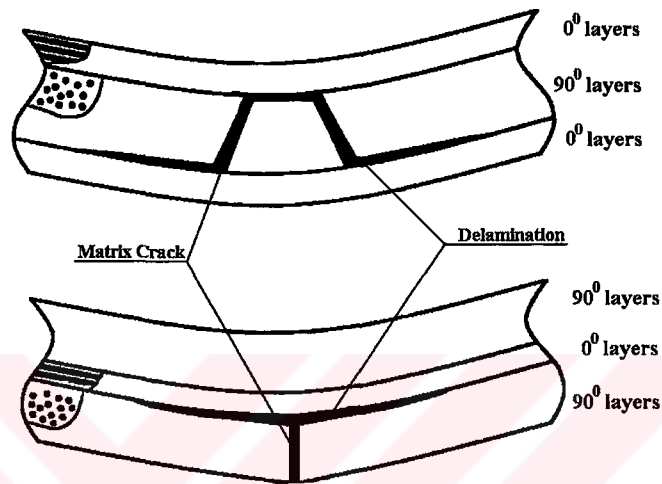

Figure 3.4 Basic impact damage mechanism of fiber-reinforced laminated composites. Top: delamination induced by inner shear cracks. Bottom: delamination induced by a surface-bending crack.
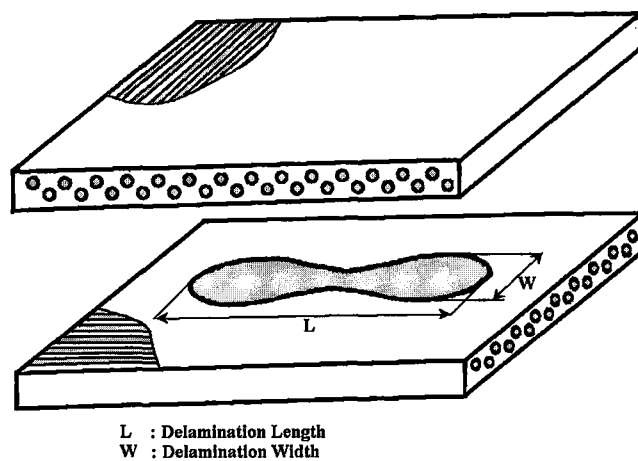

Figure 3.5 A typical delamination shape in laminated composites induced by a point-nose impact.

For the shear-crack induced delaminaton, the interlaminar longitudinal shear stress (along the fiber direction) σ_{xz} in the layer right below the interface and the interlaminar transverse shear stress σ_{yz} in the layer right above the interface governing the delamination growth. A schematic description of the delamination growth mechanisms induced by a shear crack is shown in Figure 3.6. However, for a bending crack-induced delamination, the interlaminar longitudinal shear stresses σ_{xz} in the layer right below the interface would govern the major growth of the delamination, and the in-plane bending stress σ_{yy} in the layer right below the interface would advance the delamination propagation in the secondary direction (normal to the fiber direction). A schematic description of the delamination growth mechanism induced by a bending crack is shown in Figure 3.7.

Accordingly, by taking both failure mechanisms into consideration, the distributions of the interlaminar longitudinal shear stress σ_{xz} and transverse in-plane stress σ_{yy} throughout the thickness of the bottom layer of the interface and the interlaminar transverse shear stress σ_{yz} in the upper layer contribute significantly to the delamination growth resulting front point-nose impact. Therefore, it is considered that delamination growth due to low-velocity impact could occur, only when the following two sequential conditions are met:

1. One of the ply groups intimately above or below the concerned interface has failed due to matrix cracking.

2. The combined stresses governing the delamination growth mechanisms through the thicknesses of the upper and lower ply groups of the interface reaches a critical value.

Based on the above second statement, the following impact-induced delamination growth criterion for low velocity impact proposed by Choi & Chang (1992) is applied at this code.

Impact Damage Growth Mechanism

Delamination Induced by Shear Cracking
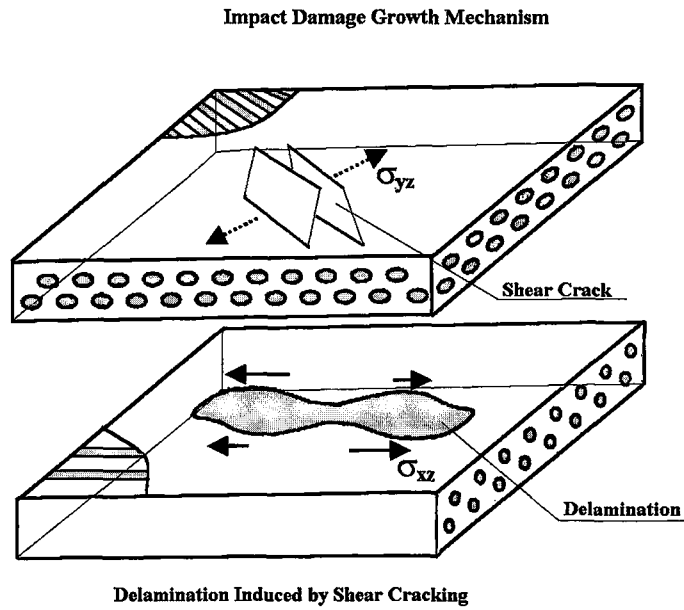
Figure 3.6 A schematic description of the delamination growth mechanism induced by a shear crack in laminated composite subjected to point-nose impact.

Impact Damage Growth Mechanism

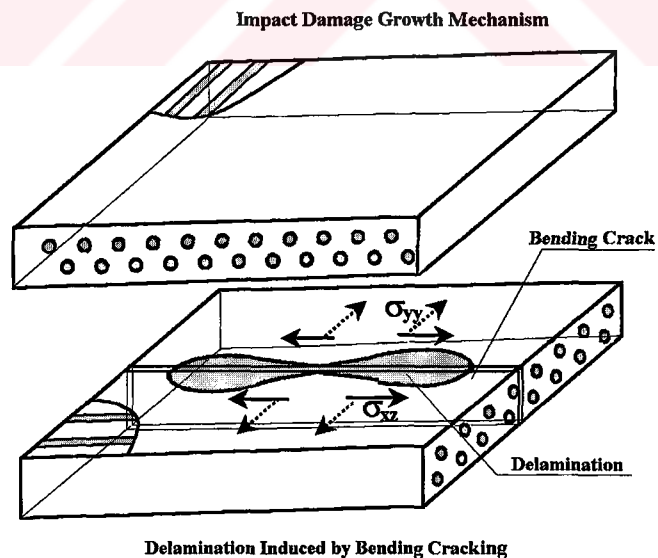Delamination Induced by Bending Cracking

Figure 3.7 A schematic description of the delamination growth mechanism induced by a bending crack in laminated composite subjected to point-nose impact.

$$D_a\left[\left(\frac{\overline{\sigma_{yz}^n}}{{}^nS_i}\right)^2+\left(\frac{\overline{\sigma_{xz}^{n+1}}}{{}^{n+1}S_i}\right)^2+\left(\frac{\overline{\sigma_{yy}^{n+1}}}{{}^{n+1}Y}\right)^2\right]=e_D^2 \qquad \begin{array}{l} e_D \ge 1 \text{ Failure} \\ e_D < 1 \text{ No failure} \\ {}^{n+1}Y = {}^{n+1}Y_t \text{ if } \overline{\sigma_{yy}} \ge 0 \\ {}^{n+1}Y = {}^{n+1}Y_c \text{ if } \overline{\sigma_{yy}} \langle\ 0 \end{array} \qquad (3.82)$$

where D_a is an empirical constant which has to be determined from experiments as will be described in following. Once chosen, it was found to be quite insensitive to the ply orientation and thickness of the laminates, and primarily dependent only on the material system used. The subscripts x, y and z are the local material coordinates of an individual ply within the laminate, and the superscripts n and $n + 1$ correspond to the upper and lower plies of the nth interface, respectively. $\overline{\sigma_{yz}}$ and $\overline{\sigma_{yy}}$ are the averaged interlaminar and in-plane transverse stresses within the nth and $(n + 1)^{\text{th}}$ ply, respectively. $\overline{\sigma_{xz}}$ is the averaged interlaminar longitudinal stress within the $(n + 1)^{\text{th}}$ ply which can be expressed as

$$\overline{\sigma_{xz}^{n+1}}=\frac{1}{h_{n+1}}\int_{t_n}^{t_{n+1}}\sigma_{xz}\,dz \qquad (3.83)$$

where t_{n+1} and t_n are the upper and lower interfaces of the $(n + 1)^{\text{th}}$ ply in the laminate and h_{n+1} is the thickness of the ply.

In order to determine the sensitivity of the empirical constant D_a to laminate configuration, the delamination lengths of the laminates with three tested ply orientations are calculated from the values of D_a varying in a wide range. The calculated lengths are then compared with the corresponding data from the experiments. The measured delamination sizes and shapes from X-radiographs are used for determining the value. An error formula (Eq. 3.84) is selected to estimate the discrepancies between the predictions and measurements based on various values of D_a. The error formula can be expressed as

$$Err^2=\frac{1}{L^2N}\sum_{i=1}^{N}(L_c^i-L_l^i)^2 \qquad (3.84)$$

where

L_c = calculated delamination length

L_t = tested delamination length

L = specimen length

N = number of test data.

In this investigation, a value of 1.0 is chosen for D_a [(Wang & Yew, 1990), (Liu, 1993) and (Liu et al., 1993 a,b)].

Accordingly, once a critical matrix crack is predicted in a layer, the delamination criterion is then applied to estimate the extent of the delamination along the interface of the cracked ply in the laminate. It is noted that only the delaminations along the bottom interface (see Figure 3.4) induced by shear cracks or along the upper interface induced by a bending crack are included in the analysis. The small, confined delamination along the upper interface induced by shear cracks (see Figure 3.4) is ignored in the 3DIMPACT Computer Code.

The procedure for determining the extent of the impact damage can be described as follows:

1. Calculating transient dynamic stresses within each layer as function of time

2. Applying the matrix failure criterion for predicting the critical matrix cracks in each layer for determination of the extent of delaminations

3. If matrix cracking is predicted in a layer of the laminate, then applying the delamination criterion subsequently in the upper and bottom layer of the interface during the entire period of impact.

The sequence of the above impact damage mechanism is essential for predicting the impact damage. The procedure has to be repeated at the other layers during impact for determining any additional matrix cracking and delaminations. The final size of each delamination is determined by the area within which the stress

components satisfy the delamination failure criterion during the entire duration of impact. No material degradation is considered in the model and it is also noted that the model doesn't take into account the delamination interaction during impact which may be important for multiple delaminations (Choi & Chang,1992).

3.4 Finite Element Mesh

The three-dimensional finite element mesh of a laminated composite plate, which consists of a 8-point brick elements, is shown in Figure 3.8. The laminate is discretized in to a total of NxMxQ elements. A total of four elements are used through the thickness of the laminate. The mesh is made progressively coarser towards the boundary. Choi & Chang (1992) evaluated the effect of finite element mesh size on the stability of the numerical prediction based on the model. They found that the propose failure analysis does not require the use of an extensive fine mesh. Therefore, a regular mesh of 768 [N(=16)x M(=12)xQ(=4)] is used in the numerical calculations for generating the results.
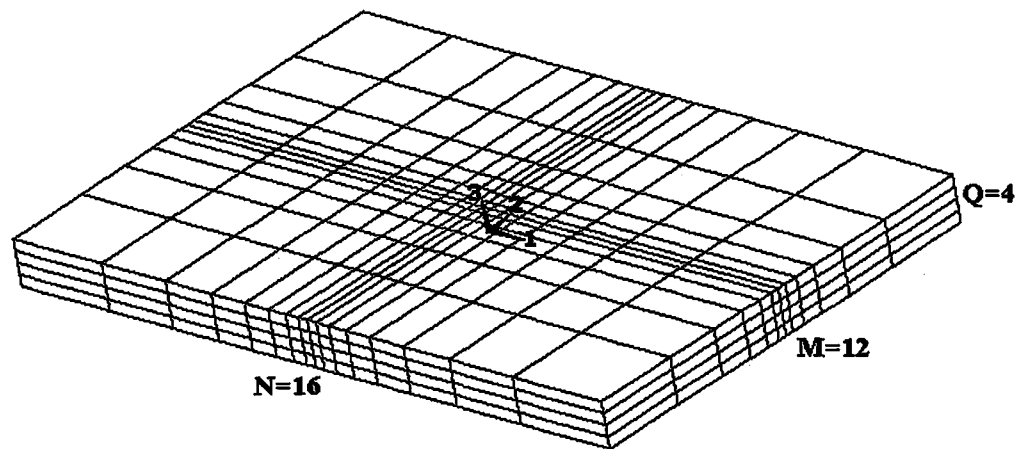

Figure 3.8 Finite element mesh.

CHAPTER FOUR

MATERIAL

4.1 Introduction

This chapter is devoted to the production of the laminated composite material and experimental characterization of the material properties of a unidirectional and woven ply under static loading conditions. Experimental characterization refers to the determination of the material properties through tests conducted on suitably designed specimens. Due to the special characteristics of composites, such as anisotropy, coupling effects and a variety of possible failure modes, it has been found that the mechanical test methods that are used for conventional metallic materials are usually not applicable to composites. There are various testing techniques for determination of the mechanical properties of composite materials. In the thesis, many of the mechanical properties of composite materials are determined by the ASTM (American Society for Testing and Materials) standards.

The fiber reinforced laminated composite materials used in the thesis are manufactured from E-glass fibers and epoxy resin. The material properties of E-glass/epoxy material are fully characterized under tension and compression, and under in-plane and out-of plane shear, in static conditions.

4.2 Production of the Laminated Composite Material

The fiber reinforced laminated composite materials used in the thesis are produced at Izoreel Firm. The composite laminates are manufactured from E-glass fibers and epoxy resin. Two fiber forms are selected for the E-glass fibers. The volume fraction is approximately 64 % in woven fibers and 57 % in unidirectional

fibers. For matrix materials, epoxy CY225 and hardener HY225 are mixed in the mass ratio of 100:80. The curing is carried out at 120 ^{0}C for 4 hours under a pressure of 0.2 MPa. The post curing is carried out at 100 ^{0}C for 2 hours. It is then cooled to room temperature at the same pressure. A total of six laminates with differing thicknesses and fiber stacking sequences are studied, details of which are given in Table 4.1. For unidirectional fiber reinforced laminated composite, four stacking sequences $(0^0/90^0/0^0)_s$, $(0^0/-45^0/+45^0)_s$, $(0^0/0^0/90^0/90^0)_s$ and $(0^0/90^0/0^0/90^0)_s$ are considered. Two stacking sequences have 6 plies and the other two stacking sequences have 8 plies. For woven fiber reinforced laminated composite, the stacking sequence consists of six layers of identically oriented woven fibers. The two nominal thicknesses with averages of 1.4 mm and 2.8 mm are used for studying the thickness effect.

4.3 Determination of the Mechanical Properties of the Laminated Composite Material

Static mechanical characterization has been carried out before impact testing, in order to evaluate the mechanical constants for each layer of the composite. All of the elastic parameters and the strength of composite materials studied are measured in the Department of Metallurgical and Materials Engineering. The parameters employed are listed in Table 4.2 for a unidirectional layer and Table 4.3 for a woven layer.

Table 4.1 Characteristics of laminates studied.

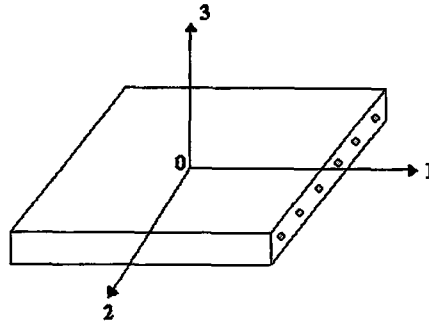| Fiber Form	Stacking Sequence	Number of Plies	Nominal Thickness (mm)
unidirectional	$(0^0/90^0/0^0)_s$	6	3.4
unidirectional	$(0^0/-45^0/+45^0)_s$	6	4.4
unidirectional	$(0^0/0^0/90^0/90^0)_s$	8	4.8
unidirectional	$(0^0/90^0/0^0/90^0)_s$	8	4.8
woven	$(0^0,90^0)_6$	6	1.4
woven	$(0^0,90^0)_6$	6	2.8

Figure 4.1 The coordinate system used for the composite laminates.

The mechanical properties of the composite lamina are measured by Shimadzu-AG Tensile Testing Machine of 50 kN load capacity at a ratio of 0.5 mm/min. The coordinate system used to describe the properties is shown in Figure 4.1. The direction indicated as 1 is along the fibers and the direction indicated as 2 is normal to the fibers in the laminate plane and direction 3 is through the laminate thickness.

The specimens in tension tests are manufactured based on ASTM D 3039-76 standards. The specimens and the dimensions are shown in Figure 4.2 (ASTM D 3039-76, 1990). Nominal specimen thickness is 3.3 mm for unidirectional reinforced laminated composite and 2.8 mm for woven reinforced laminated composite. Lay-up of laminates is $(0^0)_6$. To obtain the modulus of elasticity in the fiber direction (E_1), Poisson's ratio (v_{12}) and the tensile strength in the fiber direction (X_t) a specimen whose fiber direction coinciding with the loading direction is taken and two strain gauges perpendicular to each other are stuck on. One of them is in the fiber direction, the other is in the transverse direction. A uniaxial tension test is used in the fiber direction and the specimen is loaded step by step up to rupture. For all steps, strains in the fiber directions (ε_1) and strains in the transverse directions (ε_2) are measured by an indicator. The specimens in compressive tests are manufactured based on ASTM D 3410-87 standard test method for compression strength (ASTM D 3410-87, 1990).

To define the shear modulus G_{12}, a specimen whose principal axis is on 45^0 is taken and a strain gauge is stuck on loading direction of the lamina. The specimen is loaded by a test machine and G_{12} is calculated by using one strain gauges in the tensile direction as shown in Eq. (4.1) (Jones, 1998).
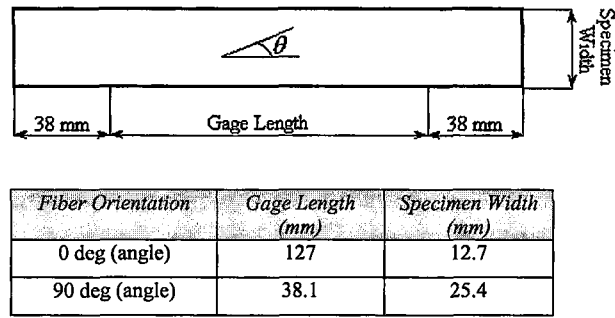
Figure 4.2 Tensile test specimens.

$$G_{12} = \cfrac{1}{\left(\cfrac{4}{E_x} - \cfrac{1}{E_1} - \cfrac{1}{E_2} + \cfrac{2\upsilon_{12}}{E_1}\right)}$$ (4.1)

To find the shearing strength S, T-Shear Test Set-up developed in the Mechanical Laboratory is used. A flat lamina, which has a T shape is taken as shown in Figure 4.3 and loaded up to rupture. Minimum clearance is left to prevent bending and to provide contact between the specimen and the metal support. The load at rupture (F_{max}) is taken and shear strength is calculated by the following equation (Aktaş & Karakuzu, 1999).

$$S = \frac{F_{max}}{2.h.t_T}$$ (4.2)
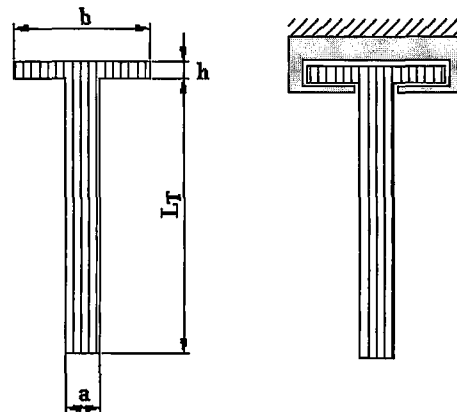
Figure 4.3 T-Shear Test Set-up.
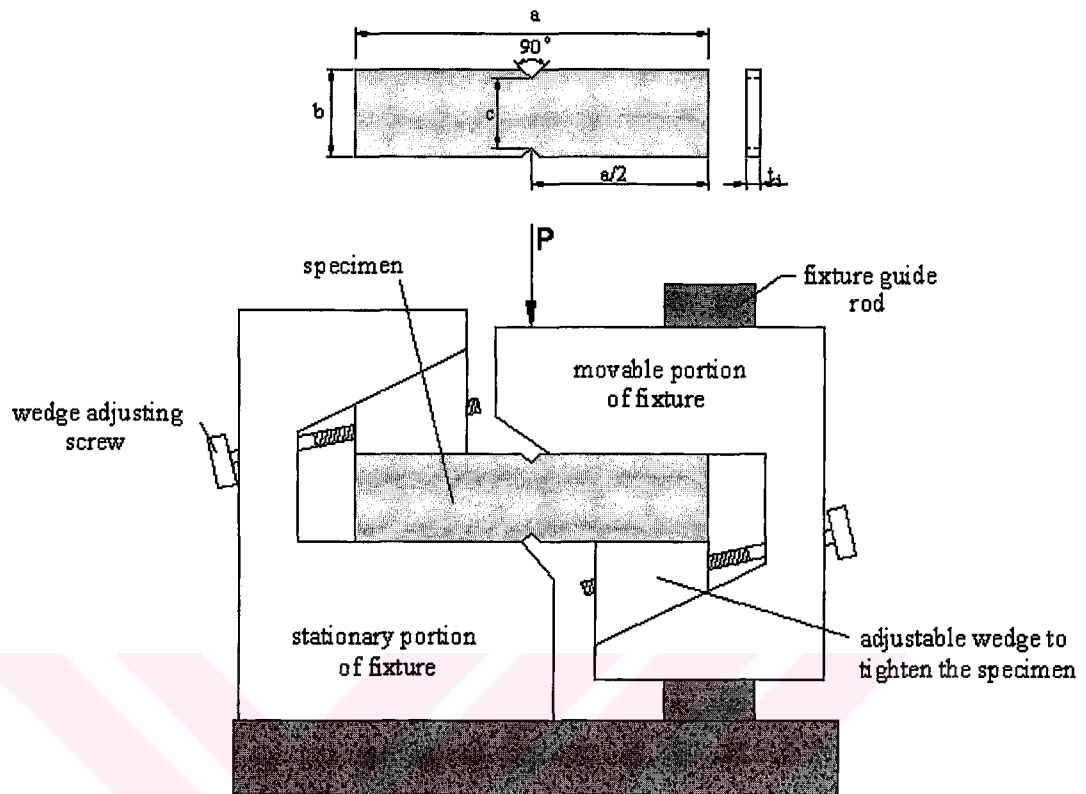
Figure 4.4 Iosipescue Shear Test Method.

The dimensions of the specimen are chosen as h = 5 mm, L_T = 80 mm, a = 10 mm and b = 40 mm. The thickness of the plate t_T is 2.8 mm for woven reinforced laminated composite and 3.3 mm for unidirectional reinforced laminated composite.

Iosipescue Shear Test Method (Figure 4.4) is also used to find shearing strength S and in plane shear modulus G_{12}. Results obtained by T-Shear Test Set-up and Iosipescue Shear Test Method agreed fairly well and are shown separately in Table 4.3. The dimensions of the Iosipescue specimen are chosen as a = 80 mm, b = 20 mm and c = 12 mm. The load at failure (F_{max}) is taken and shear strength is calculated by the following equation:

$$S = \frac{F_{max}}{c.t_i}$$ (4.3)
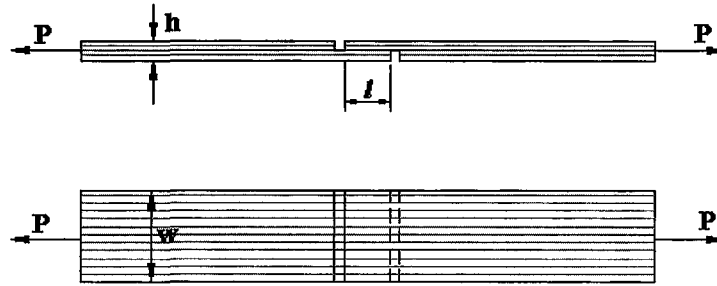
Figure 4.5 Double-notch shear test specimen.

To find the interlaminar shear strength S_i, double-notch shear test as described in ASTM specification D 3846-79 has been used (ASTM D 3846-79, 1990). The specimen is a unidirectional coupon 79.5 mm long, 12.7 mm wide (w), and 2.8 mm thick (h) as shown in Figure 4.5. Two parallel notches or grooves are machined, one on each face of the specimen, 6.4 mm (l) apart and of depth equal to half the specimen thickness. When this specimen is loaded in uniaxial tension, shear failure results along the mid plane of the specimen between the notches. The interlaminar shear strength is then given by

$$S_i \cong \frac{P}{wl} \tag{4.4}$$

where P is the failure load, l is the distance between notches, and w is the width of the specimen.

In an impact analysis the mass of the structure has to be taken into consideration. Therefore, a density test is conducted in order to place the correct mass value in the theoretical calculation. The density ρ of the composite laminates is derived by weighting the composite plates, measuring its volume and calculating their ratio.

Table 4.2 The measured mechanical properties of a unidirectional layer.

Symbol	Value	Property
V_f	57 %	fiber volume fraction
ρ	1.506 gr/cm^3	density
E_1	44 GPa	longitudinal modulus
E_2	10.5 GPa	transverse modulus
G_{12}	3.7 GPa	in-plane shear modulus (45^0 off-Axis Test)
v_{12}	0.36	major poisson's ratio
X_t	800 MPa	longitudinal tensile strength
Y_t	50 MPa	transverse tensile strength
X_c	350 MPa	longitudinal compressive strength
Y_c	125 MPa	transverse compressive strength
S_i	35 MPa	interlaminar shear strength
S	60 MPa	in-plane shear strength

Table 4.3 The measured mechanical properties of a woven layer.

Symbol	Value	Property
V_f	64 %	fiber volume fraction
ρ	1.78 gr/cm^3	density
E_1	20 GPa	longitudinal modulus
E_2	20 GPa	transverse modulus
G_{12}	4 GPa	in-plane shear modulus (Iosipescue)
v_{12}	0.1171	major poisson's ratio
X_t	473 MPa	longitudinal tensile strength
Y_t	473 MPa	transverse tensile strength
X_c	300 MPa	longitudinal compressive strength
Y_c	300 MPa	transverse compressive strength
S_i	35 MPa	interlaminar shear strength
S	85 MPa [T specimen] 90 MPa [Iosipescue]	in-plane shear strength

---
CHAPTER FIVE
IMPACT TESTING APPARATUS

5.1 Introduction

In the thesis, to simulate actual impact by a foreign object, a vertical drop-weight testing machine was developed in the Mechanical Laboratory. The impact of a composite structure by a larger projectile at low velocity is best simulated using a drop-weight tester. The apparatus consists of a tower frame, a piezoelectric force transducer, a conditioning amplifier, a computer coupled with a sound card and Matlab Data Acquisition Toolbox as digital oscilloscope.

5.2 Impact Testing Apparatus

The drop-weight impact tower consists of two vertical steel rods mounted on a heavy steel base as depicted in Figures 5.1, 5.2 and 5.3. a Brüel & Kjaer 8201 type piezoelectric force transducer with a hemispherical steel cap was mounted on the bottom side of a steel cross-bar. The diameter of the hemispherical impactor nose is equal to 18 mm. The force transducer has a force capacity of 20 kN. Each end of the cross bar is attached to a frictionless linear bearing to minimize friction. The bearings carry the cross bar up and down on the vertical steel rods. The total mass of the whole drop-weight is 2.6 kg. If needed, additional mass can be added on top of the cross bar. Drop heights range from 0.05m to 1.03m. Corresponding impact velocities are found as 1 m/sec to 4.5 m/sec based on the free fall formula.

Signals from piezoelectric force transducer are amplified by a signal-conditioning amplifier (NEXUS-2692 A OI1). The output from the conditioning amplifier is collected by a computer coupled with a sound card and Matlab Data Acquisition
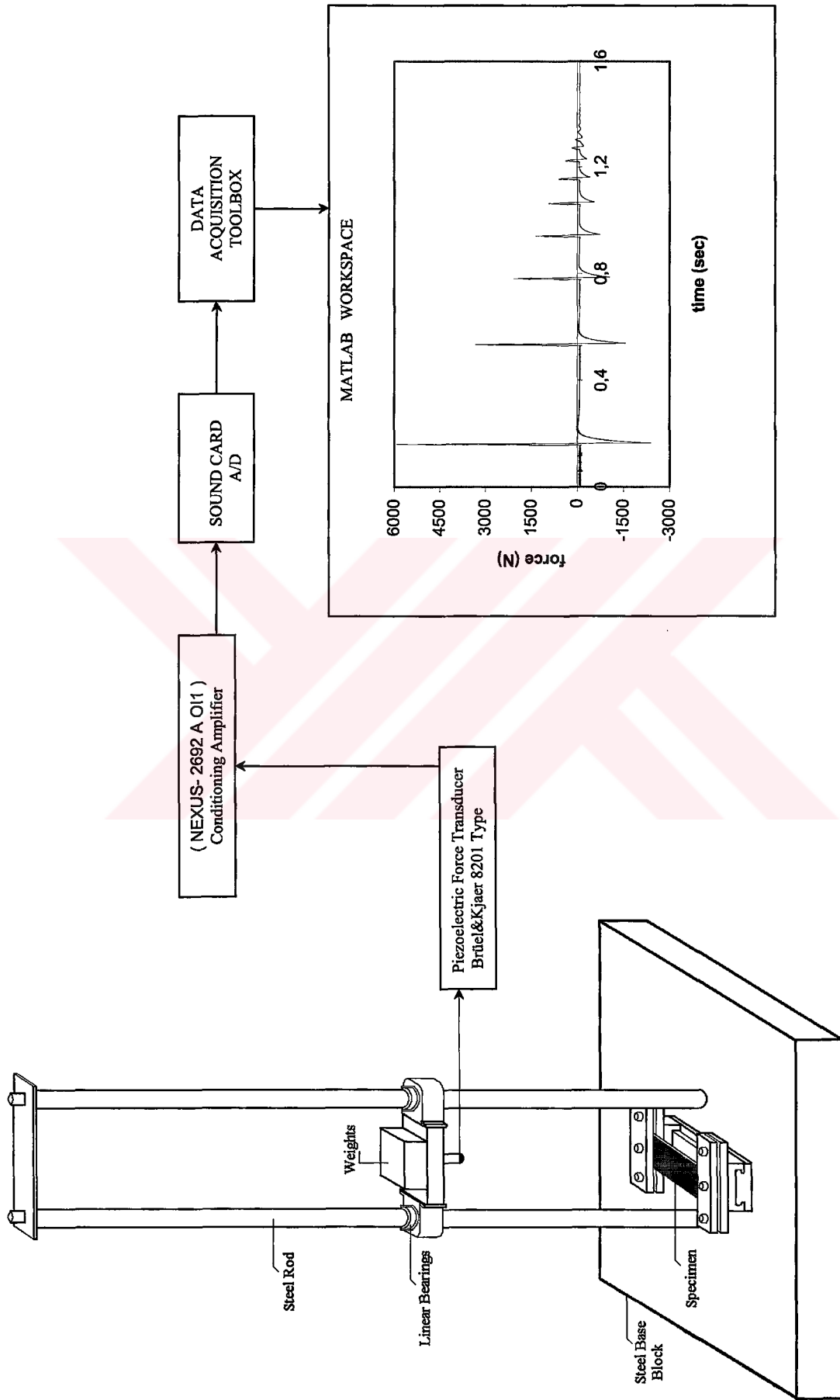
Figure 5.1 The schematic diagram of drop-weight test system.

1 : steel base block
2 : sledge
3 : bold (M6x10)
4 : target holder
5 : steel rod
6 : impactor
7 : force transducer
8 : bearing shell (KGB 30)
9 : segment
10 : linear bearing (KB 30)
11 : steel rod
12 : supporting plate
13 : bold (M6x10)
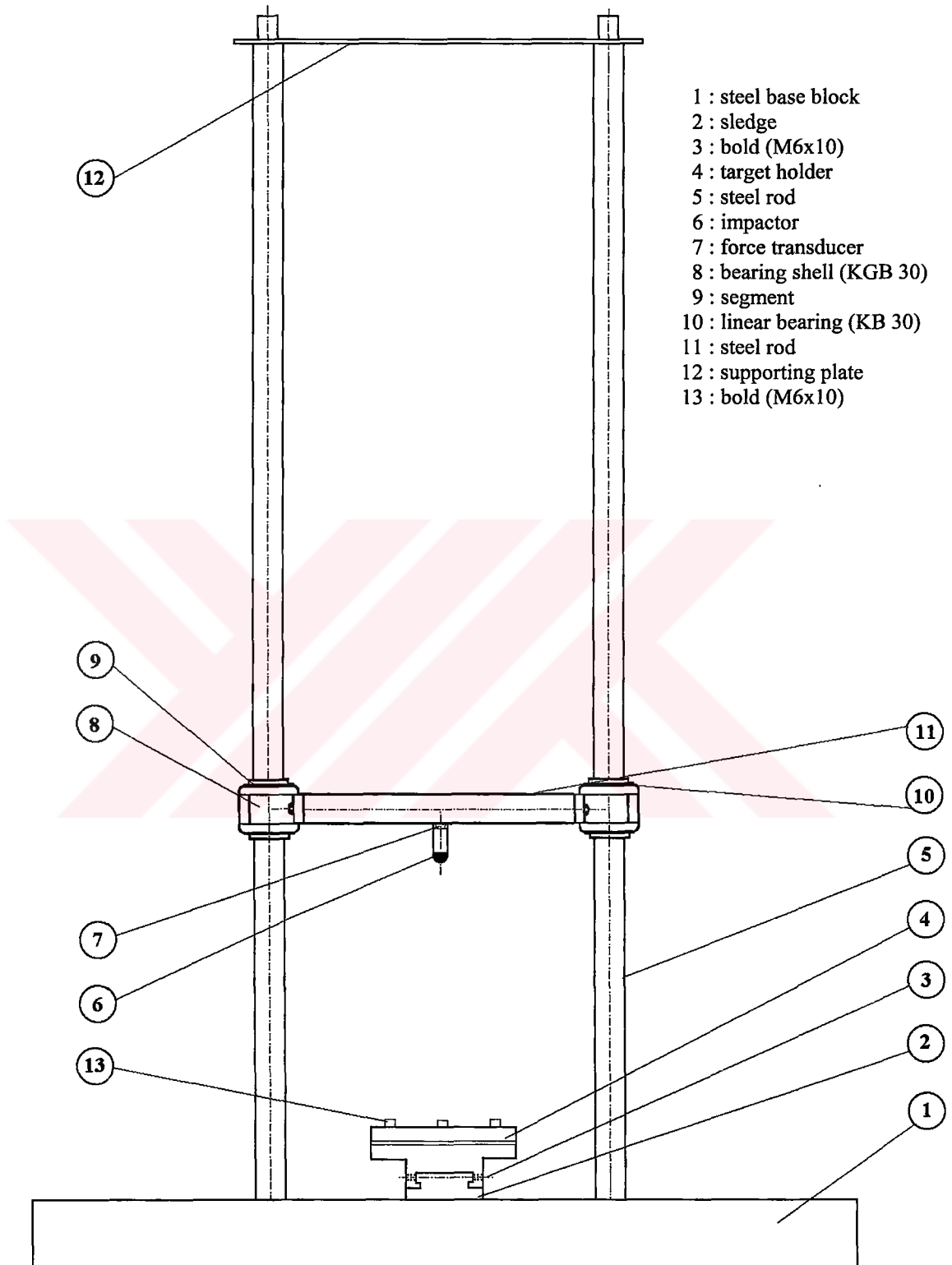
Figure 5.2 Drop weight impact tower.
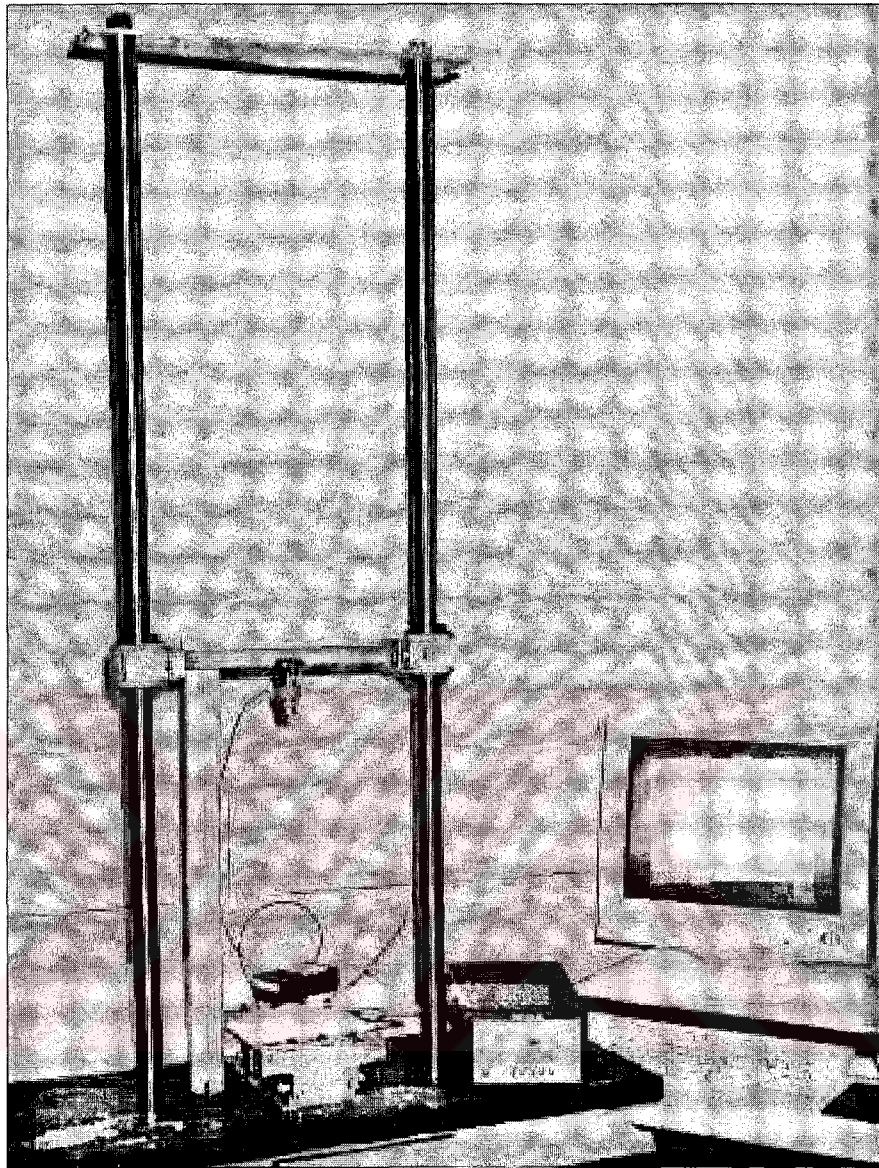
(a)
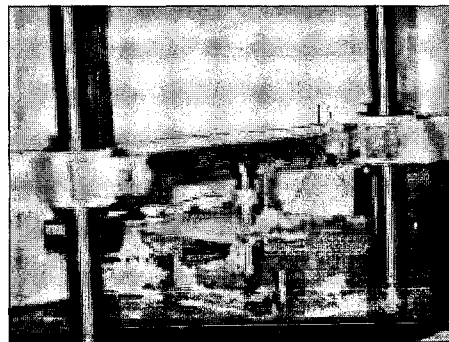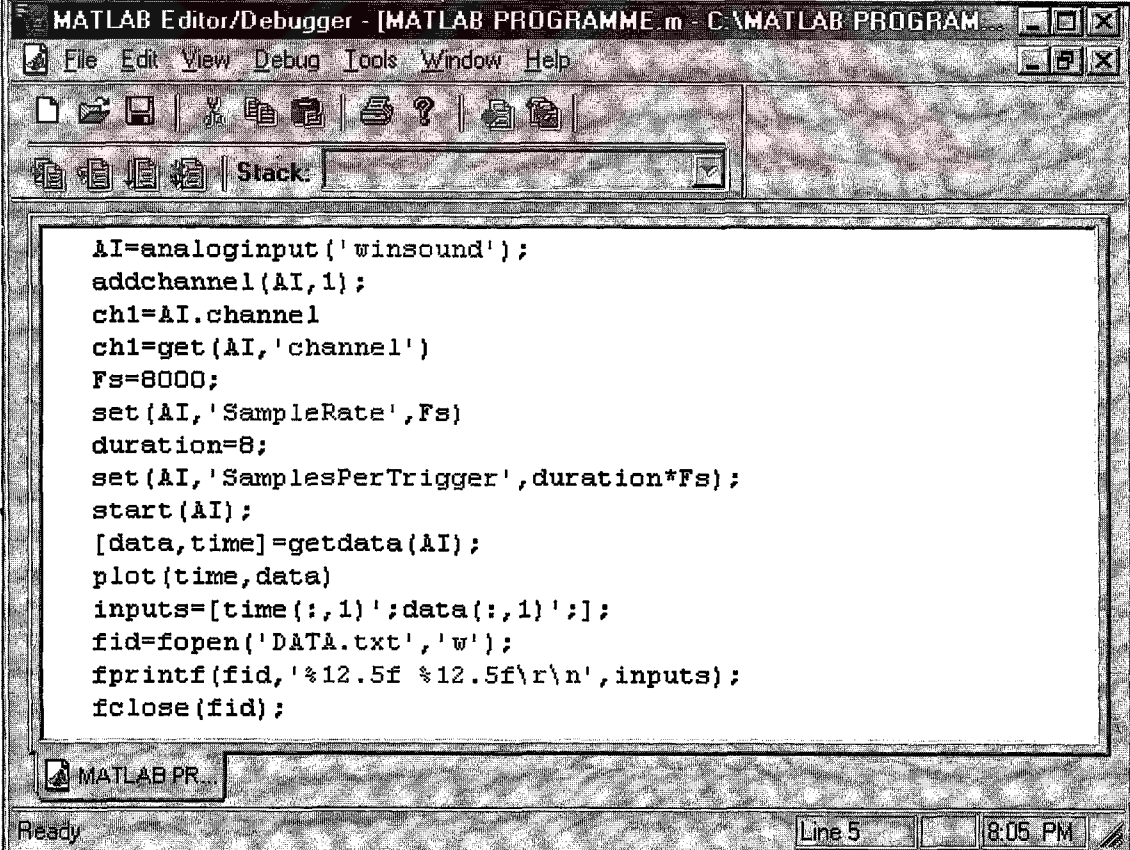
(b)

Figure 5.3 The photograph of drop-weight impact test system
(a) before impact (b) after impact.

Toolbox. The Data Acquisition Toolbox allows us to read data directly into Matlab from sound card, which is displayed as a PSD image. This uses the Matlab signal processing and visualization capabilities. The programme for Matlab Data Acquisition Toolbox is given in Table 5.1. The first step is to create the analog input object (AI) for the sound card. Next, we add a single channel to AI, and set the sample rate to 8000 Hz with acquisition duration of t seconds. The default trigger is to start collecting data as soon as the start command is issued. The acquisition ends once all the data is acquired.

Prior to impacting, the specimens are tightly clamped on both ends to a target holder, resulting in a 150 mm span. All tests are performed at room temperature. The impact point is on the center of the plate.

Table 5.1 The programme for Matlab Data Acquisition Toolbox.

```
AI=analoginput('winsound');
addchannel(AI,1);
ch1=AI.channel
ch1=get(AI,'channel')
Fs=8000;
set(AI,'SampleRate',Fs)
duration=8;
set(AI,'SamplesPerTrigger',duration*Fs);
start(AI);
[data,time]=getdata(AI);
plot(time,data)
inputs=[time(:,1)';data(:,1)';];
fid=fopen('DATA.txt','w');
fprintf(fid,'%12.5f %12.5f\r\n',inputs);
fclose(fid);
```

CHAPTER SIX
RESULTS AND DISCUSSION

6.1 Introduction

The impact behavior of E-glass/epoxy laminated composite plates under low velocities is considered experimentally and numerically. The projectile is a hemispherical tip-ended rigid impactor and the targets are square and rectangular composite plates. A range of laminated E-glass/epoxy composite plates is impacted under different impact conditions using a drop-weight apparatus. During each test, the drop-weight is released at a certain height to hit the center of the specimen. The contact force versus time is measured by a piezoelectric force transducer (Brüel & Kjaer), mounted on the impactor head. The following parameters are considered in the impact tests:

a) impact velocity
b) impactor mass
c) plate in-plane dimensions
d) plate thickness
e) variations in fiber form
f) variations in fiber orientation

A numerical evaluation of these specimens is also carried out by using 3DIMPACT transient dynamic finite element analysis code. The transient contact forces between the impactor and the laminated composite plate, stresses and strains during impact and maximum transverse deflection at the center are calculated numerically. Furthermore, a failure analysis for predicting the threshold of impact damage and initiation of delaminations is carried out numerically as functions of time.

In all cases, the projectile's Young's modulus and hardness are greater than the through-thickness Young's modulus and hardness of the specimen material. Therefore, the impacting projectile is regarded as rigid. The mechanical properties of the rigid impactor are given in Table 6.1.

6.2 Parameters

Different 6-ply and 8-ply symmetric laminates with $(0^0/90^0/0^0)_s$, $(0^0/-45^0/+45^0)_s$, $(0^0/0^0/90^0/90^0)_s$, $(0^0/90^0/0^0/90^0)_s$ and $(0^0,90^0)_6$ stacking sequences are considered. Impact tests are performed at increasing velocities (1 m/sec, 2 m/sec and 3 m/sec) and increasing masses (135 g and 2600 g) on clamped composite plates. All impact tests have been carried out with plate dimensions of 150 mm by 150 mm, 150 mm by 100 mm and 150 mm by 50 mm. Prior to impacting, the specimens are tightly clamped on both ends to a target holder, resulting in a 150 mm span. All impact conditions are summarized as follows and the details of the impact parameters are given in Table 6.2.

Characterization of impact regimes

- 72 specimens with impacts using 18 mm hemispherical-nosed impactors with masses of 135 g and 2600 g.
- Plate thickness (t): 1.4 mm, 2.8 mm, 3.4 mm, 4.4 mm and 4.8 mm.
- Plate span (S) x width (W): 150 mm by 150 mm, 150 mm by 100 mm and 150 mm by 50 mm (the nominal length of each plate is 150 mm).
- Clamping conditions: two opposite sides clamped resulting in a 150 mm span and the other two free.
- Four impact energies: 1.3 J, 5.2 J, 11.7 J and 0.6075 J.
- Corresponding velocities: 1 m/sec (2600 g), 2 m/sec (2600 g), 3 m/sec (2600 g), and 3 m/sec (135 g).
- Measured quantity: impact force.

Table 6.1 The mechanical properties of the rigid impactor.

Symbol	Value	Property
E	210 GPa	Young's modulus
ρ	7850 kg/m^3	density
ν	0.3	Poisson's ratio

The results are arranged in groups, each group contain the effect of certain parameters on the dynamic behavior of laminated composite plate. Firstly, the contact force-time histories are recorded during drop-weight impacts and calculated numerically. The numerical and experimental results are compared and excellent agreement is found between the comparisons. Later, the effect of impact velocity, impactor mass, and in-plane dimensions of the laminated composite plate is investigated using 8-ply laminates with $(0^0/90^0/0^0/90^0)_s$ lay-up, 6-ply laminates with $(0^0/-45^0/45^0)_s$ lay-up and 6-ply woven reinforced laminates with $(0^0,90^0)_6$ lay-up. Finally, the effect of thickness is evaluated using 6-ply woven reinforced laminates with two nominal thicknesses with averages of 1.4 mm and 2.8 mm.

Table 6.2 The impact parameters.

Fiber Orientation	Plate In-Plane Dimension					
	150 mm by 150 mm		150 mm by 100 mm		150 mm by 50 mm	
	Velocity (m/sec)	Mass (g)	Velocity (m/sec)	Mass (g)	Velocity (m/sec)	Mass (g)
$(0^0/90^0/0^0/90^0)_s$	[1] 1	2600	[5] 1	2600	[9] 1	2600
	[2] 2	2600	[6] 2	2600	[10] 2	2600
	[3] 3	2600	[7] 3	2600	[11] 3	2600
thickness=4.8 mm	[4] 3	135	[8] 3	135	[12] 3	135
$(0^0/90^0/0^0)_s$	[13] 1	2600	[17] 1	2600	[21] 1	2600
	[14] 2	2600	[18] 2	2600	[22] 2	2600
	[15] 3	2600	[19] 3	2600	[23] 3	2600
thickness=3.4 mm	[16] 3	135	[20] 3	135	[24] 3	135
$(0^0/0^0/90^0/90^0)_s$	[25] 1	2600	[29] 1	2600	[33] 1	2600
	[26] 2	2600	[30] 2	2600	[34] 2	2600
	[27] 3	2600	[31] 3	2600	[35] 3	2600
thickness=4.8 mm	[28] 3	135	[32] 3	135	[36] 3	135
$(0^0/-45^0/+45^0)_s$	[37] 1	2600	[41] 1	2600	[45] 1	2600
	[38] 2	2600	[42] 2	2600	[46] 2	2600
	[39] 3	2600	[43] 3	2600	[47] 3	2600
thickness=4.4 mm	[40] 3	135	[44] 3	135	[48] 3	135
$(0^0,90^0)_6$	[49] 1	2600	[53] 1	2600	[57] 1	2600
	[50] 2	2600	[54] 2	2600	[58] 2	2600
	[51] 3	2600	[55] 3	2600	[59] 3	2600
thickness=1.4 mm	[52] 3	135	[56] 3	135	[60] 3	135
$(0^0,90^0)_6$	[61] 1	2600	[65] 1	2600	[69] 1	2600
	[62] 2	2600	[66] 2	2600	[70] 2	2600
	[63] 3	2600	[67] 3	2600	[71] 3	2600
thickness=2.8 mm	[64] 3	135	[68] 3	135	[72] 3	135

6.3 Contact Force Between Impactor and Laminate

6.3.1 Plates $(0^0/90^0/0^0/90^0)_s$

Low velocity impact loading tests are performed at increasing velocities (1, 2 and 3 m/sec) and increasing masses (135 g and 2600 g) on clamped plates in order to determine the dynamic behavior of laminated composite material. Figure 6.1 shows oscilloscope trace of the force-time histories recorded during drop-weight impacts. It is worth noting that during impact, the contact forces are reduced to zero for a certain period of time, during which the impactor was separated from the plate. The plate and the impactor contacted again after the plate reversed its direction of motion and snapped back. Similar results were observed analytically by Chen & Sun (1985), Wu & Chang (1989) and experimentally by Lagace (1986).

Figures 6.2-6.13 show the impact force-time histories recorded during drop-weight impacts and calculated numerically from 3DIMPACT computer code of composite laminates with $(0^0/90^0/0^0/90^0)_s$ lay-up. In the present thesis, only the first impact is considered. The impact force-time histories for 150 mm by 150 mm square specimen are given in Figures 6.2-6.5.
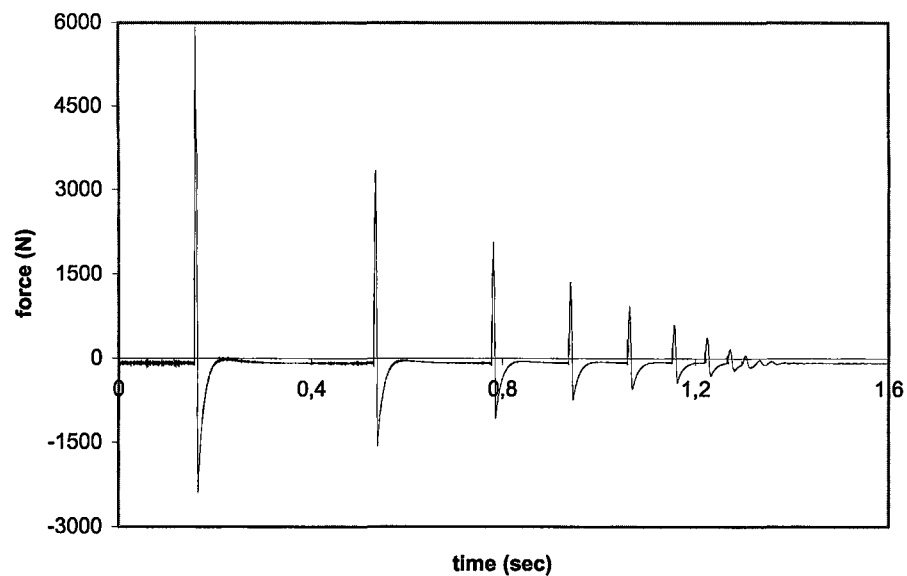
Figure 6.1 Oscilloscope trace of the force-time histories $((0^0/90^0/0^0/90^0)_s$ lay-up, 150 mm by 150 mm, 3 m/sec and 2600 g).

In addition to effective impact zones of 150 mm by 150 mm, other effective impact zones of 150 mm by 100 mm and 150 mm by 50 mm, i.e. intermediate and small rectangular specimens, are investigated for in-plane dimensional effects. For 150 mm by 100 mm and 150 mm by 50 mm rectangular specimens, the impact responses are shown in Figures 6.6-6.13, respectively. Most of the analysis curves capture the multiple small oscillations superimposed on the measured force-time curve. These oscillations, which represent the plate vibrations, are characteristics of large-mass, low-velocity impact events where the contact duration is sufficiently long for flexural waves to reach the plate boundaries and reflect back several times. In Figure 6.4, a relatively high frequency oscillation is found to superimpose on the basic load-time curve. This oscillating signal seems to be related to the damage growth during impact (Wang & Vukhanh, 1994). It occurred and lasted during the loading period, and ceased when unloading began, possibly implying that the damage growth finished around the time of maximum impact load.

All figures show comparison of experimental and FE computed force-time history at the center of the laminated composite plate. Note that the calculated impact force between the impactor and the target has a higher value than that measured by the impact force transducer. The duration of impact events in the test results is more than that obtained from the analysis. The discrepancies between the computed and experimental results could also be due to the fact that the boundaries of the plate in the experimental analysis are not as perfectly clamped as reported. This may be because the metal support that held the impacted laminate allowed the laminate to move horizontally and also to rotate a small amount.

If the force-time histories of $(0^0/90^0/0^0/90^0)_s$ lay-up (Figure 6.2-6.13) and $(0^0/0^0/90^0/90^0)_s$ lay-up (Figure 9.1-9.12) are compared, it is seen that the differences between the results are not significant. The results on the center deflection, stresses and strains histories, and delaminated area of 8-ply laminates with $(0^0/90^0/0^0/90^0)_s$ lay-up and $(0^0/0^0/90^0/90^0)_s$ lay-up are nearly same. Therefore, the center deflection, stresses and strains, and delaminated area results of 8-ply laminates with $(0^0/0^0/90^0/90^0)_s$ lay-up are not given in thesis.
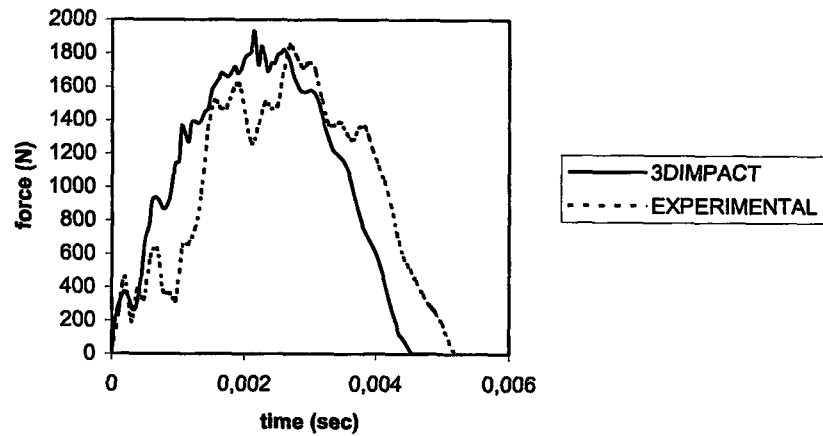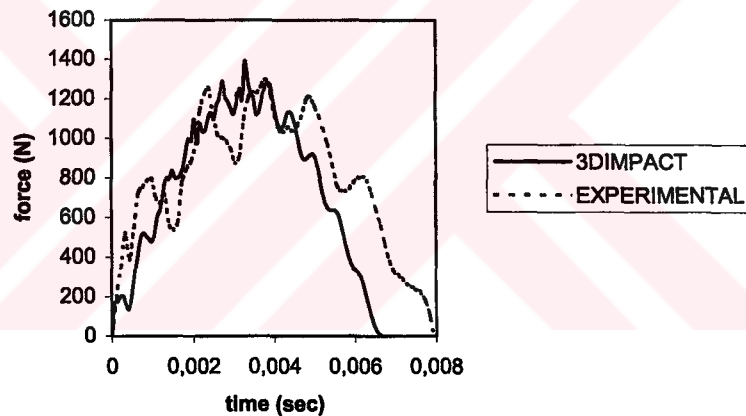
Figure 6.2 Impact force-time history of $(0^0/90^0/0^0/90^0)_s$ laminate under the impact velocity V=1 m/sec and impactor mass m=2600 g (150 mm by 150 mm).
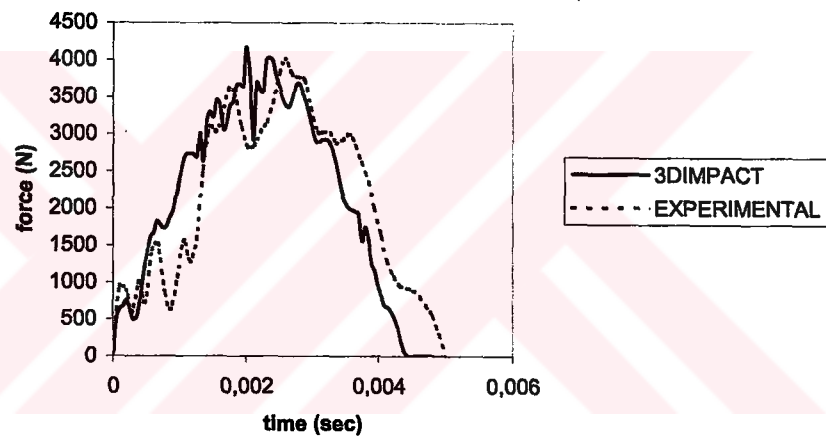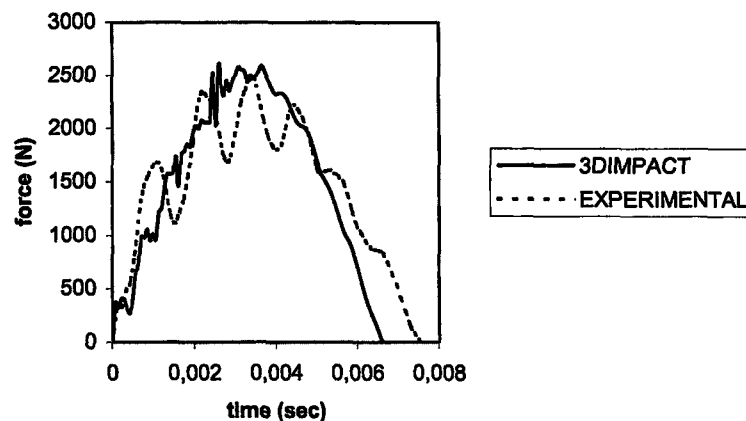
Figure 6.3 Impact force-time history of $(0^0/90^0/0^0/90^0)_s$ laminate under the impact velocity V=2 m/sec and impactor mass m=2600 g (150 mm by 150 mm).
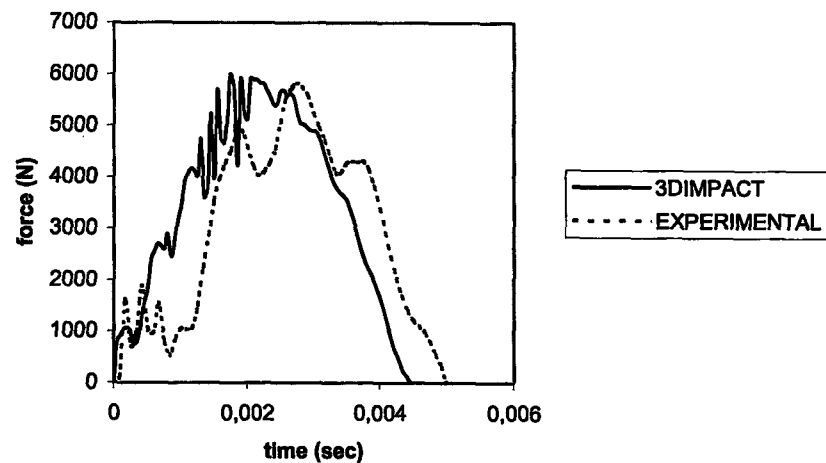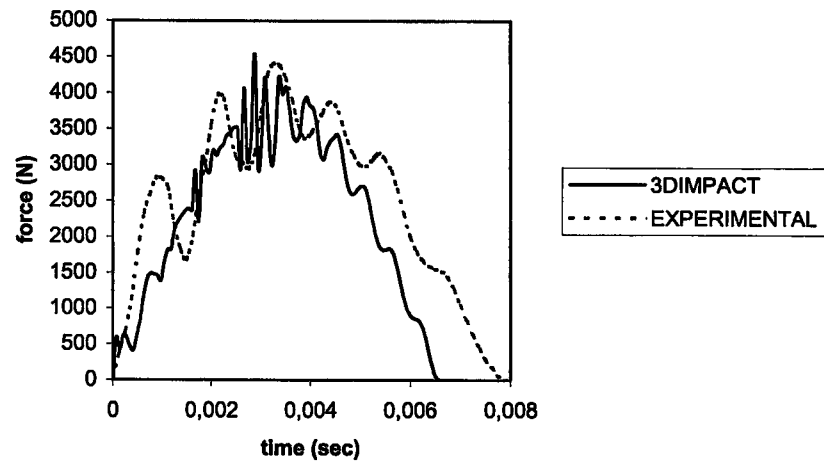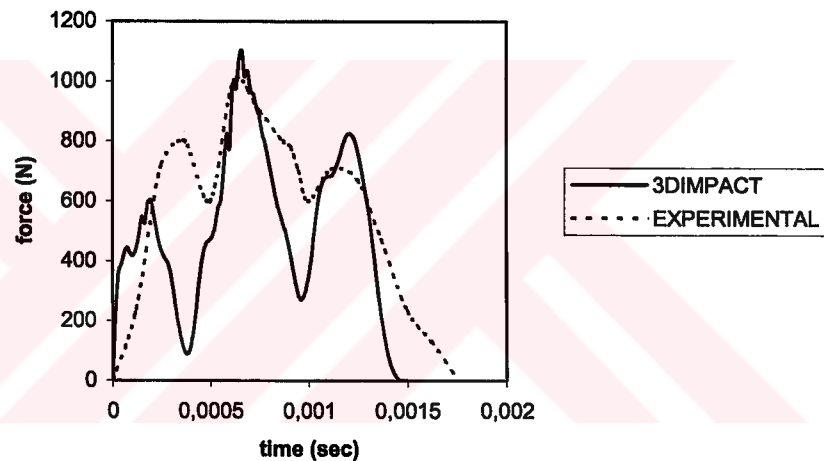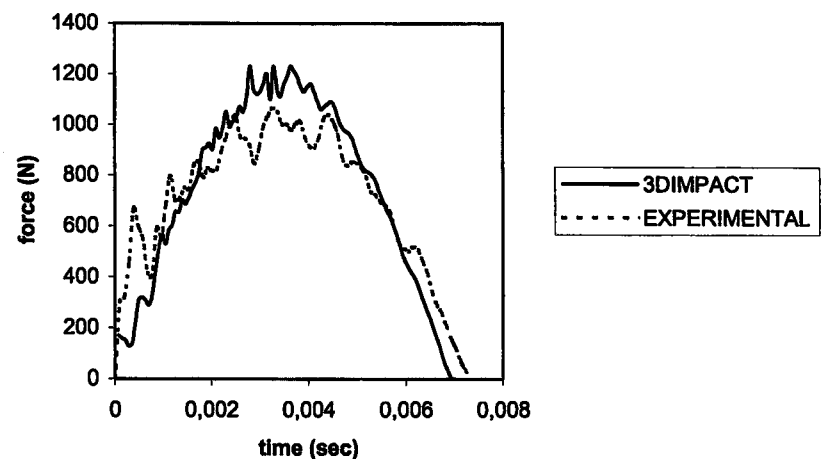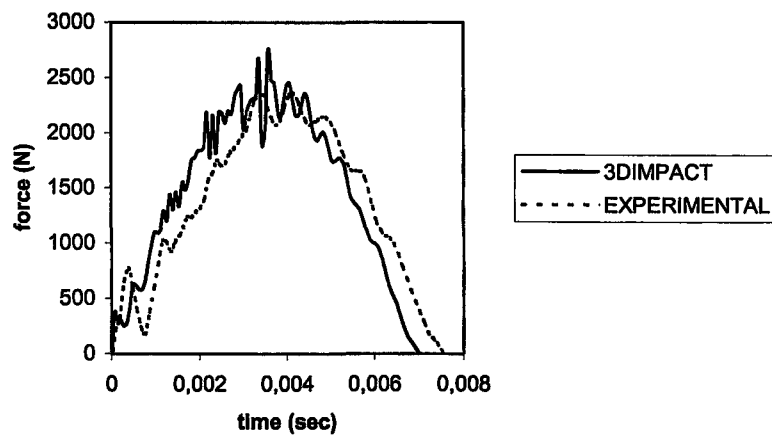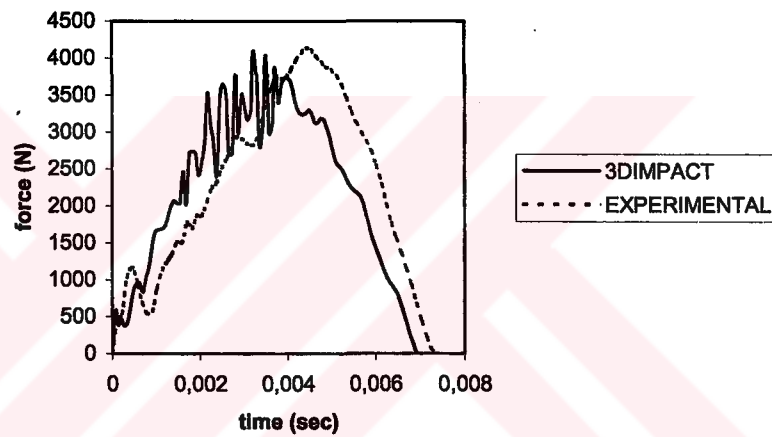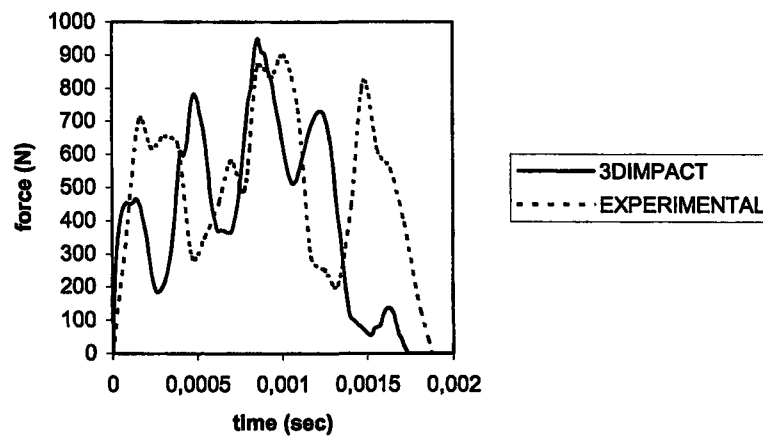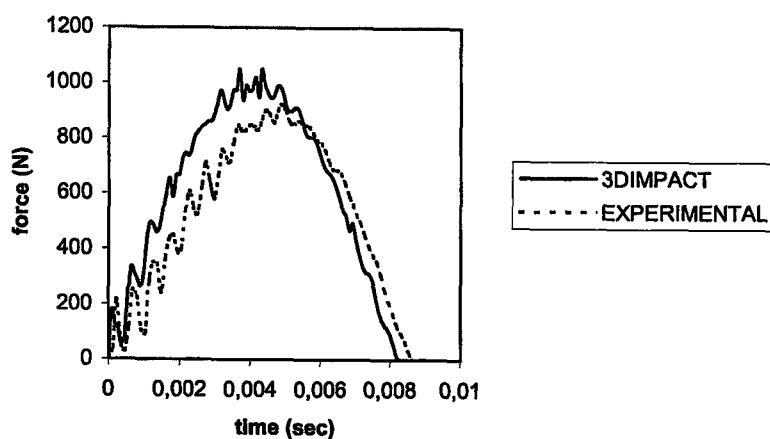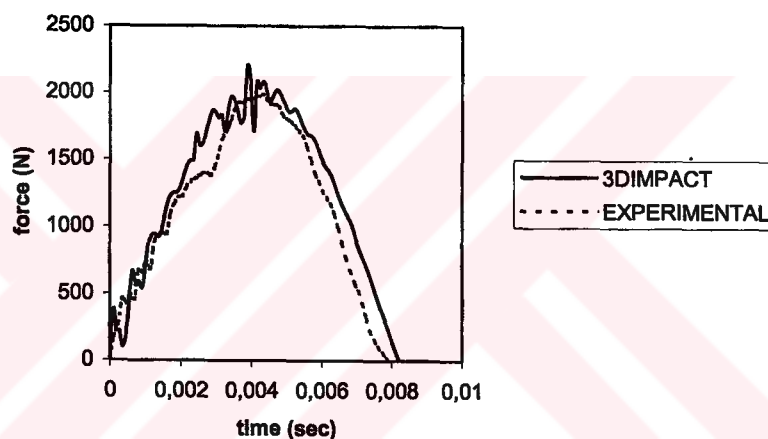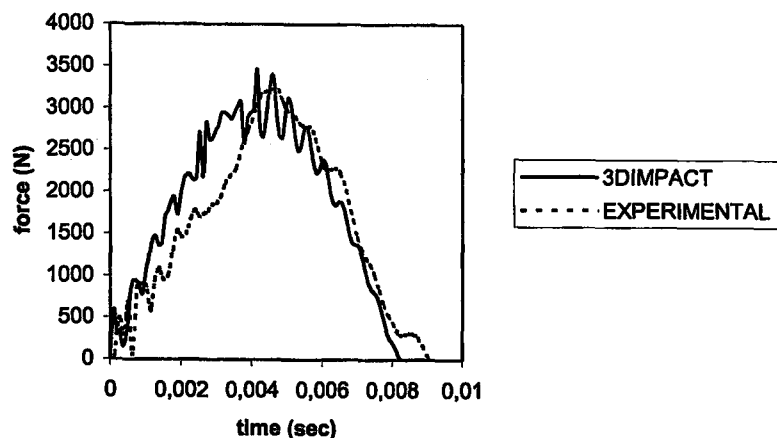
Figure 6.4 Impact force-time history of $(0^0/90^0/0^0/90^0)_s$ laminate under the impact velocity V=3 m/sec and impactor mass m=2600 g (150 mm by 150 mm).
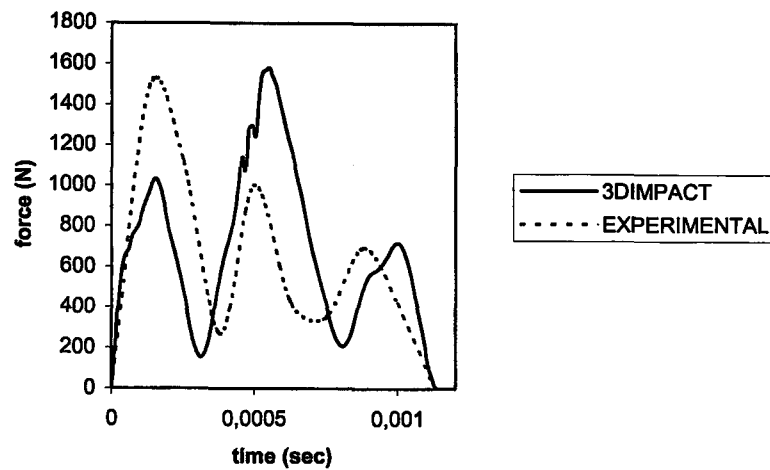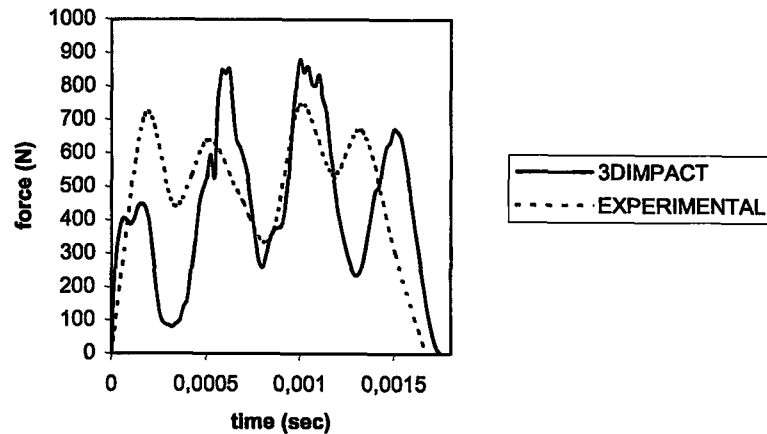
Figure 6.5 Impact force-time history of $(0^0/90^0/0^0/90^0)_s$ laminate under the impact velocity V=3 m/sec and impactor mass m=135 g (150 mm by 150 mm).
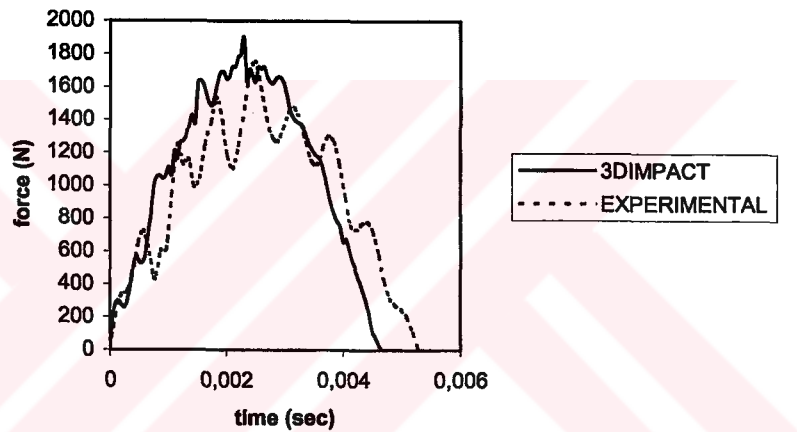
Figure 6.6 Impact force-time history of $(0^0/90^0/0^0/90^0)_s$ laminate under the impact velocity V=1 m/sec and impactor mass m=2600 g (150 mm by 100 mm).
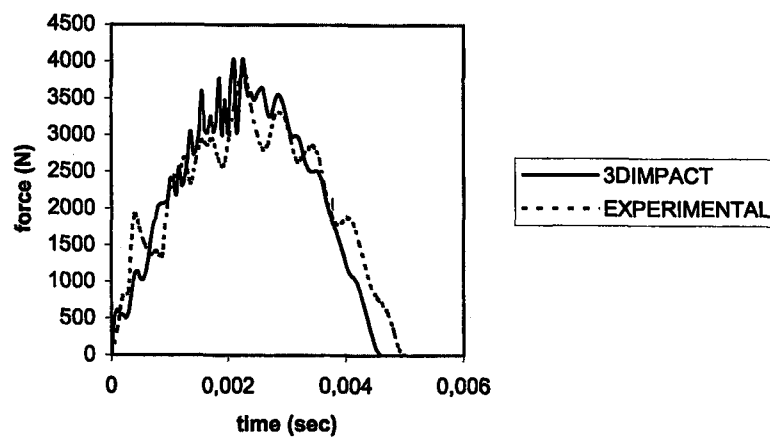
Figure 6.7 Impact force-time history of $(0^0/90^0/0^0/90^0)_s$ laminate under the impact velocity V=2 m/sec and impactor mass m=2600 g (150 mm by 100 mm).
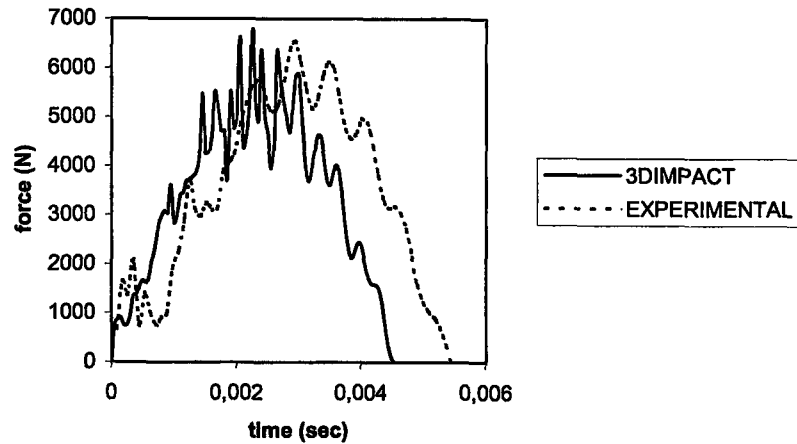
Figure 6.8 Impact force-time history of $(0^0/90^0/0^0/90^0)_s$ laminate under the impact velocity V=3 m/sec and impactor mass m=2600 g (150 mm by 100 mm).
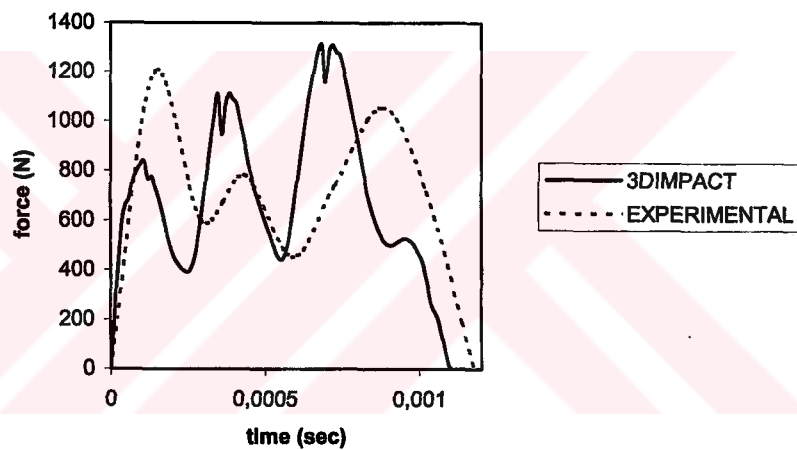
Figure 6.9 Impact force-time history of $(0^0/90^0/0^0/90^0)_s$ laminate under the impact velocity V=3 m/sec and impactor mass m=135 g (150 mm by 100 mm).
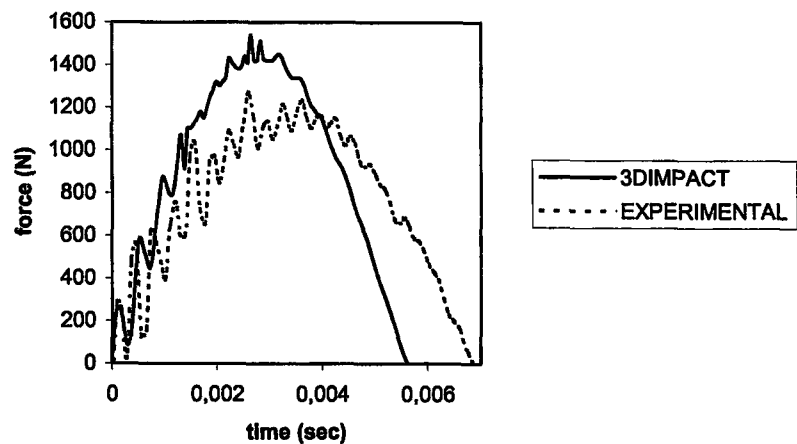
Figure 6.10 Impact force-time history of $(0^0/90^0/0^0/90^0)_s$ laminate under the impact velocity V=1 m/sec and impactor mass m=2600 g (150 mm by 50 mm).
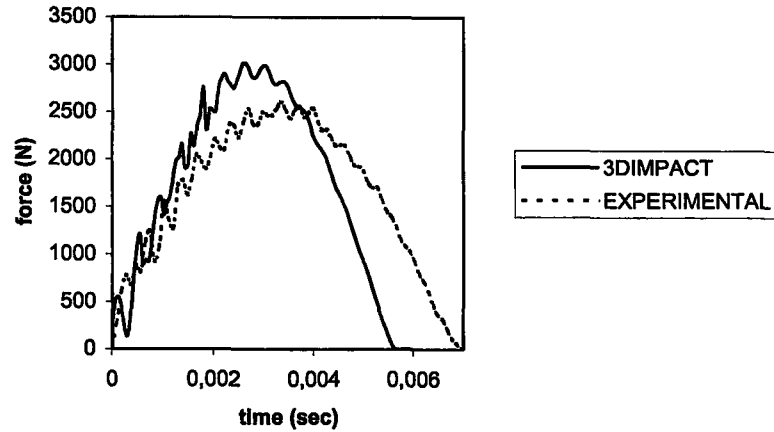
Figure 6.11 Impact force-time history of $(0^0/90^0/0^0/90^0)_s$ laminate under the impact velocity V=2 m/sec and impactor mass m=2600 g (150 mm by 50 mm).
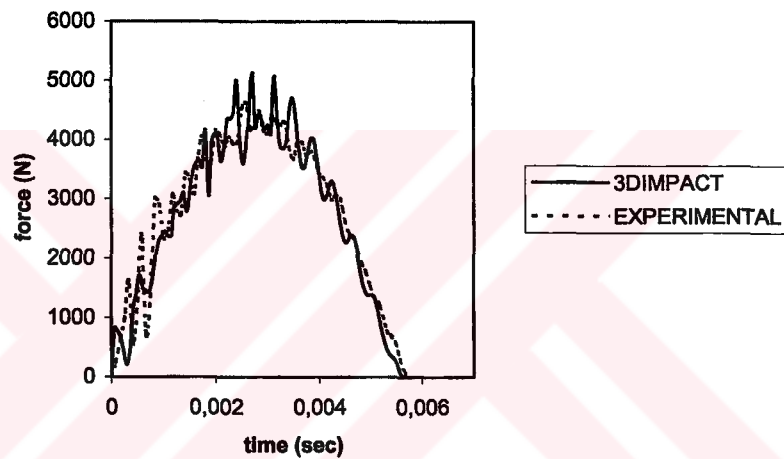
Figure 6.12 Impact force-time history of $(0^0/90^0/0^0/90^0)_s$ laminate under the impact velocity V=3 m/sec and impactor mass m=2600 g (150 mm by 50 mm).
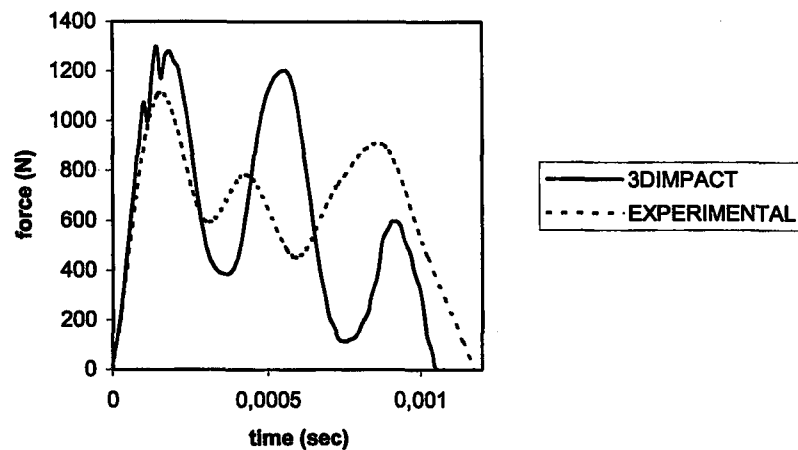
Figure 6.13 Impact force-time history of $(0^0/90^0/0^0/90^0)_s$ laminate under the impact velocity V=3 m/sec and impactor mass m=135 g (150 mm by 50 mm).

6.3.2 Plates $(0^0/90^0/0^0)_s$

Figures 6.14-6.25 show the comparison between the predicted and measured impact force histories using 6-ply unidirectional reinforced laminates with $(0^0/90^0/0^0)_s$ lay-up for three different in-plane dimensions. As shown in Figures 6.2-6.25, the force magnitudes of the 8–ply laminates with $(0^0/90^0/0^0/90^0)_s$ are greater than the 6-ply laminates with $(0^0/90^0/0^0)_s$ and the contact duration of the 8-ply laminates is smaller than the 6-ply laminates. This may be because the thickness of the 6-ply laminates is less than the 8-ply laminates. It can be concluded that the higher the thickness of the composite laminate, the higher the peak force. But the contact time duration decreases with increasing thickness. This behavior is essentially the same for all the laminated plate dimensions.

Figure 6.14 Impact force-time history of $(0^0/90^0/0^0)_s$ laminate under the impact velocity V=1 m/sec and impactor mass m=2600 g (150 mm by 150 mm).

Figure 6.15 Impact force-time history of $(0^0/90^0/0^0)_s$ laminate under the impact velocity V=2 m/sec and impactor mass m=2600 g (150 mm by 150 mm).

Figure 6.16 Impact force-time history of $(0^0/90^0/0^0)_s$ laminate under the impact velocity V=3 m/sec and impactor mass m=2600 g (150 mm by 150 mm).

Figure 6.17 Impact force-time history of $(0^0/90^0/0^0)_s$ laminate under the impact velocity V=3 m/sec and impactor mass m=135 g (150 mm by 150 mm).

Figure 6.18 Impact force-time history of $(0^0/90^0/0^0)_s$ laminate under the impact velocity V=1 m/sec and impactor mass m=2600 g (150 mm by 100 mm).

Figure 6.19 Impact force-time history of $(0^0/90^0/0^0)_s$ laminate under the impact velocity V=2 m/sec and impactor mass m=2600 g (150 mm by 100 mm).

Figure 6.20 Impact force-time history of $(0^0/90^0/0^0)_s$ laminate under the impact velocity V=3 m/sec and impactor mass m=2600 g (150 mm by 100 mm).

Figure 6.21 Impact force-time history of $(0^0/90^0/0^0)_s$ laminate under the impact velocity V=3 m/sec and impactor mass m=135 g (150 mm by 100 mm).

Figure 6.22 Impact force-time history of $(0^0/90^0/0^0)_s$ laminate under the impact velocity V=1 m/sec and impactor mass m=2600 g (150 mm by 50 mm).

Figure 6.23 Impact force-time history of $(0^0/90^0/0^0)_s$ laminate under the impact velocity V=2 m/sec and impactor mass m=2600 g (150 mm by 50 mm).

Figure 6.24 Impact force-time history of $(0^0/90^0/0^0)_s$ laminate under the impact velocity V=3 m/sec and impactor mass m=2600 g (150 mm by 50 mm).

Figure 6.25 Impact force-time history of $(0^0/90^0/0^0)_s$ laminate under the impact velocity V=3 m/sec and impactor mass m=135 g (150 mm by 50 mm).

6.4 Impact Velocity Effects

Low velocity impact loading tests are performed at increasing velocities (1 m/sec, 2 m/sec and 3 m/sec) on clamped plates in order to determine the effect of the projectile velocity on the impact behavior of the composite laminate. Figure 6.26 shows the force-time histories recorded during drop-weight impacts and calculated numerically from 3DIMPACT computer code of 8-ply laminates with $(0^0/90^0/0^0/90^0)_s$ for the same plate dimensions (150 mm by 150 mm) at three different impact velocity levels. With the impactor mass held constant at 2600 g, the velocity is varied for three cases: (a) 1 m/sec, (b) 2 m/sec and (c) 3 m/sec. The measured maximum contact forces are 1847 N, 4013 N and 5825 N for the above impact velocities, respectively. It can be seen that the contact force is directly proportional to the impact velocity while the duration of contact is insensitive to it.

In accordance with other authors [(Choi & Chang, 1992) and (Choi et al., 1991 a, b)], the 3DIMPACT code simulation agreed fairly well with experimental tests at low-velocity impact. Thus, transient stresses and strains in the laminate plates, center deflection histories and delaminated area are calculated numerically from 3DIMPACT. Effect of impact velocity on center deflection histories of a laminated composite plate is given in Figure 6.27. The in-plane stresses σ_1, σ_2 and τ_{12} at (1, 1, 2.4 mm), which are the mid-point of the composite plate and on the upper surface of the laminations, are presented in Figure 6.28. The transverse shear stresses τ_{23}, τ_{13}

and σ_3 are checked at the same point. The time histories are plotted in Figure 6.29. The transverse shear stresses undergo more oscillations during impact and may lead up to delamination inside the composite plates. However, from the scale of the vertical axes, it can be found that the transverse shear stresses are significantly smaller then the in plane stresses σ_1 and σ_2. The similar results on the transverse stresses were also found in the finite element analysis by Wu & Chang (1989) and Chun & Lam (1998).

The in-plane strains ε_1, ε_2 and γ_{12} at (1, 1, 2.4 mm), which are the mid-point of the composite plate and on the upper surface of the laminations, are presented in Figure 6.30. The transverse shear strains γ_{23}, γ_{13} and ε_3 are calculated at the same point. The time histories are given in Figure 6.31.

The numerical simulations of the delamination shape and size at the interface containing the major delamination of the laminates are shown in Figure 6.32. Major delamination occurs at the lower interface (the interface away from the impact side). The "asterisks" symbol in the figure indicates the location where the stresses are calculated and which satisfied the impact-induced delamination criterion. The area covered by the asterisks gives the estimation of the delamination size. The observed delamination geometry at this interface exhibit "peanut-shapes" and propagates along the fiber direction.

Figure 6.33 shows experimental and numerical comparisons of force-time histories of 6-ply laminates with $(0^0,-45^0,45^0)_s$ for three different impact velocity levels, 1 m/sec, 2 m/sec and 3 m/sec and an impactor mass of 2600 g. Effect of impact velocity on center deflection histories, stresses and strains and delaminated area is given in Figures 6.34-6.39 for 6-ply laminates with $(0^0,-45^0,45^0)_s$.

Concerning the effects of projectile velocity on the dynamic response of an impacted laminate, it is found that the impact forces and center deflections, transient stresses and strains, and delaminated area are directly proportional to the projectile velocity.
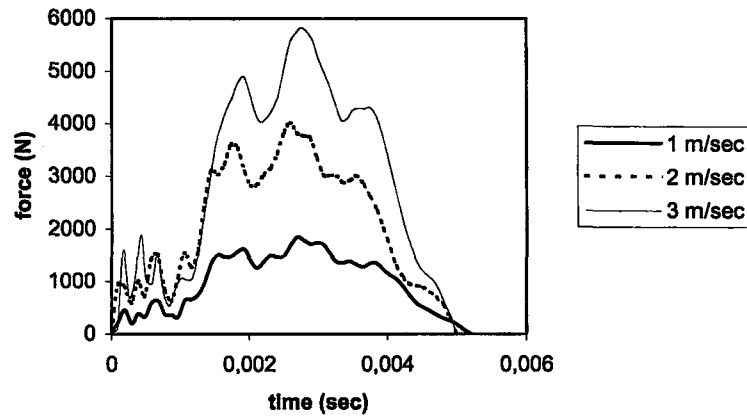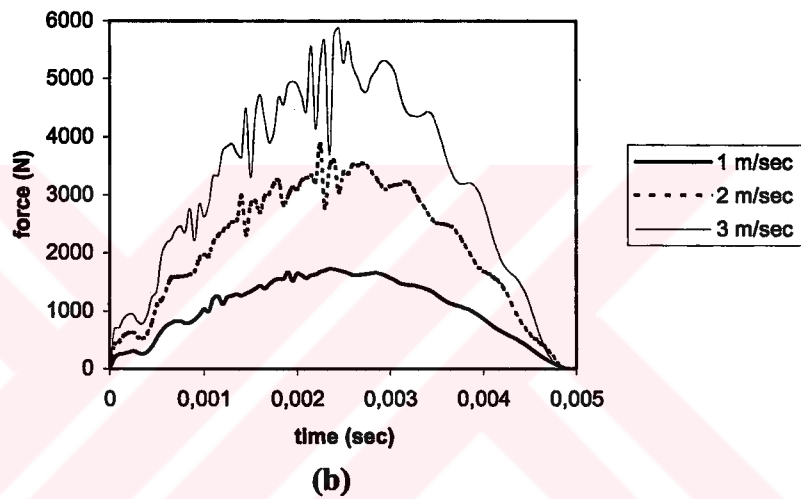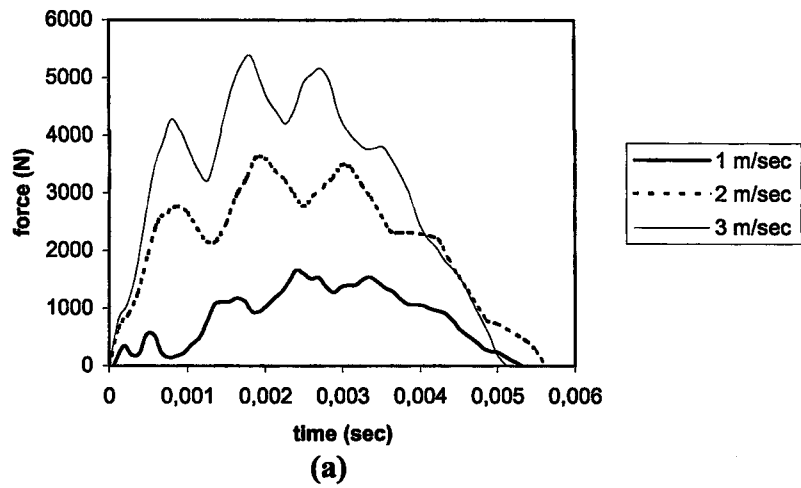
(a)
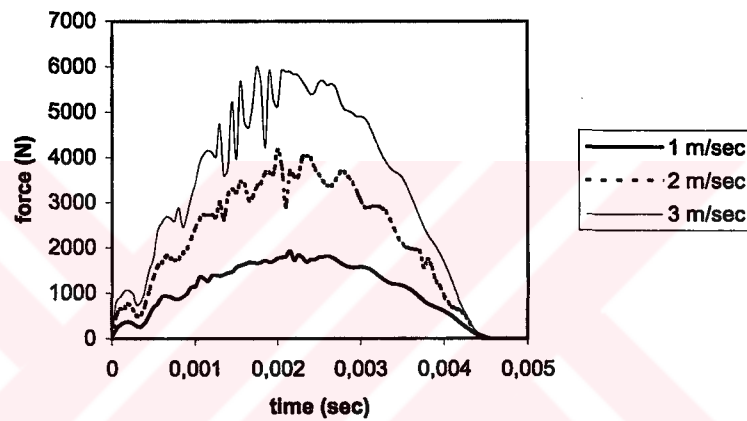
(b)

Figure 6.26 Comparison of force histories at three different impact velocity levels $((0^0/90^0/0^0/90^0)_s,$ 150 mm by 150 mm and 2600 g) **(a)** experimental response **(b)** predicted response.
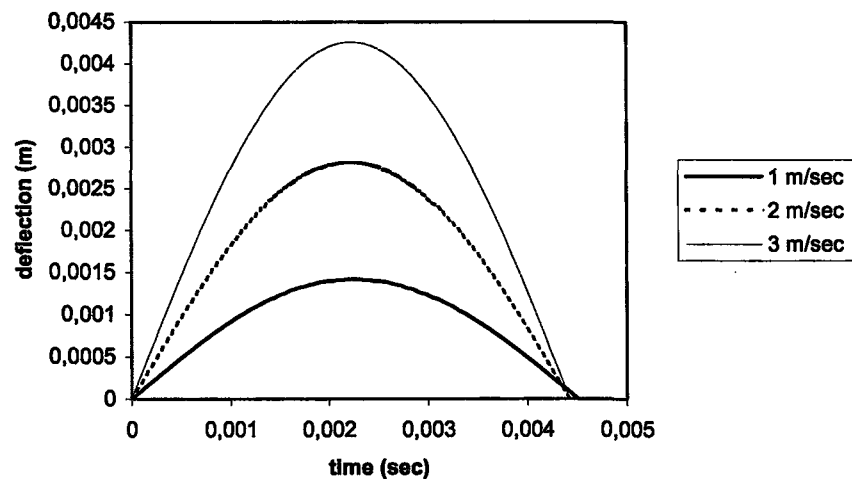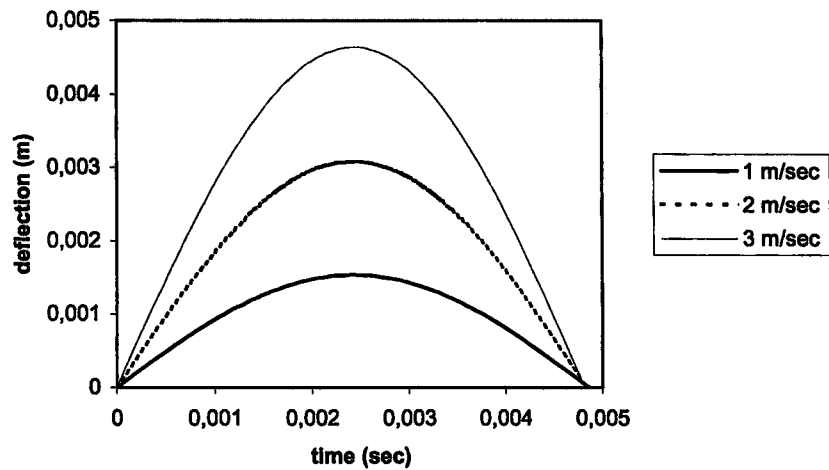

Figure 6.27 Comparison of center deflection histories at three different impact velocity levels $((0^0/90^0/0^0/90^0)_s,$ 150 mm by 150 mm and 2600 g).
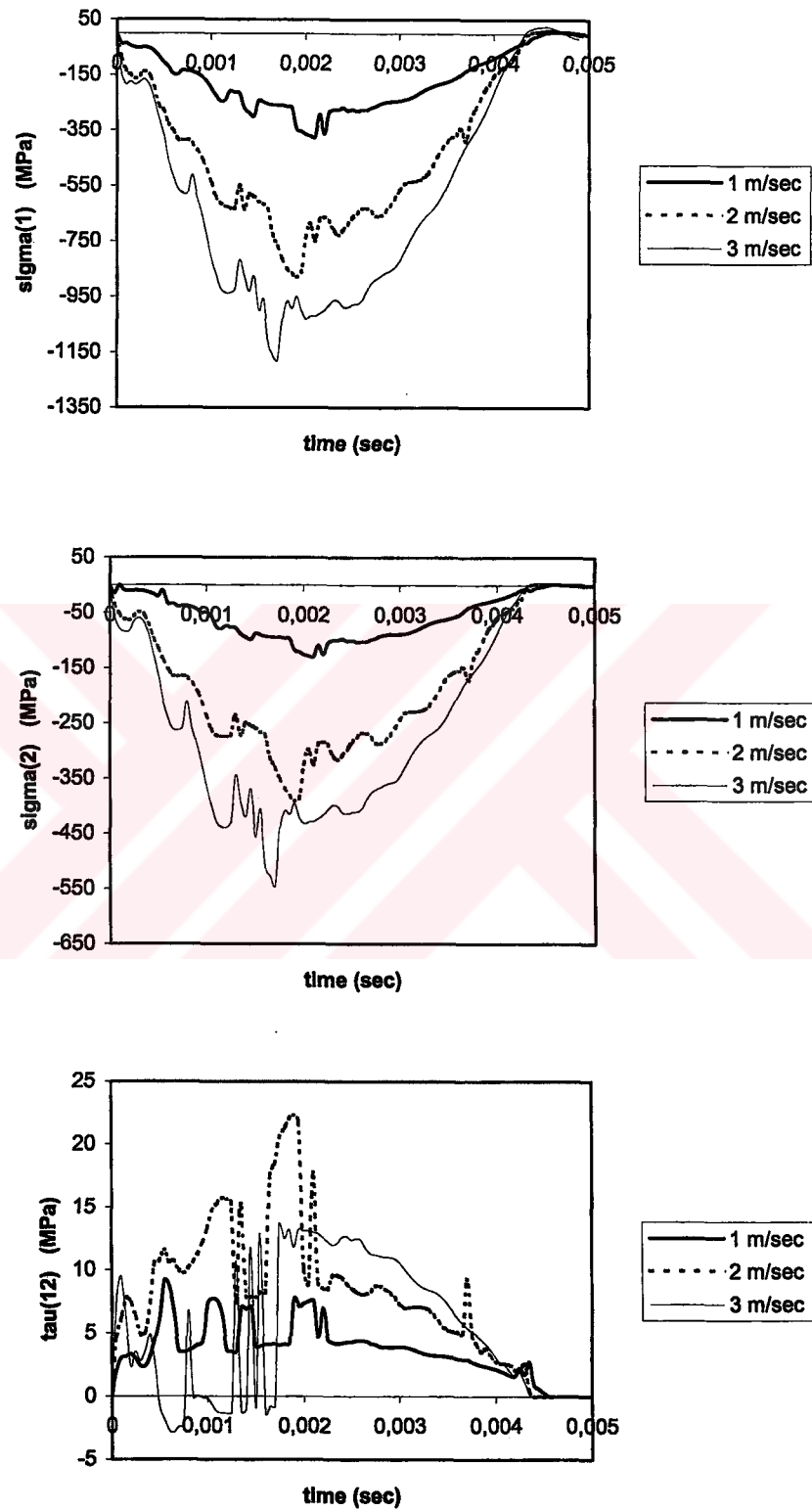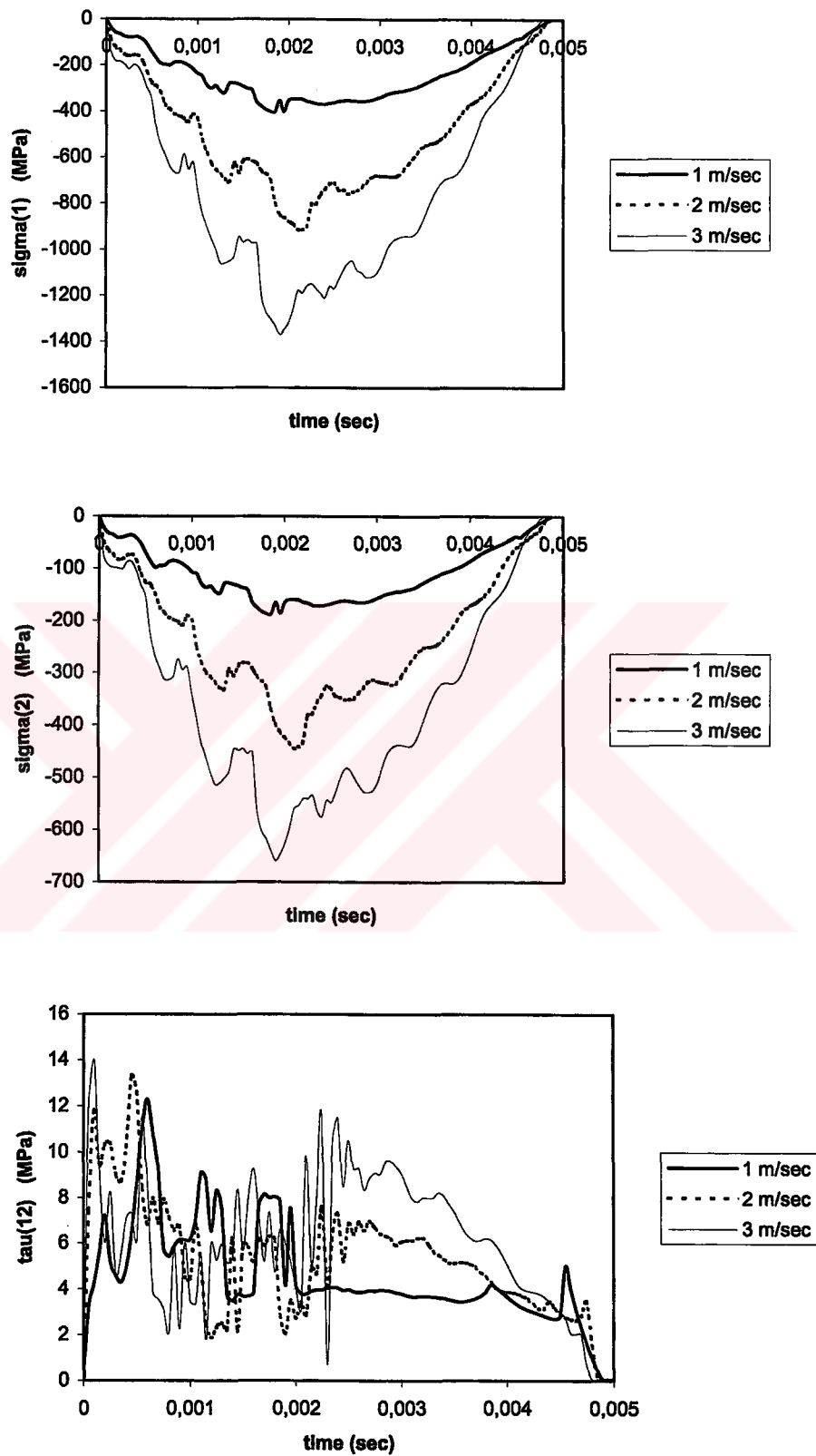
Figure 6.28 History of the stresses σ_1, σ_2 and τ_{12} at a given point (1, 1, 2.4 mm) calculated by 3DIMPACT at three different impact velocity levels $((0^0/90^0/0^0/90^0)_s$, 150 mm by 150 mm and 2600 g).
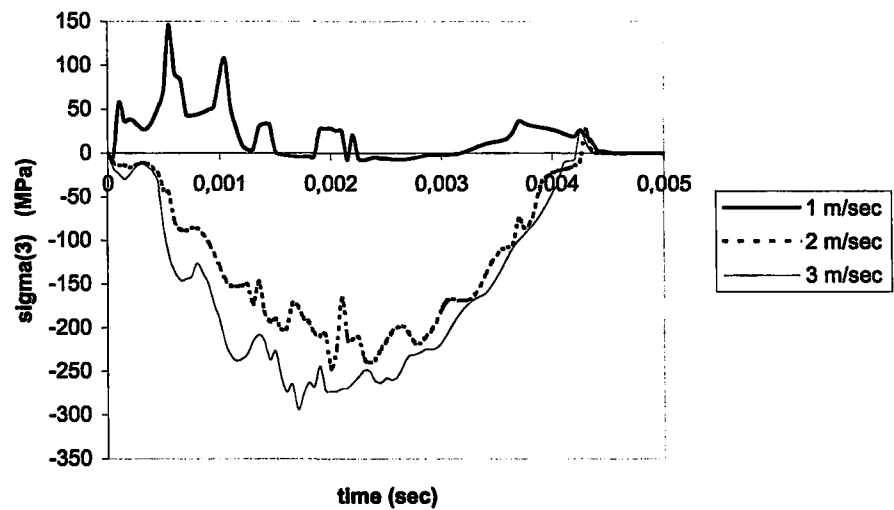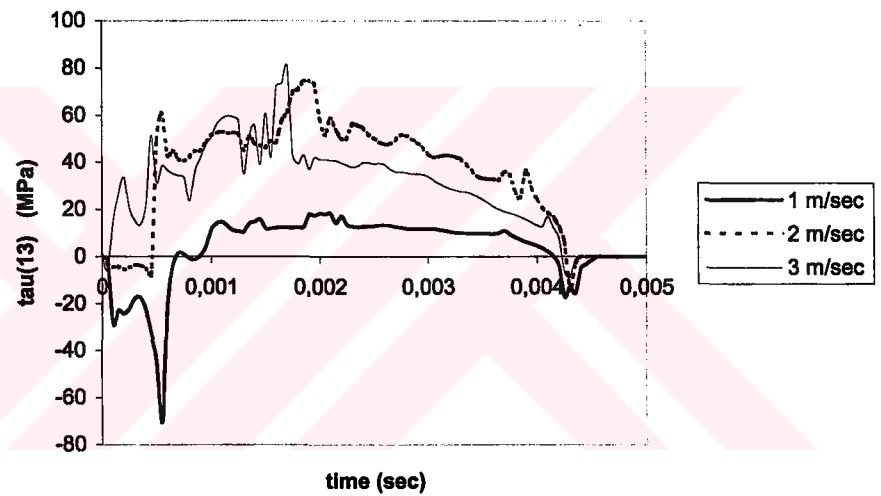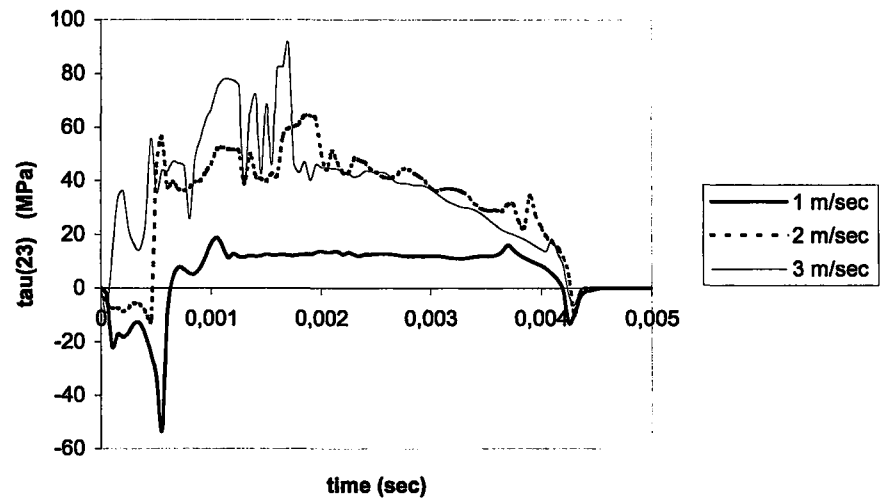
Figure 6.29 History of the stresses τ_{23}, τ_{13} and σ_3 at a given point (1, 1, 2.4 mm) calculated by 3DIMPACT at three different impact velocity levels $((0^0/90^0/0^0/90^0)_s$, 150 mm by 150 mm and 2600 g).
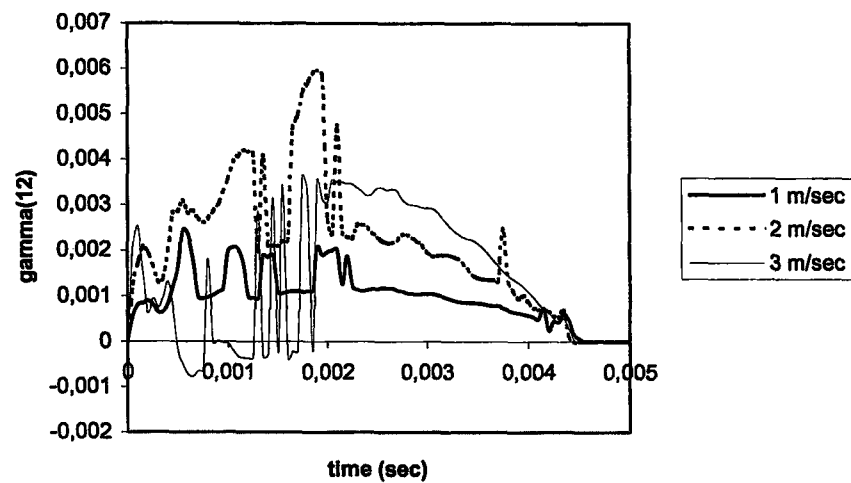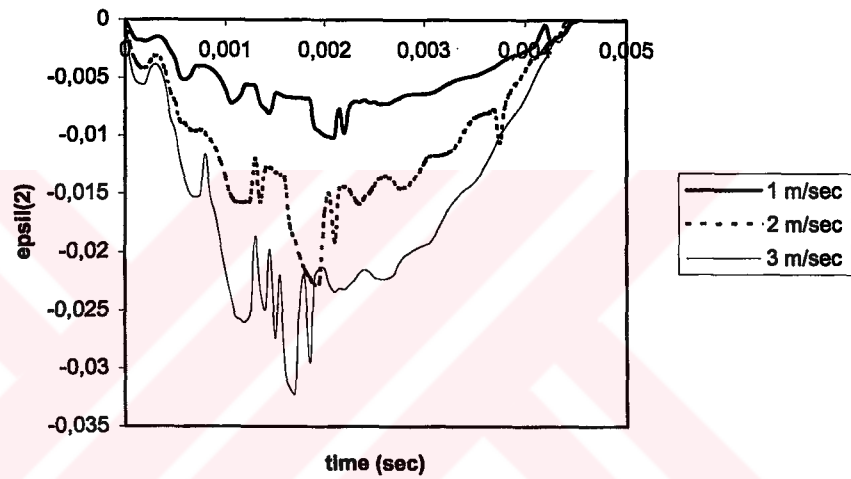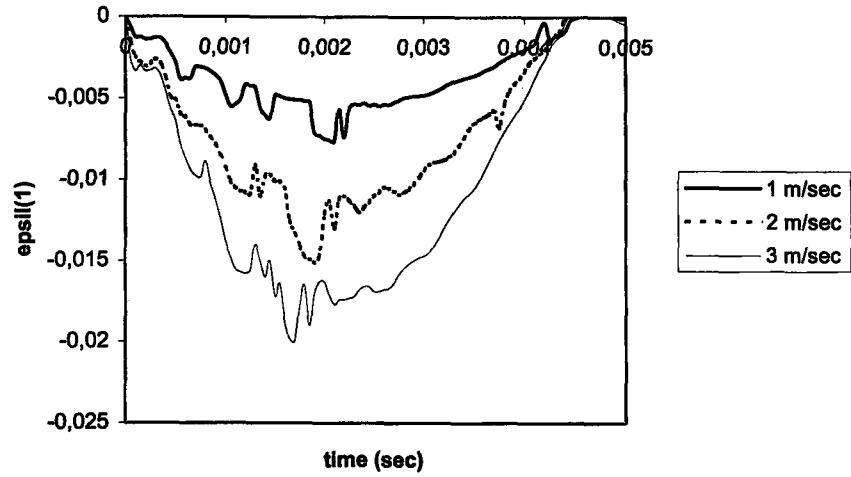
Figure 6.30 History of the strains ε_1, ε_2 and γ_{12} at a given point (1, 1, 2.4 mm) calculated by 3DIMPACT at three different impact velocity levels $((0^0/90^0/0^0/90^0)_s$, 150 mm by 150 mm and 2600 g).
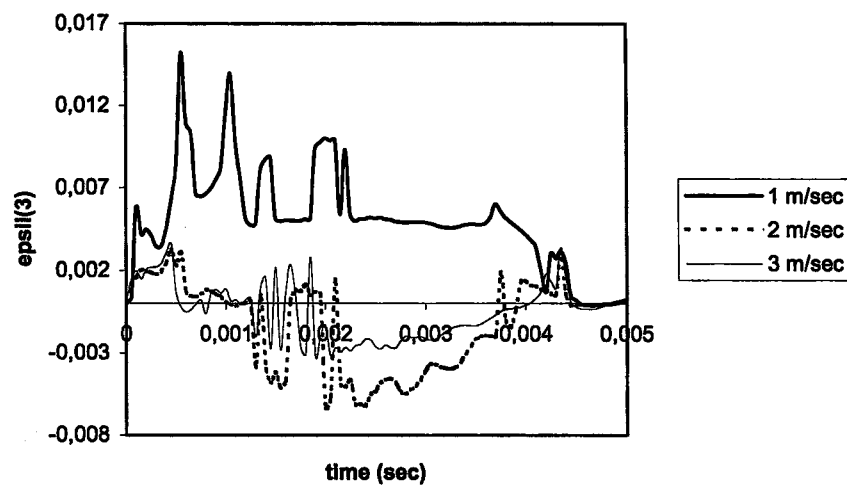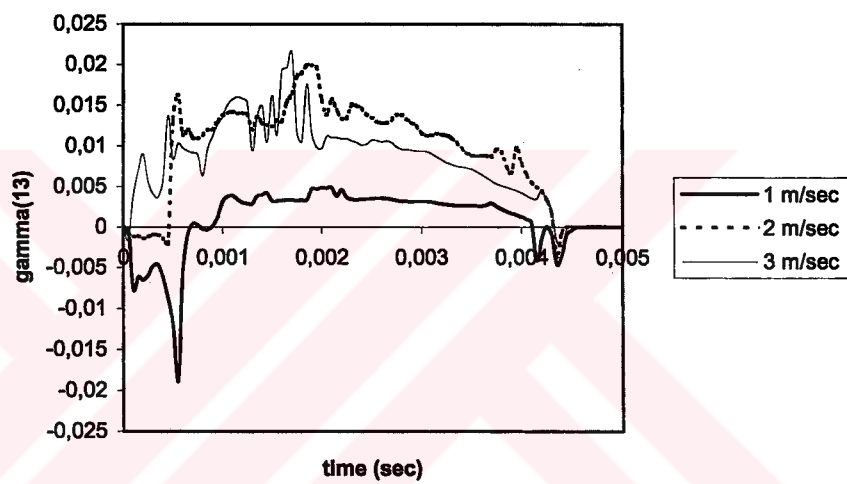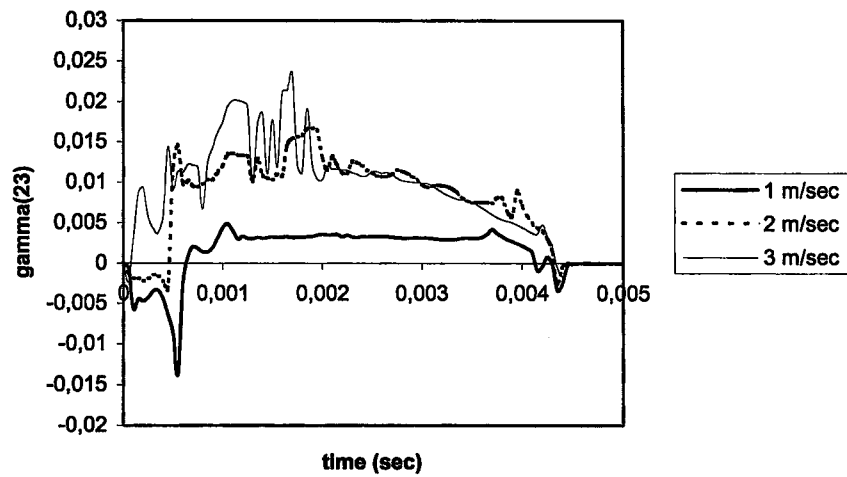
Figure 6.31 History of the strains γ_{23}, γ_{13} and ε_3 at a given point (1, 1, 2.4 mm) calculated by 3DIMPACT at three different impact velocity levels $((0^0/90^0/0^0/90^0)_s$, 150 mm by 150 mm and 2600 g).
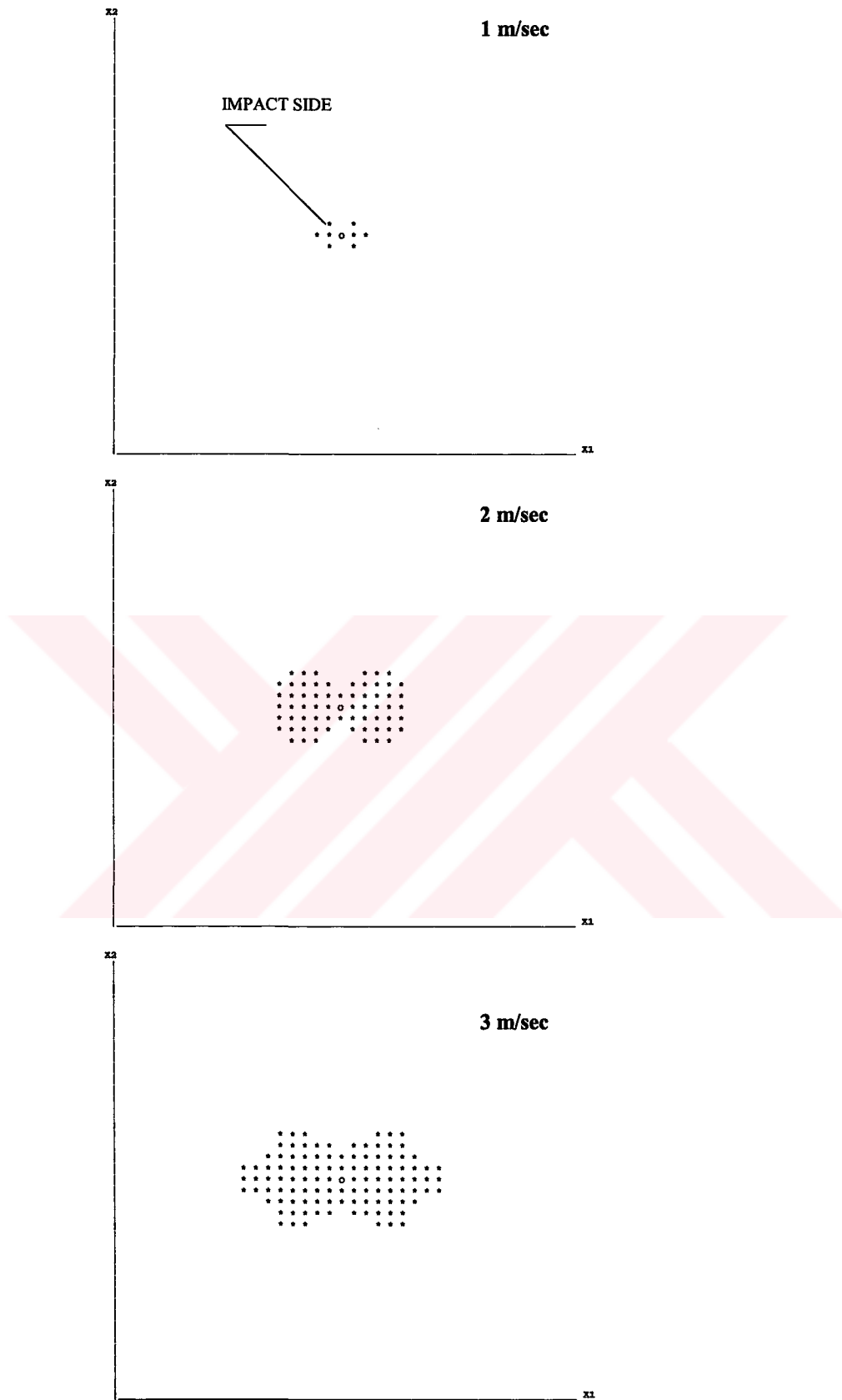
Figure 6.32 Predicted major delaminations at three different impact velocity levels ($(0^0/90^0/0^0/90^0)_s$, 150 mm by 150 mm and 2600 g).

Figure 6.33 Comparison of force histories at three different impact velocity levels $((0^0/-45^0/45^0)_s$, 150 mm by 150 mm and 2600 g) **(a)** experimental response **(b)** predicted response.

Figure 6.34 Comparison of center deflection histories at three different impact velocity levels $((0^0/-45^0/45^0)_s$, 150 mm by 150 mm and 2600 g).

Figure 6.35 History of the stresses σ_1, σ_2 and τ_{12} at a given point (1, 1, 2.2 mm) calculated by 3DIMPACT at three different impact velocity levels $((0^0/-45^0/45^0)_s$, 150 mm by 150 mm and 2600 g).
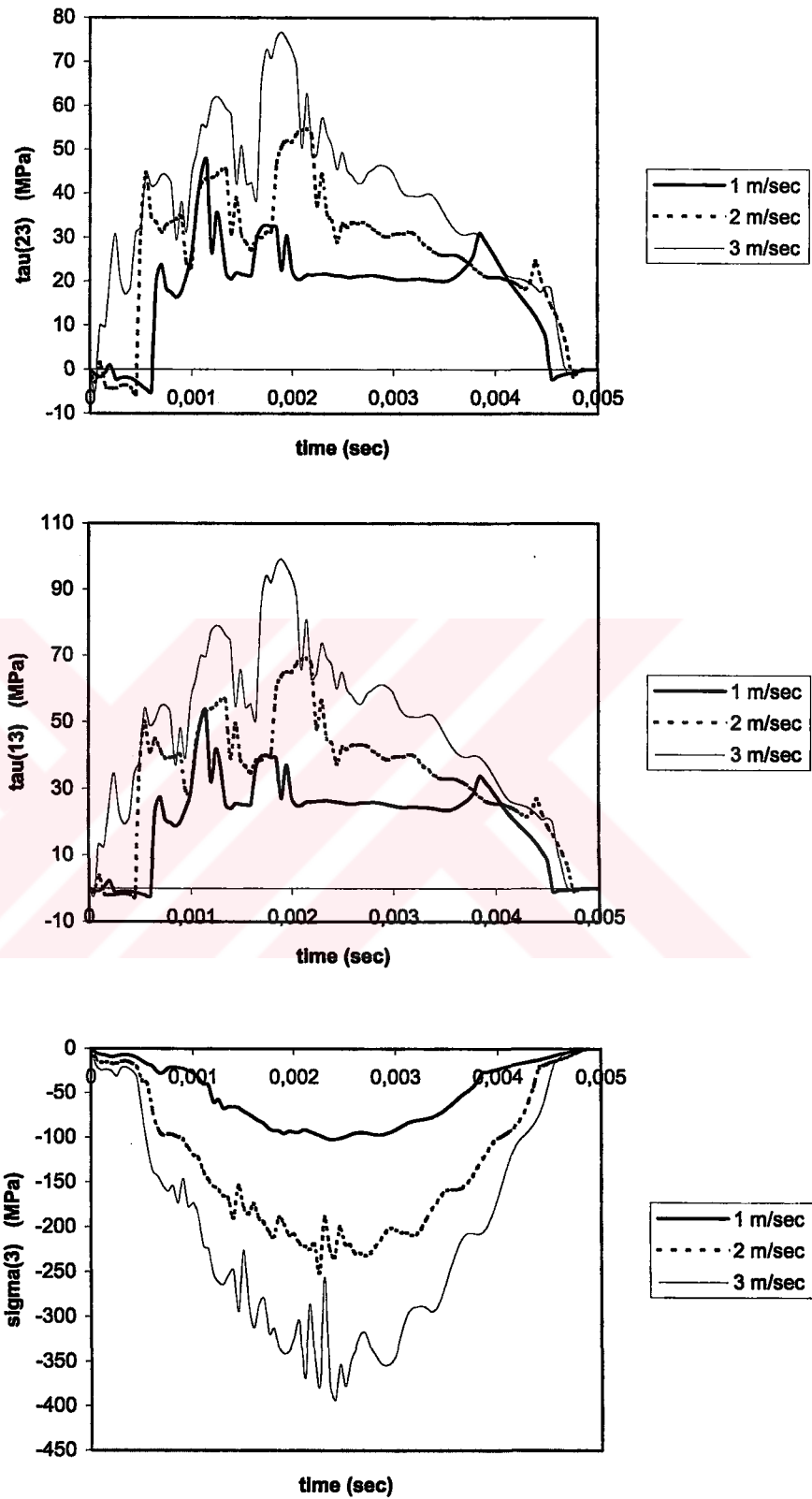
Figure 6.36 History of the stresses τ_{23}, τ_{13} and σ_3 at a given point (1, 1, 2.2 mm) calculated by 3DIMPACT at three different impact velocity levels $((0^0/-45^0/45^0)_s$, 150 mm by 150 mm and 2600 g).
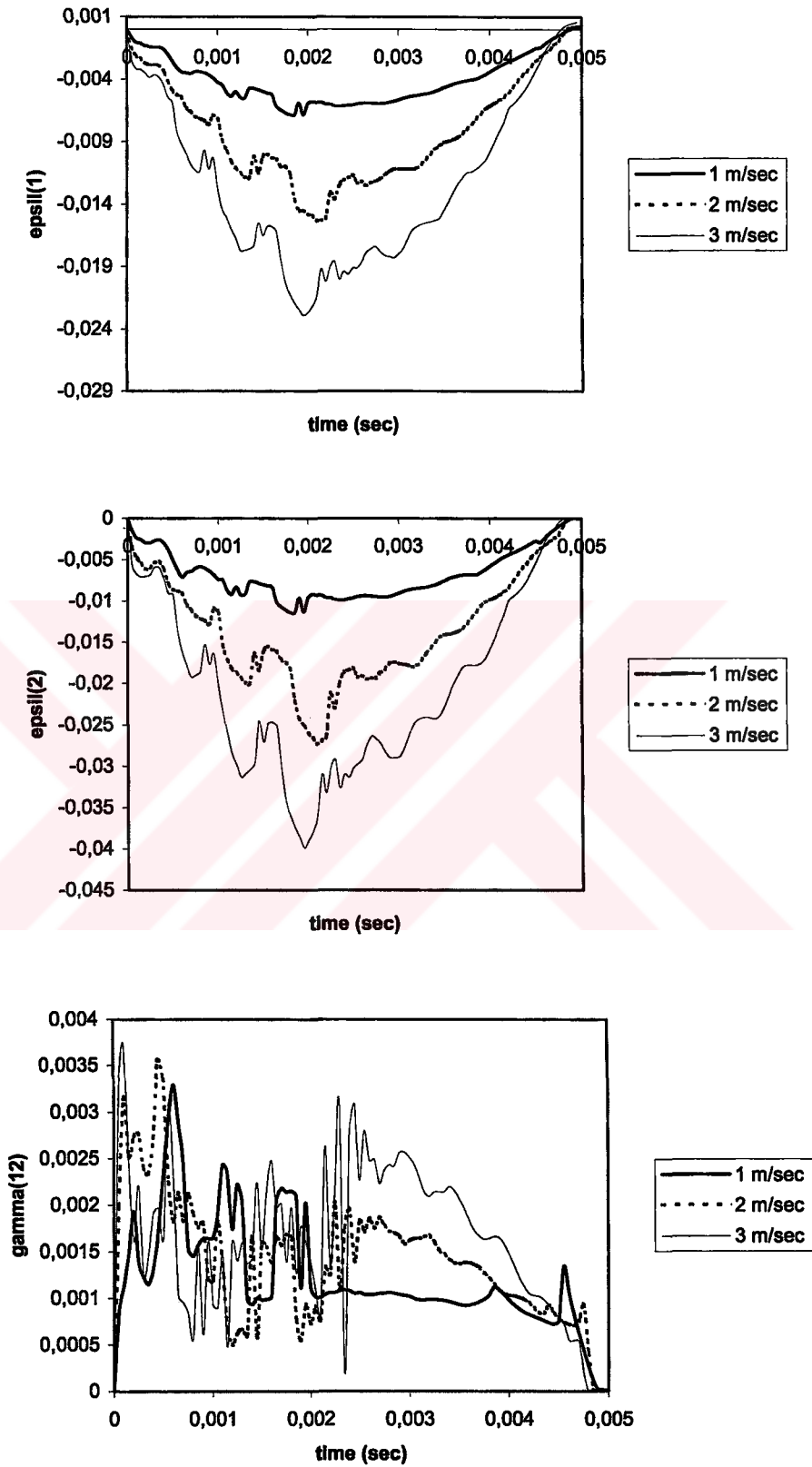
Figure 6.37 History of the strains ε_1, ε_2 and γ_{12} at a given point (1, 1, 2.2 mm) calculated by 3DIMPACT at three different impact velocity levels $((0^0/-45^0/45^0)_s$, 150 mm by 150 mm and 2600 g).
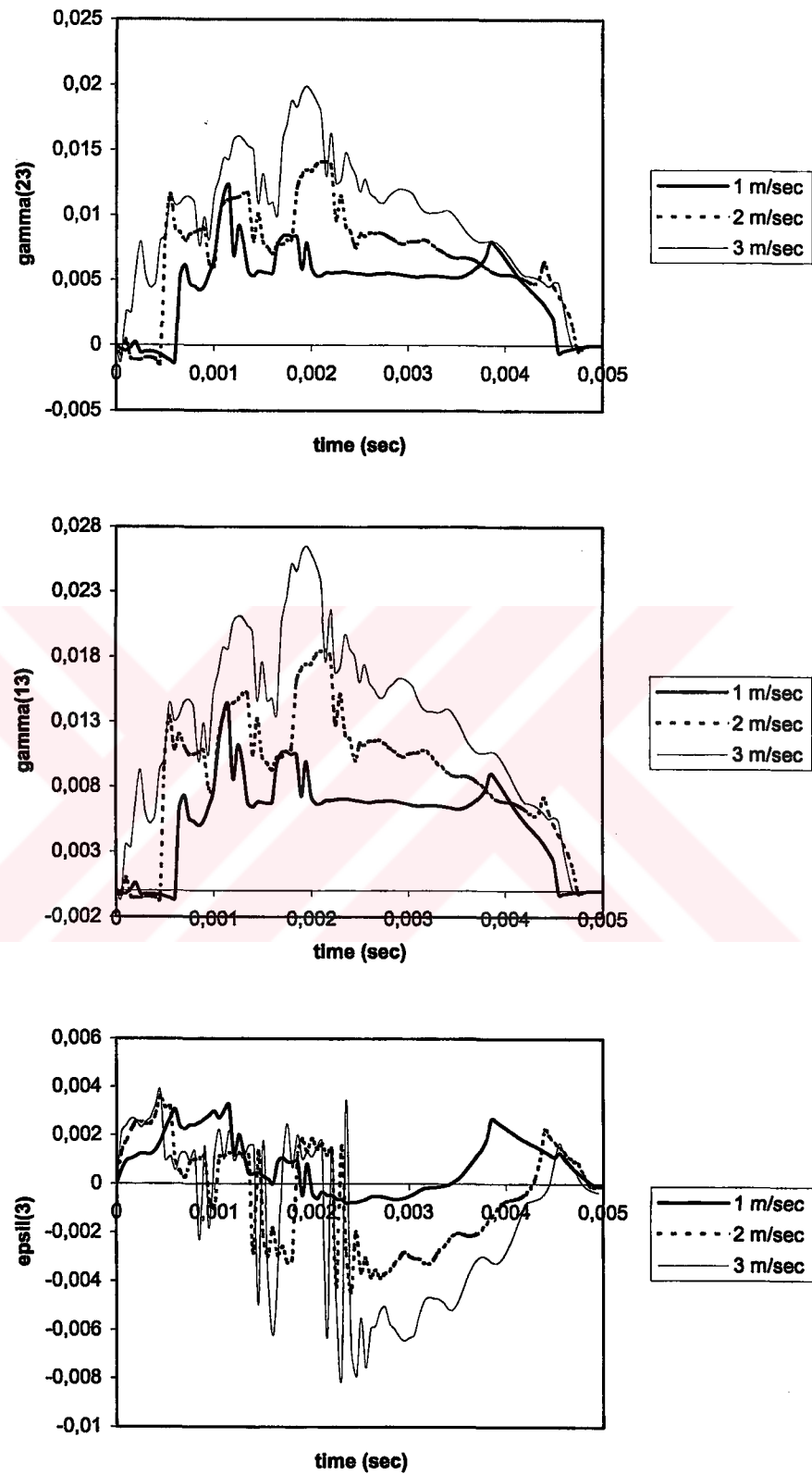
Figure 6.38 History of the strains γ_{23}, γ_{13} and ε_3 at a given point (1, 1, 2.2 mm) calculated by 3DIMPACT at three different impact velocity levels $((0^0/-45^0/45^0)_s$, 150 mm by 150 mm and 2600 g).
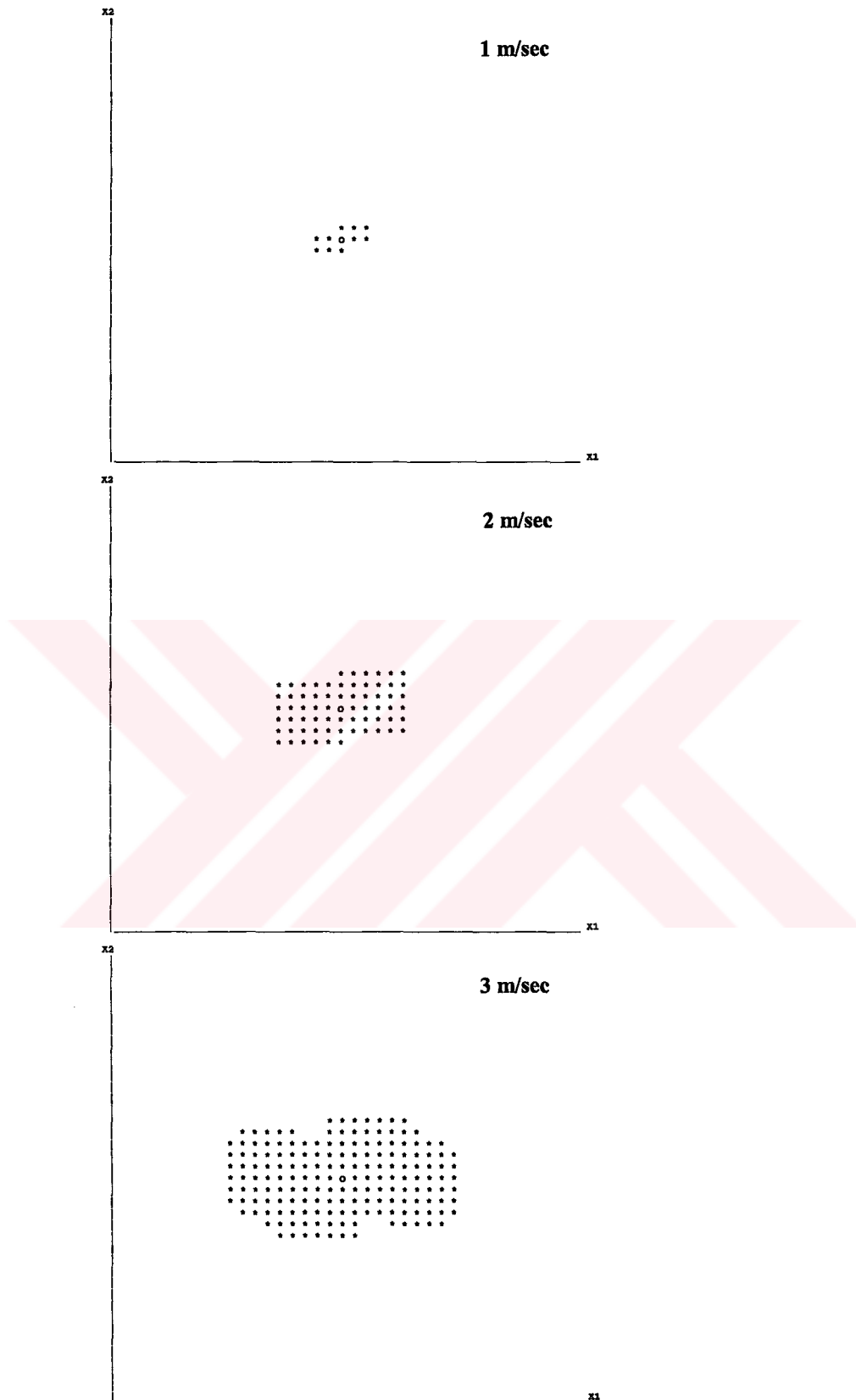
Figure 6.39 Predicted major delaminations at three different impact velocity levels $((0^0/-45^0/45^0)_s$, 150 mm by 150 mm and 2600 g).

6.5 Impactor Mass Effects

Impact tests are performed at increasing masses (135 g and 2600 g) on clamped plates $(0^0/90^0/0^0/90^0)_s$ in order to determine the effect of the projectile mass on the impact behavior of the composite laminate. Figure 6.40 shows experimental and numerical comparison of force-time histories at two different impactor mass levels. With a constant velocity of 3 m/sec, the mass is varied for two cases: (a) 135 g and (b) 2600 g. The measured maximum contact forces are 1481 N and 5825 N for the above impactor masses, respectively. It is shown that the heavier impactor mass would increase the impact force as well as the contact duration. Effect of impactor mass on center deflection histories of a laminated composite plate is given in Figure 6.41.

The in-plane stresses σ_1, σ_2 and τ_{12} at (1, 1, 2.4 mm), which are the mid-point of the composite plate and on the upper surface of the laminations, are presented in Figure 6.42. The transverse shear stresses τ_{23}, τ_{13} and σ_3 are checked at the same point. The time histories are plotted in Figure 6.43. The in-plane strains ε_1, ε_2 and γ_{12} are presented in Figure 6.44. The transverse shear strains γ_{23}, γ_{13} and ε_3 are calculated at the same point. The time histories are given in Figure 6.45.

The numerical simulations of the delamination shape and size at the interface containing the major delamination of the laminates are shown in Figure 6.46. No delamination is predicted for impactor mass of 135 g. However, the delamination damage for impactor mass of 2600 g is very big and propagates along the fiber direction at the lower layer.

Figure 6.47 shows experimental and numerical comparison of force-time histories of 6-ply laminates with $(0^0,-45^0,45^0)_s$ for two different impactor mass levels, 135 g and 2600g and an impact velocity of 3 m/sec. Effect of impactor mass on center deflection histories, stresses and strains and delaminated area is given in Figures 6.48-6.53 for 6-ply laminates with $(0^0,-45^0,45^0)_s$.
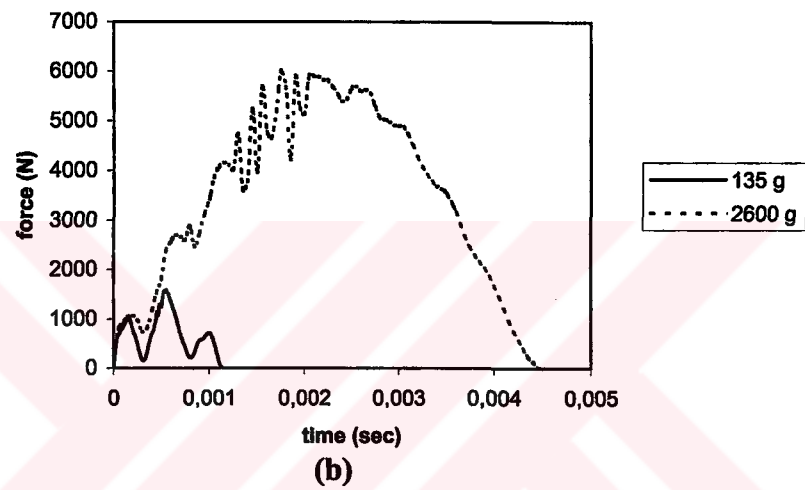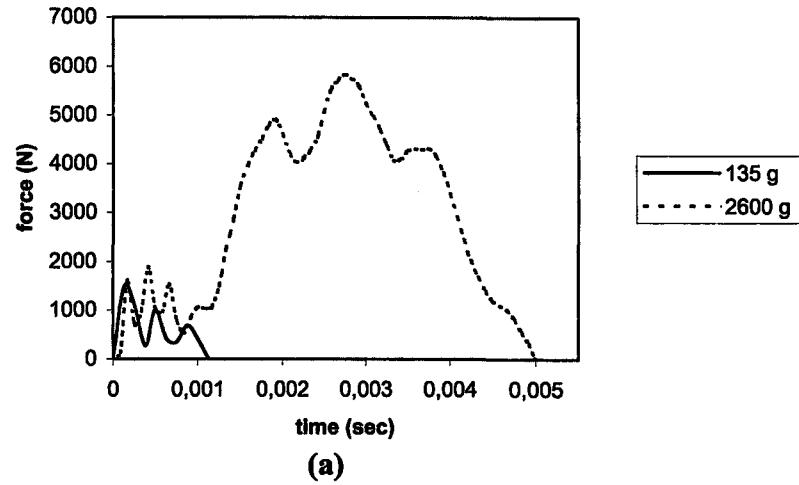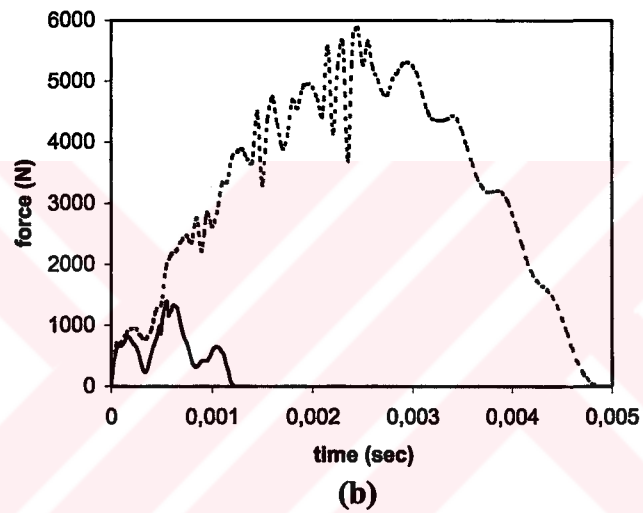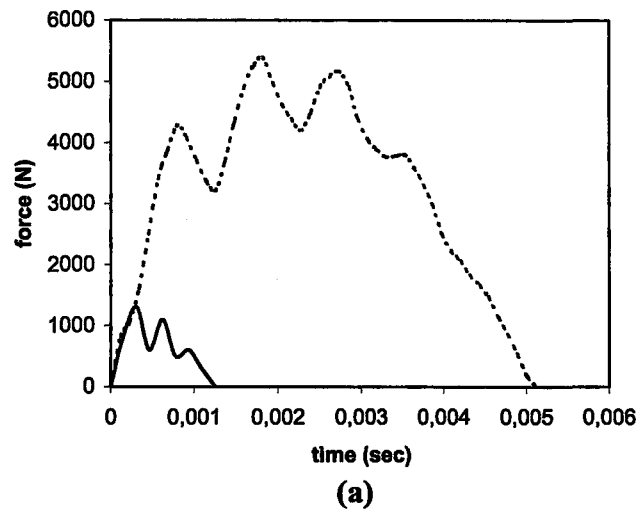
Figure 6.40 Comparison of force histories at two different impactor mass levels ((0°/90°/0°/90°)$_s$, 150 mm by 150 mm and 3 m/sec) **(a)** experimental response **(b)** predicted response.
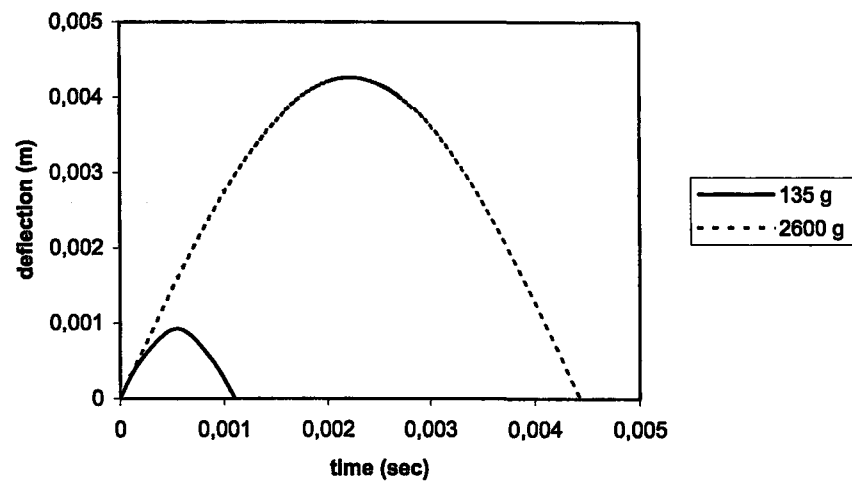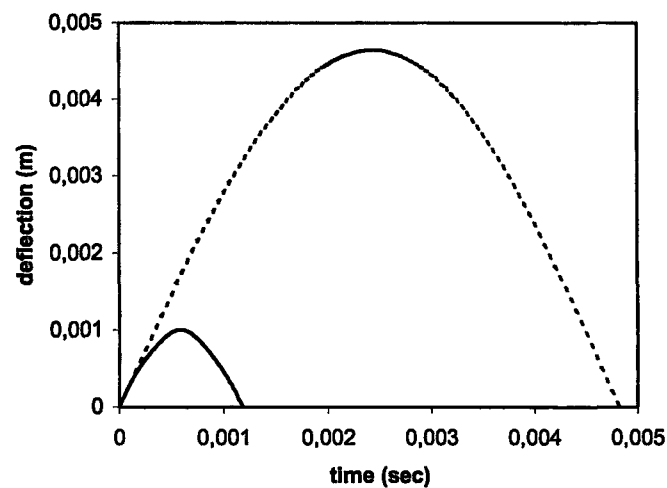

Figure 6.41 Comparison of center deflection histories at two different impactor mass levels ((0°/90°/0°/90°)$_s$, 150 mm by 150 mm and 3 m/sec).
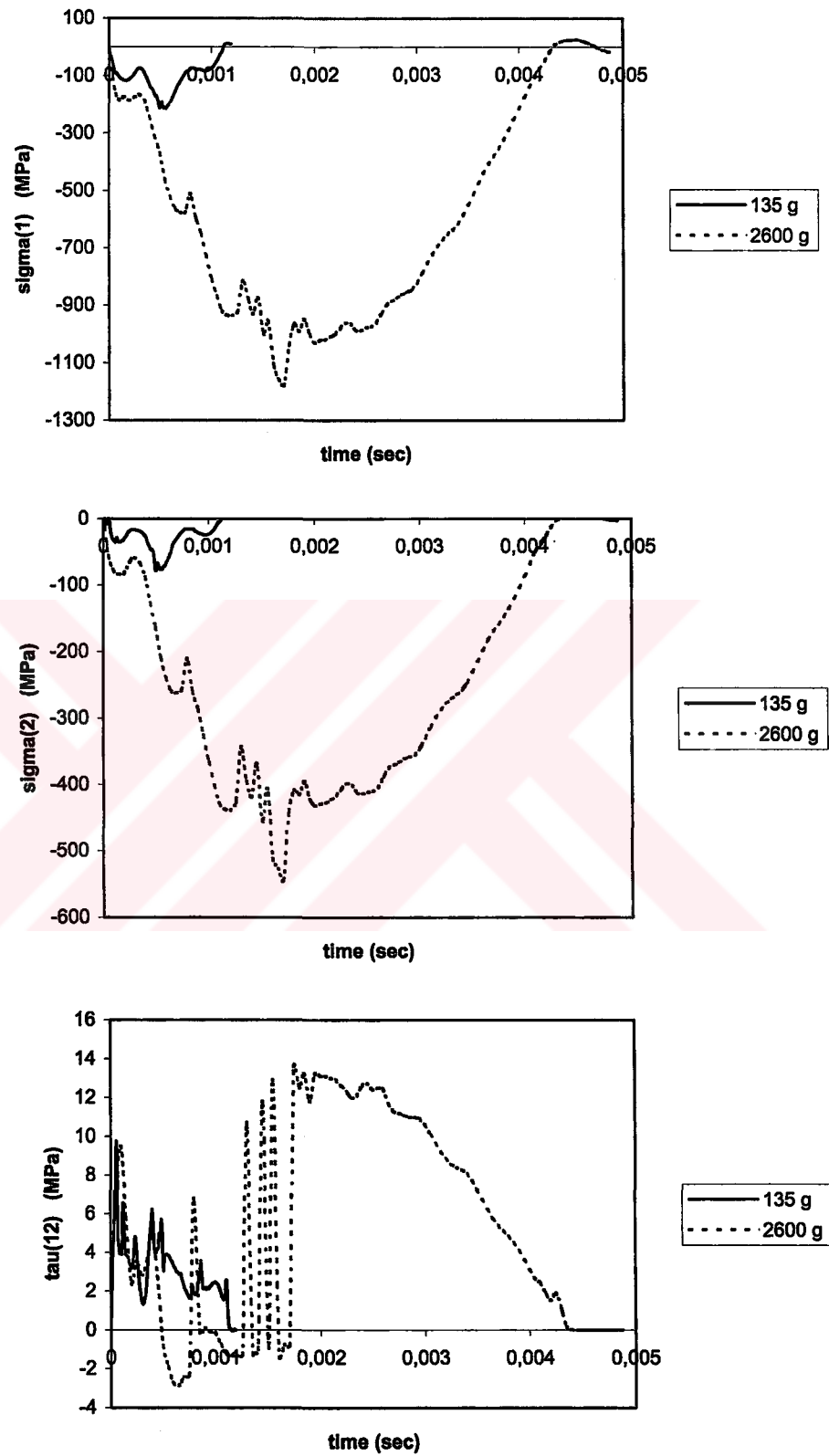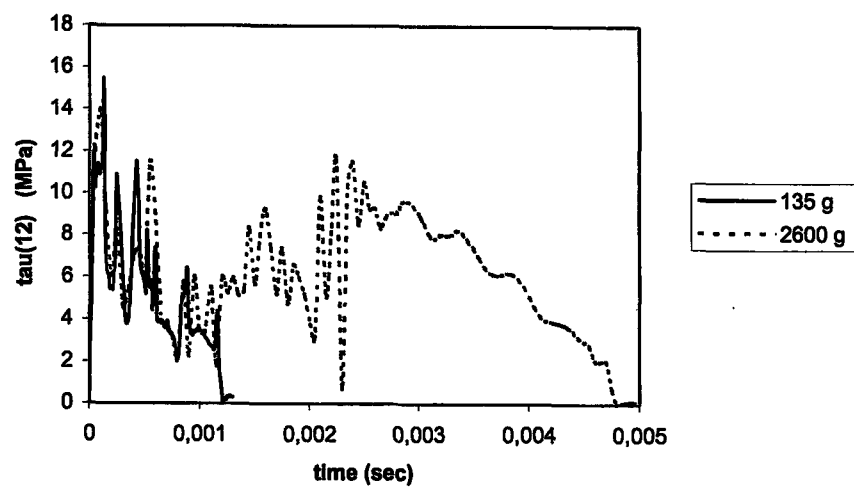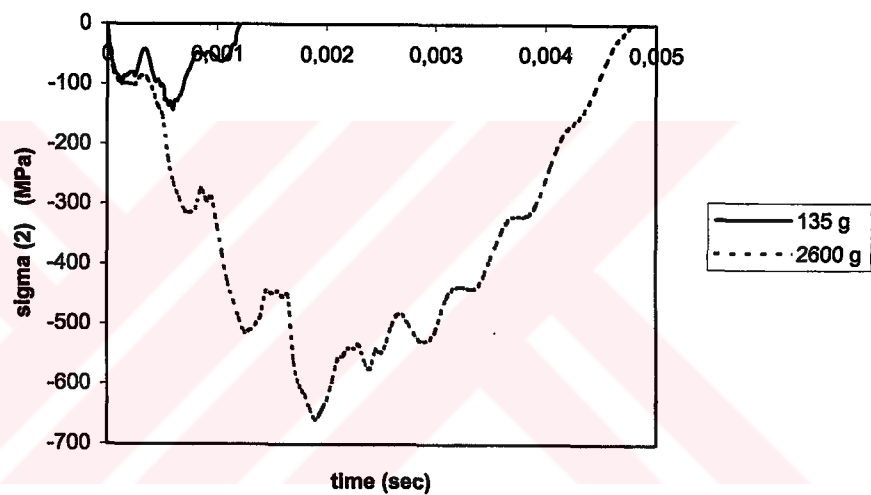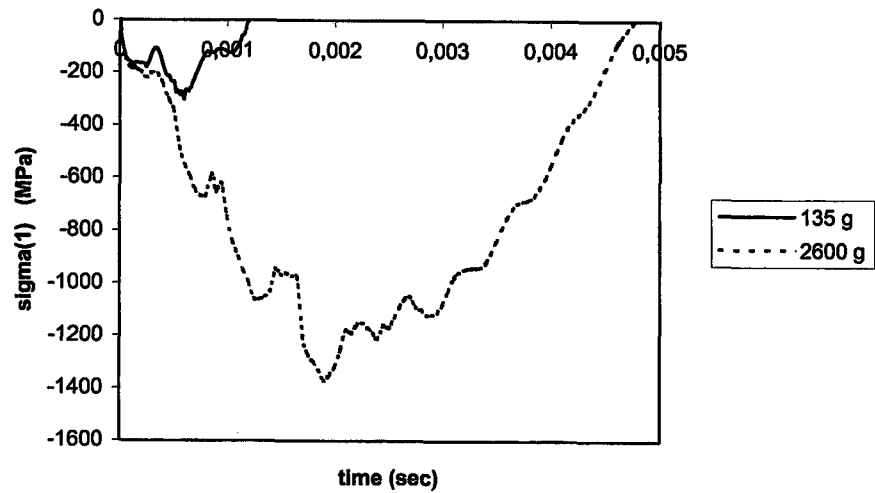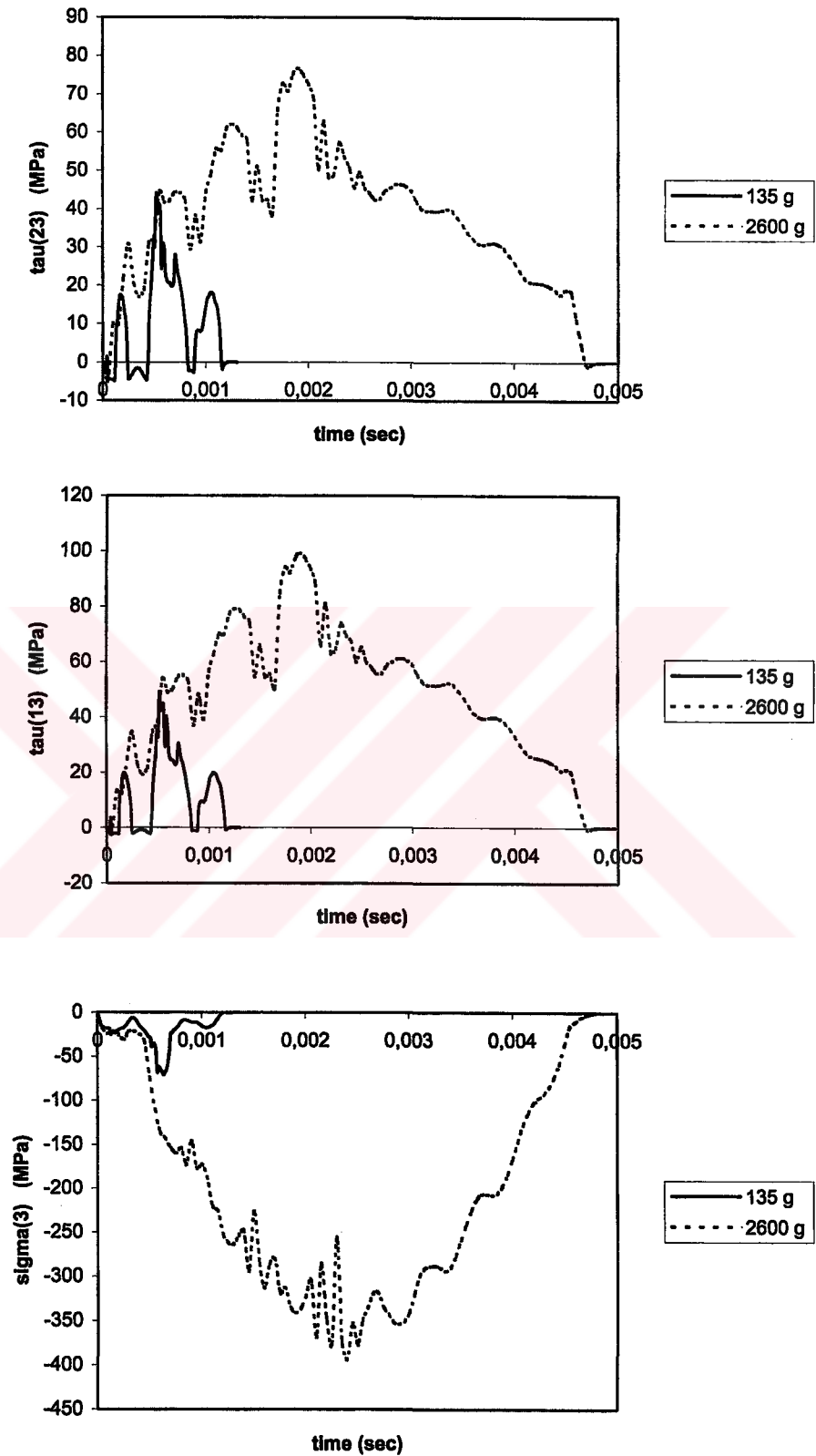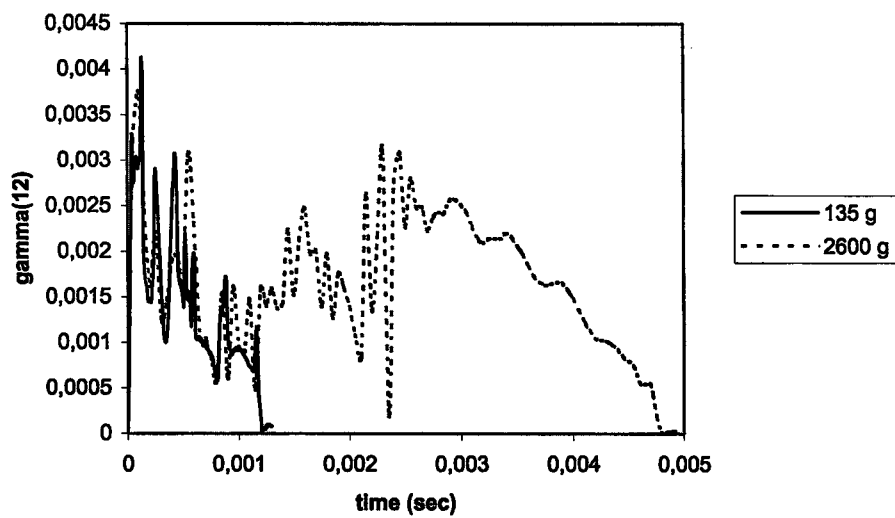
Figure 6.42 History of the stresses σ_1, σ_2 and τ_{12} at a given point (1, 1, 2.4 mm) calculated by 3DIMPACT at two different impactor mass levels $((0^0/90^0/0^0/90^0)_s$, 150 mm by 150 mm and 3 m/sec).
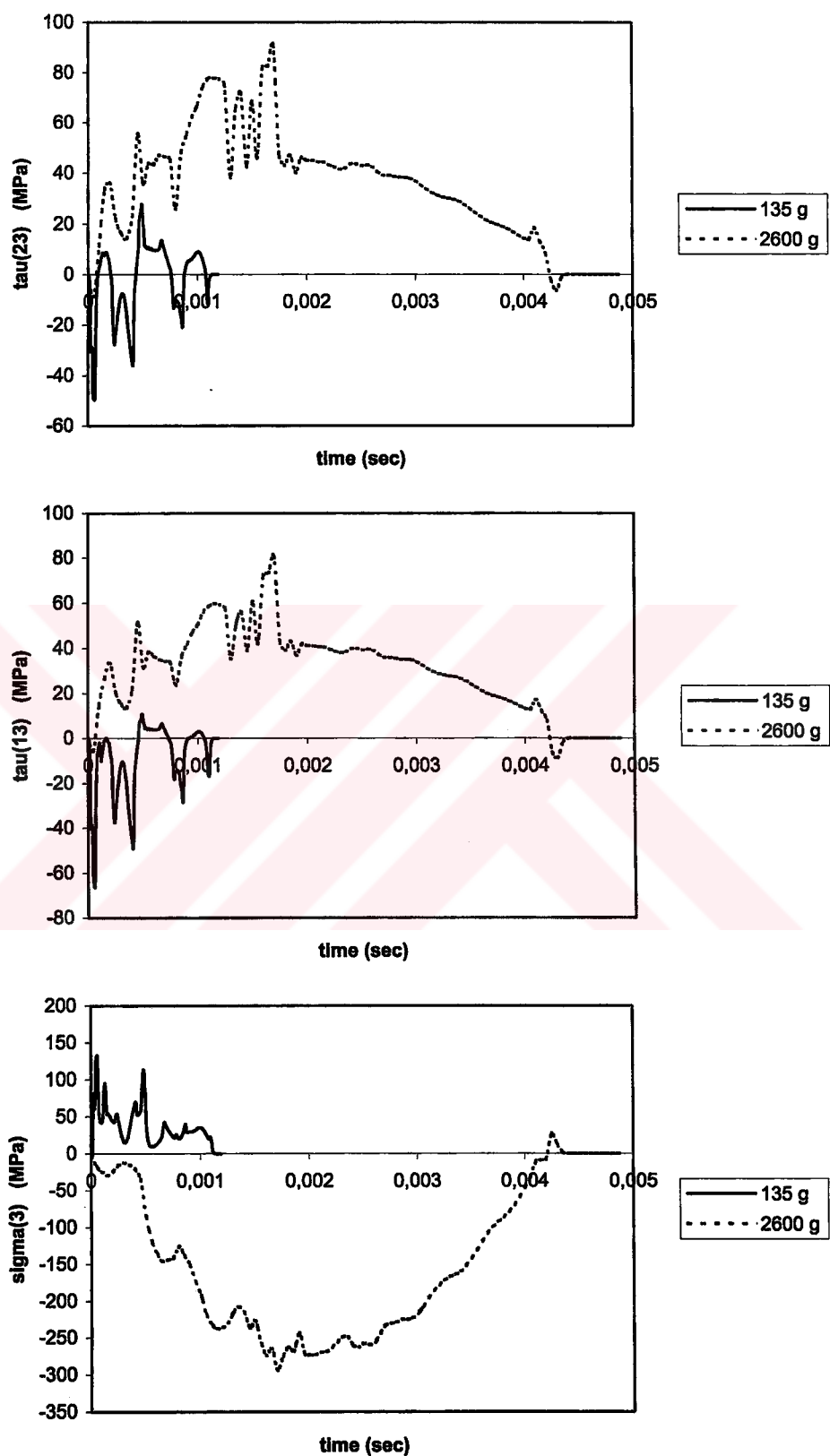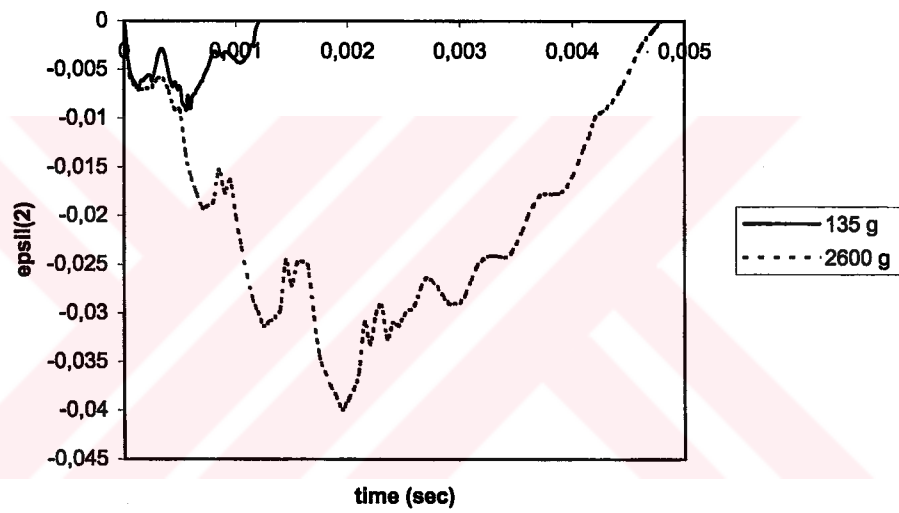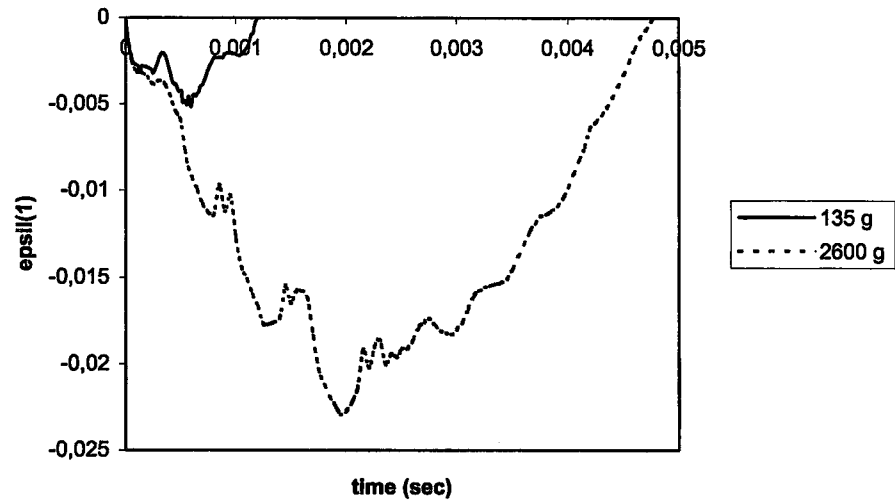
Figure 6.43 History of the stresses τ_{23}, τ_{13} and σ_3 at a given point (1, 1, 2.4 mm) calculated by 3DIMPACT at two different impactor mass levels $((0^0/90^0/0^0/90^0)_s$, 150 mm by 150 mm and 3 m/sec).
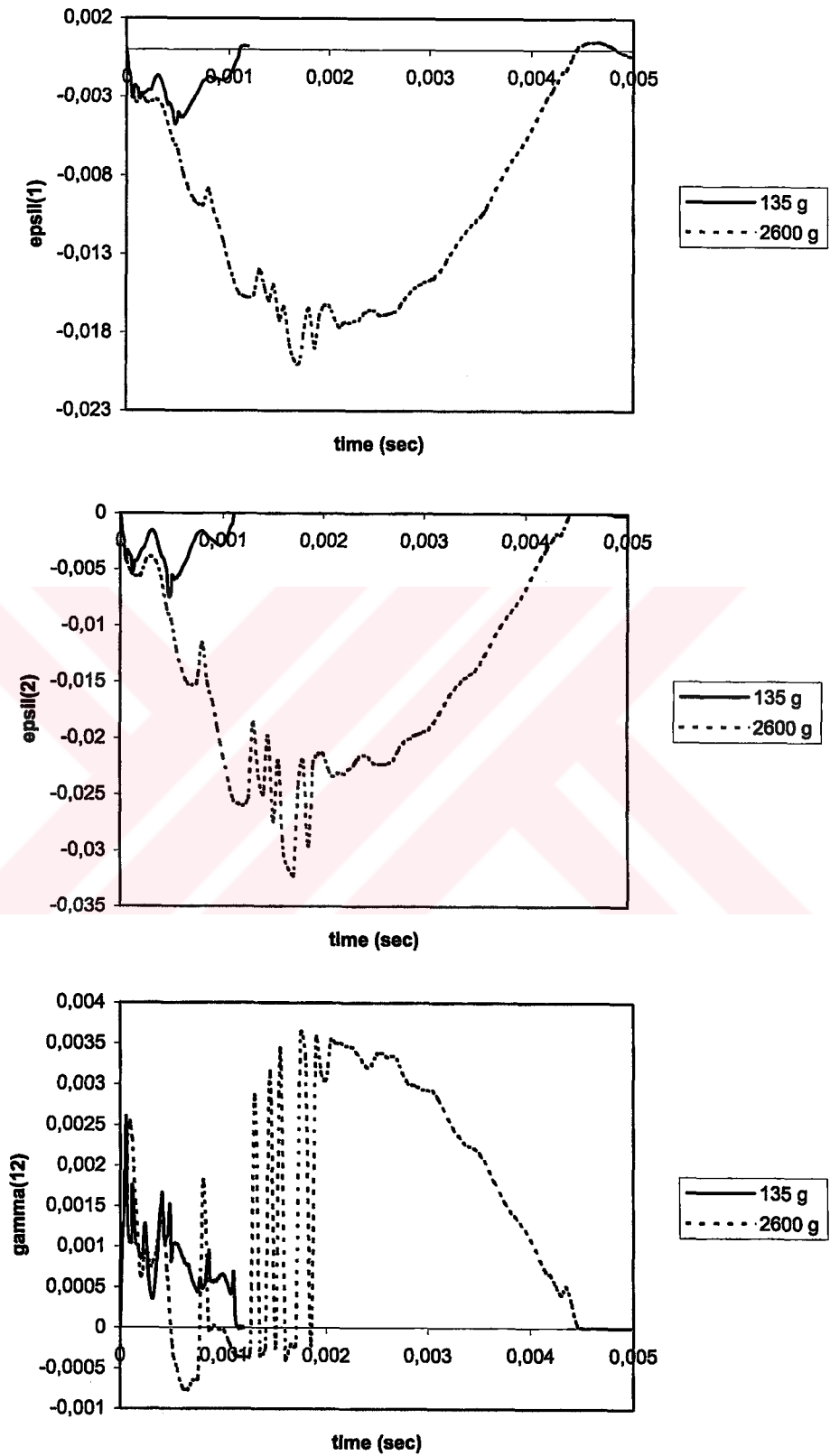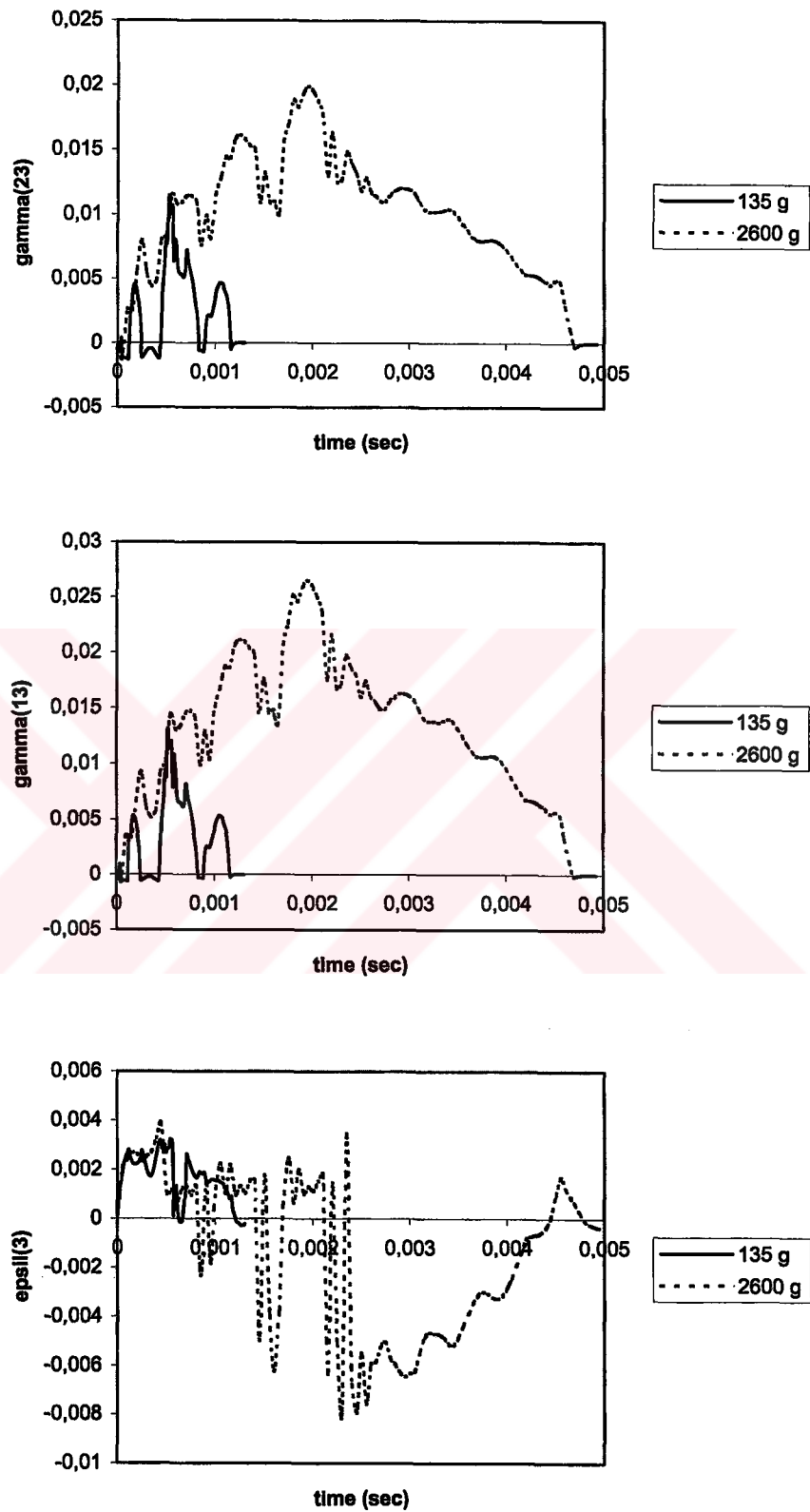
Figure 6.44 History of the strains ε_1, ε_2 and γ_{12} at a given point (1, 1, 2.4 mm) calculated by 3DIMPACT at two different impactor mass levels $((0^0/90^0/0^0/90^0)_s$, 150 mm by 150 mm and 3 m/sec).
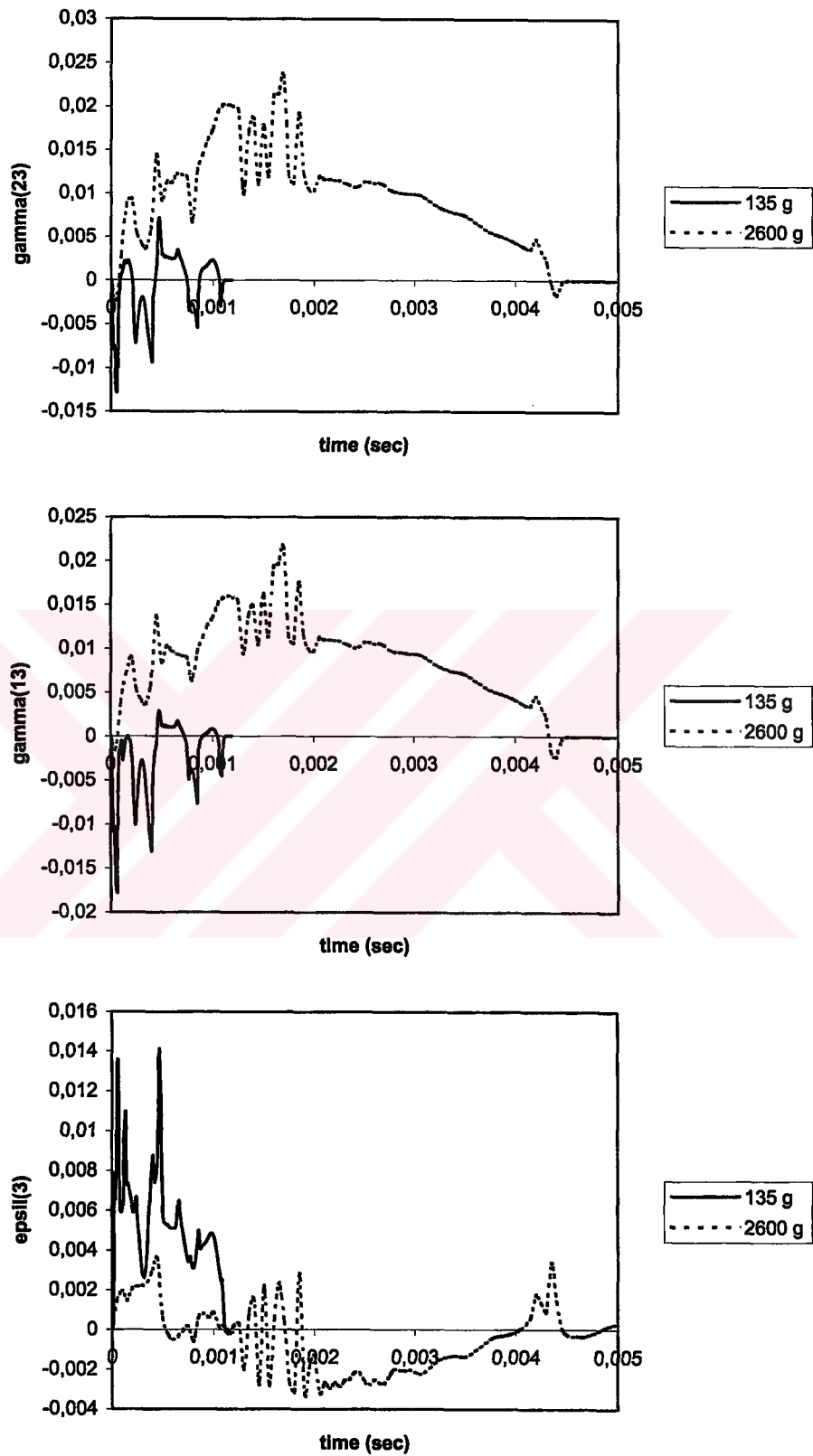
Figure 6.45 History of the strains γ_{23}, γ_{13} and ε_3 at a given point (1, 1, 2.4 mm) calculated by 3DIMPACT at two different impactor mass levels ($(0^0/90^0/0^0/90^0)_s$, 150 mm by 150 mm and 3 m/sec).

135 g

NO DELAMINATION

2600 g
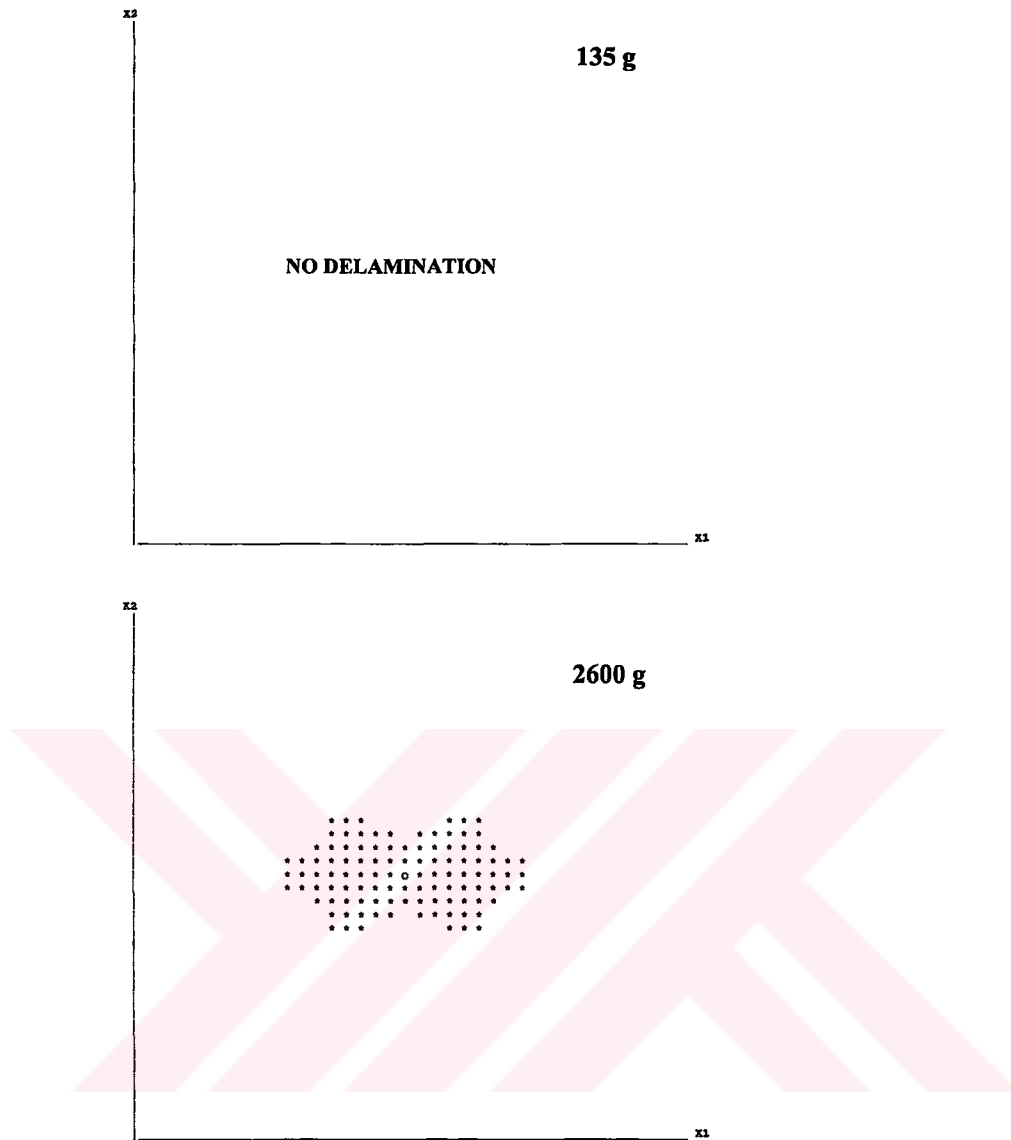
Figure 6.46 Predicted major delaminations at two different impactor mass levels $((0^0/90^0/0^0/90^0)_s$, 150 mm by 150 mm and 3 m/sec).

Figure 6.47 Comparison of force histories at two different impactor mass levels $((0^0/-45^0/45^0)_s$, 150 mm by 150 mm and 3 m/sec) **(a)** experimental response **(b)** predicted response.

Figure 6.48 Comparison of center deflection histories at two different impactor mass levels $((0^0/-45^0/45^0)_s$, 150 mm by 150 mm and 3 m/sec).

Figure 6.49 History of the stresses σ_1, σ_2 and τ_{12} at a given point (1, 1, 2.2 mm) calculated by 3DIMPACT at two different impactor mass levels $((0^0/-45^0/45^0)_s$, 150 mm by 150 mm and 3 m/sec).

Figure 6.50 History of the stresses τ_{23}, τ_{13} and σ_3 at a given point (1, 1, 2.2 mm) calculated by 3DIMPACT at two different impactor mass levels $((0^0/-45^0/45^0)_s$, 150 mm by 150 mm and 3 m/sec).

Figure 6.51 History of the strains ε_1, ε_2 and γ_{12} at a given point (1, 1, 2.2 mm) calculated by 3DIMPACT at two different impactor mass levels ((0^0/-45^0/45^0)$_s$, 150 mm by 150 mm and 3 m/sec).

Figure 6.52 History of the strains γ_{23}, γ_{13} and ε_3 at a given point (1, 1, 2.2 mm) calculated by 3DIMPACT at two different impactor mass levels $((0^0/-45^0/45^0)_s$, 150 mm by 150 mm and 3 m/sec).
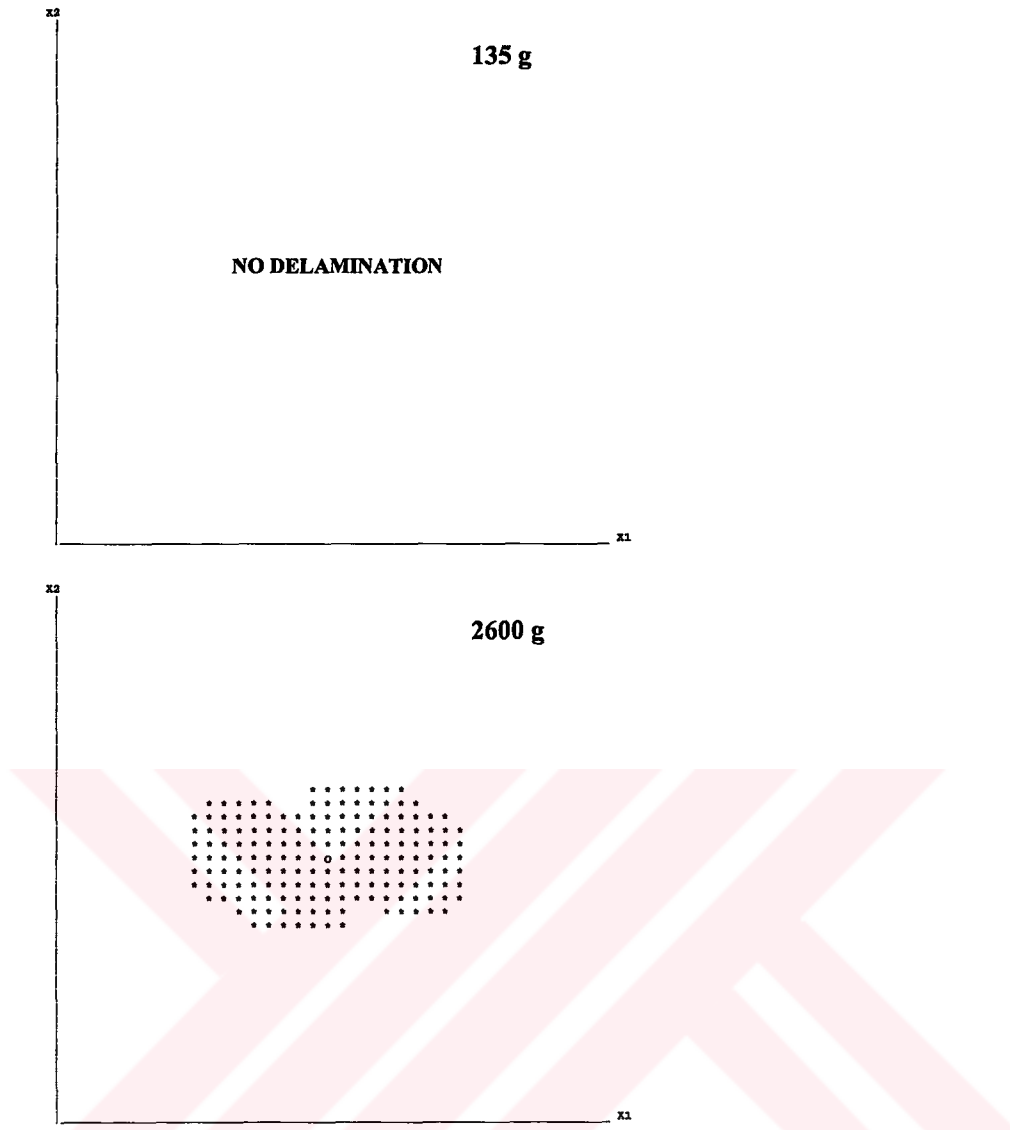
Figure 6.53 Predicted major delaminations at two different impactor mass levels $((0^{0}/-45^{0}/45^{0})_{s}$, 150 mm by 150 mm and 3 m/sec).

As can be seen, the magnitude of impact forces, deflections, stresses and strains, and delaminated area are directly proportional to the impactor mass. The shape of the force history changes noticeably as the mass varies. The magnitude of impact force increases as the mass increases. Similarly the duration of contact increases as the mass increases.

6.6 In-Plane Dimensional Effects

The effect of in-plane dimensions on the contact force for 8-ply laminates with $(0^0/90^0/0^0/90^0)_s$ is shown experimentally and numerically in Figure 6.54. In addition to effective impact zones of 150 mm by 150 mm, other effective impact zones of 150 mm by 100 mm and 150 mm by 50 mm, i.e. intermediate and small rectangular specimens, are investigated for in-plane dimensional effects. It can be concluded that the smaller the width of the rectangular composite laminate, the higher the contact duration and the impact response is dependent on laminate geometries. The highest impact force is obtained for intermediate rectangular specimens (150 mm by 100 mm) and the lower impact force is obtained for small rectangular specimens (150 mm by 50 mm). The differences between peak forces for the three effective impact zones are not as significant as that for thickness difference.

Effect of in-plane dimensions on center deflection histories of a laminated composite plate is given in Figure 6.55. The transient stresses and strains are presented in Figures 6.56-6.59, respectively. The numerical simulations of the delamination shape and size at the interface containing the major delamination of the laminates are shown in Figure 6.60. The observed delamination propagates along the fiber direction.

Figure 6.61 shows experimental and numerical comparison of force-time histories of 6-ply woven reinforced laminates with 2.8 mm thickness for three different in-plane dimensions. Effect of in-plane dimensions on center deflection histories, stresses and strains and delaminated area is given in Figures 6.62-6.67 for 6-ply woven reinforced laminates with 2.8 mm thickness.

For woven reinforced laminates, the result that rectangular specimens with larger widths have higher peak forces coincides with the fact that the larger the width of the laminate dimensions the stiffer the composite laminate. Similar results are also found for the woven laminates with 1.4 mm thicknesses.
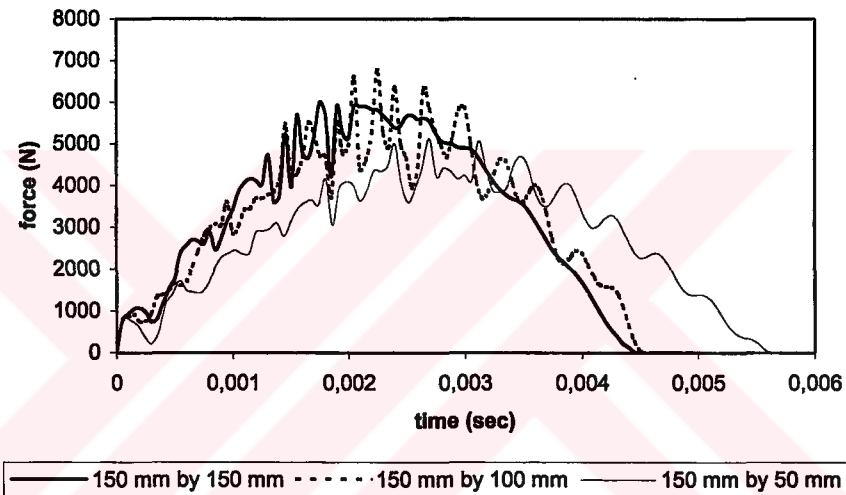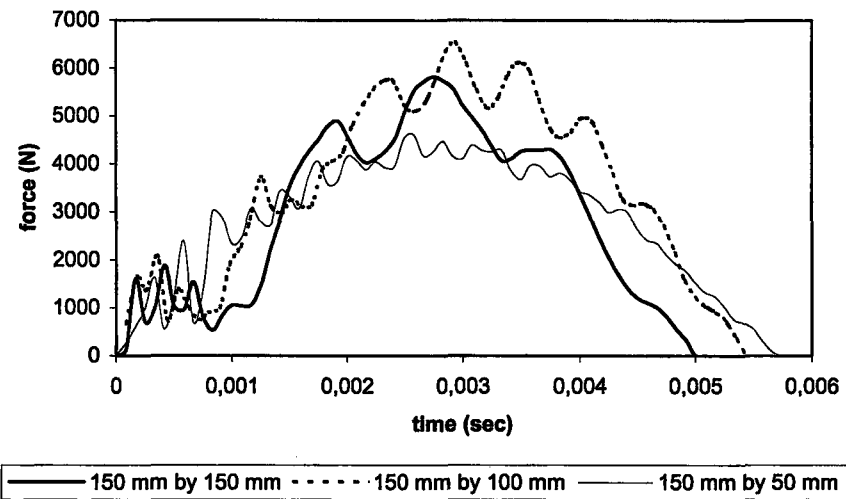
Figure 6.54 Comparison of force histories at three different in-plane dimensions $((0^0/90^0/0^0/90^0)_s$, 2600 g and 3 m/sec) **(a)** experimental response **(b)** predicted response.
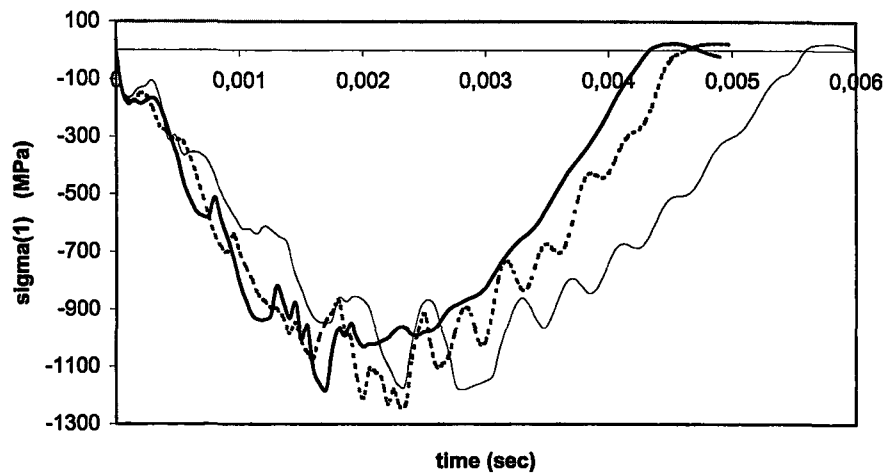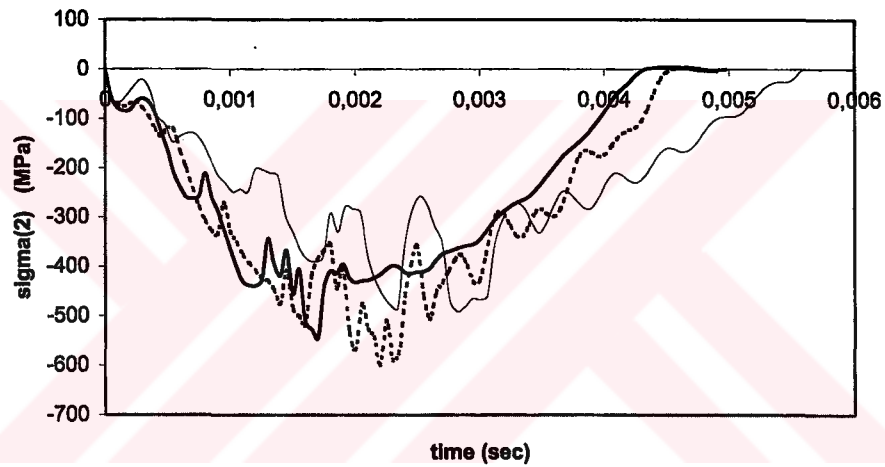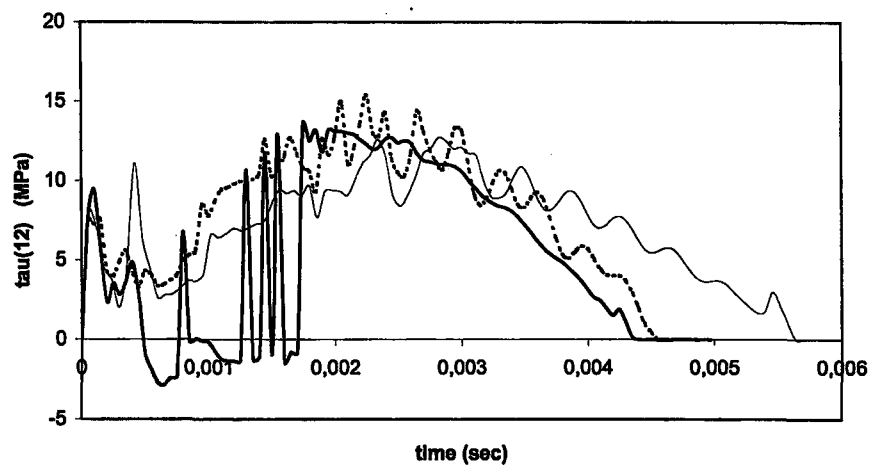

Figure 6.55 Comparison of center deflection histories at three different in-plane dimensions $((0^0/90^0/0^0/90^0)_s$, 2600 g and 3 m/sec).

Figure 6.56 History of the stresses σ_1, σ_2 and τ_{12} at a given point (1, 1, 2.4 mm) calculated by 3DIMPACT at three different in-plane dimensions ($(0^0/90^0/0^0/90^0)_s$, 2600 g and 3 m/sec).

Figure 6.57 History of the stresses τ_{23}, τ_{13} and σ_3 at a given point (1, 1, 2.4 mm) calculated by 3DIMPACT at three different in-plane dimensions $((0^0/90^0/0^0/90^0)_s$, 2600 g and 3 m/sec).

Figure 6.58 History of the strains ε_1, ε_2 and γ_{12} at a given point (1, 1, 2.4 mm) calculated by 3DIMPACT at three different in-plane dimensions ($(0^0/90^0/0^0/90^0)_s$, 2600 g and 3 m/sec).
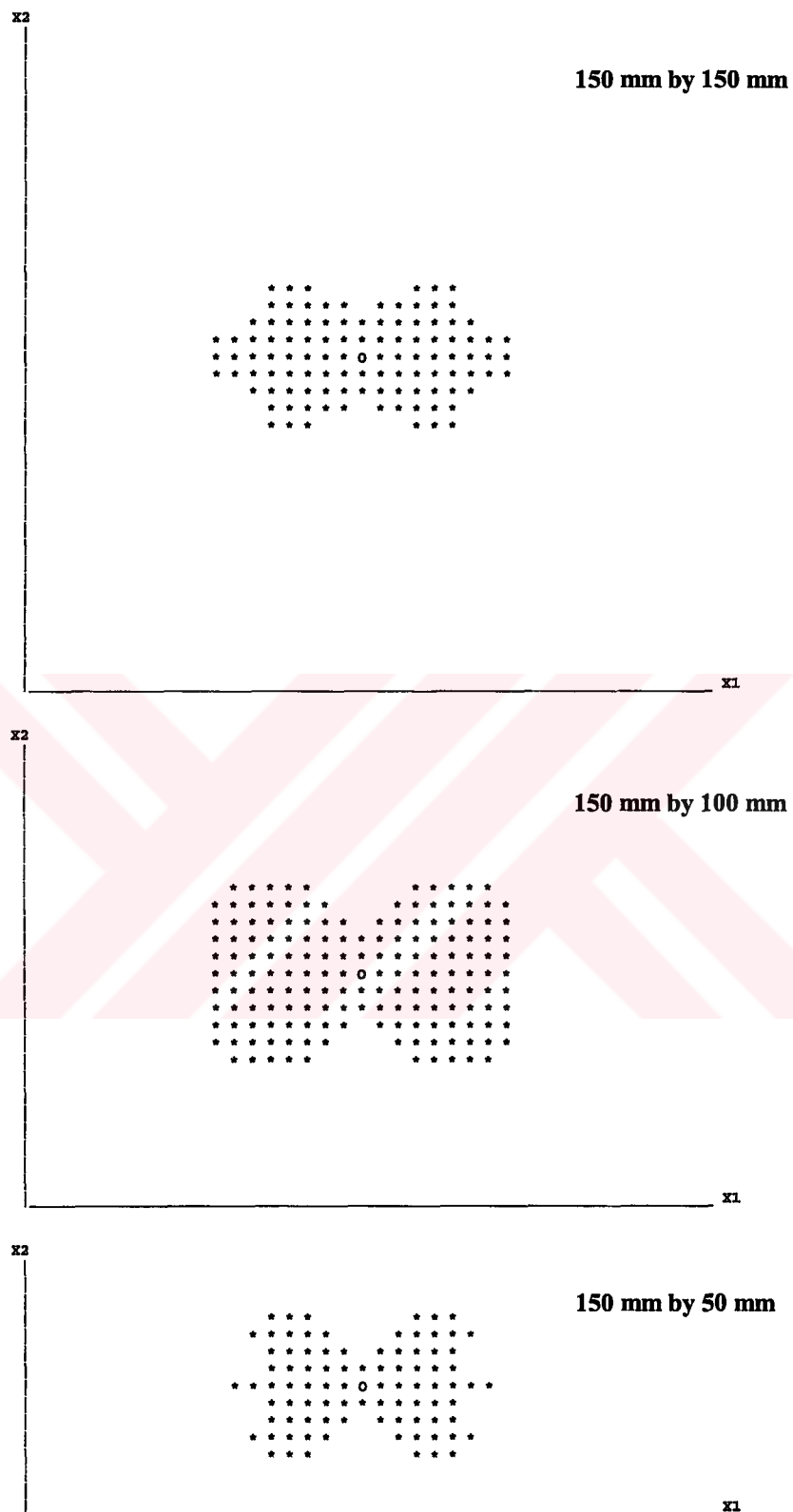
Figure 6.59 History of the strains γ_{23}, γ_{13} and ε_3 at a given point (1, 1, 2.4 mm) calculated by 3DIMPACT at three different in-plane dimensions $((0^0/90^0/0^0/90^0)_s$, 2600 g and 3 m/sec).
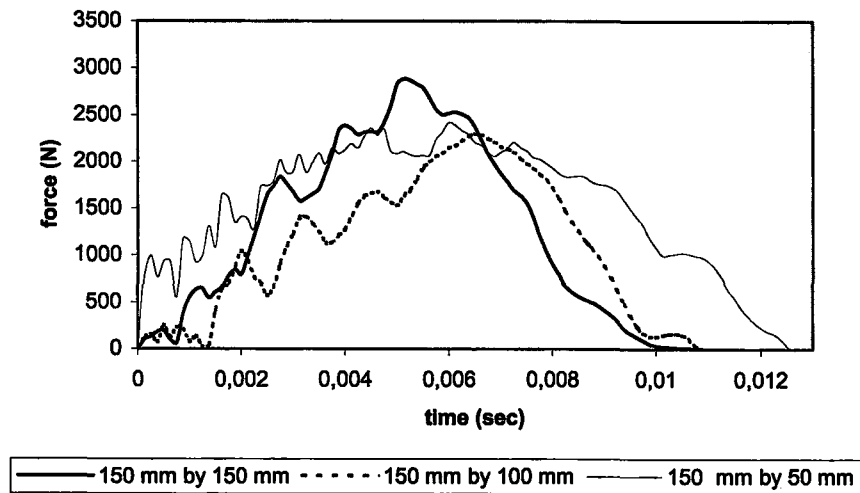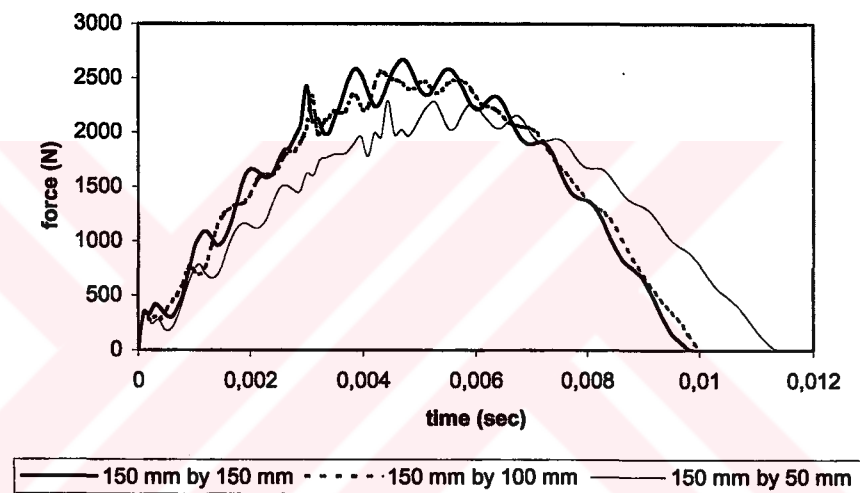
Figure 6.60 Predicted major delaminations at three different in-plane dimensions ($(0^0/90^0/0^0/90^0)_s$, 2600 g and 3 m/sec).

(a)

(b)

Figure 6.61 Comparison of force histories at three different in-plane dimensions $((0^0,90^0)_6,$ 2600 g and 3 m/sec) **(a)** experimental response **(b)** predicted response.
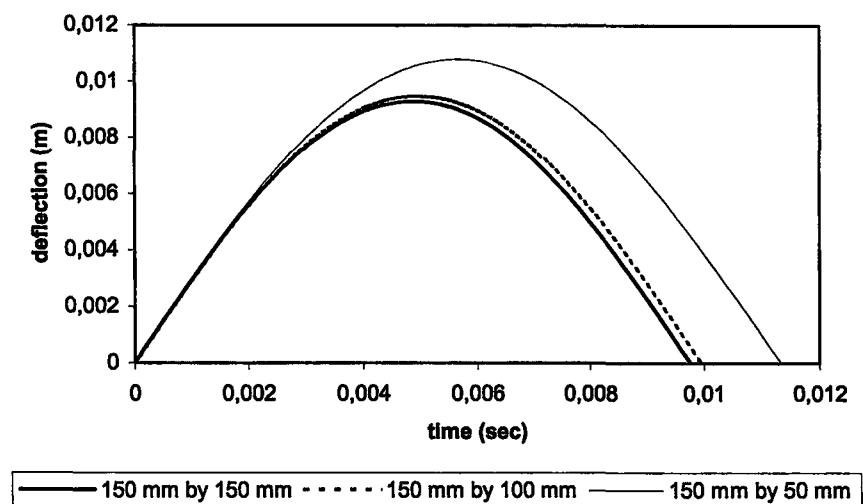

Figure 6.62 Comparison of center deflection histories at three different in-plane dimensions $((0^0,90^0)_6,$ 2600 g and 3 m/sec).
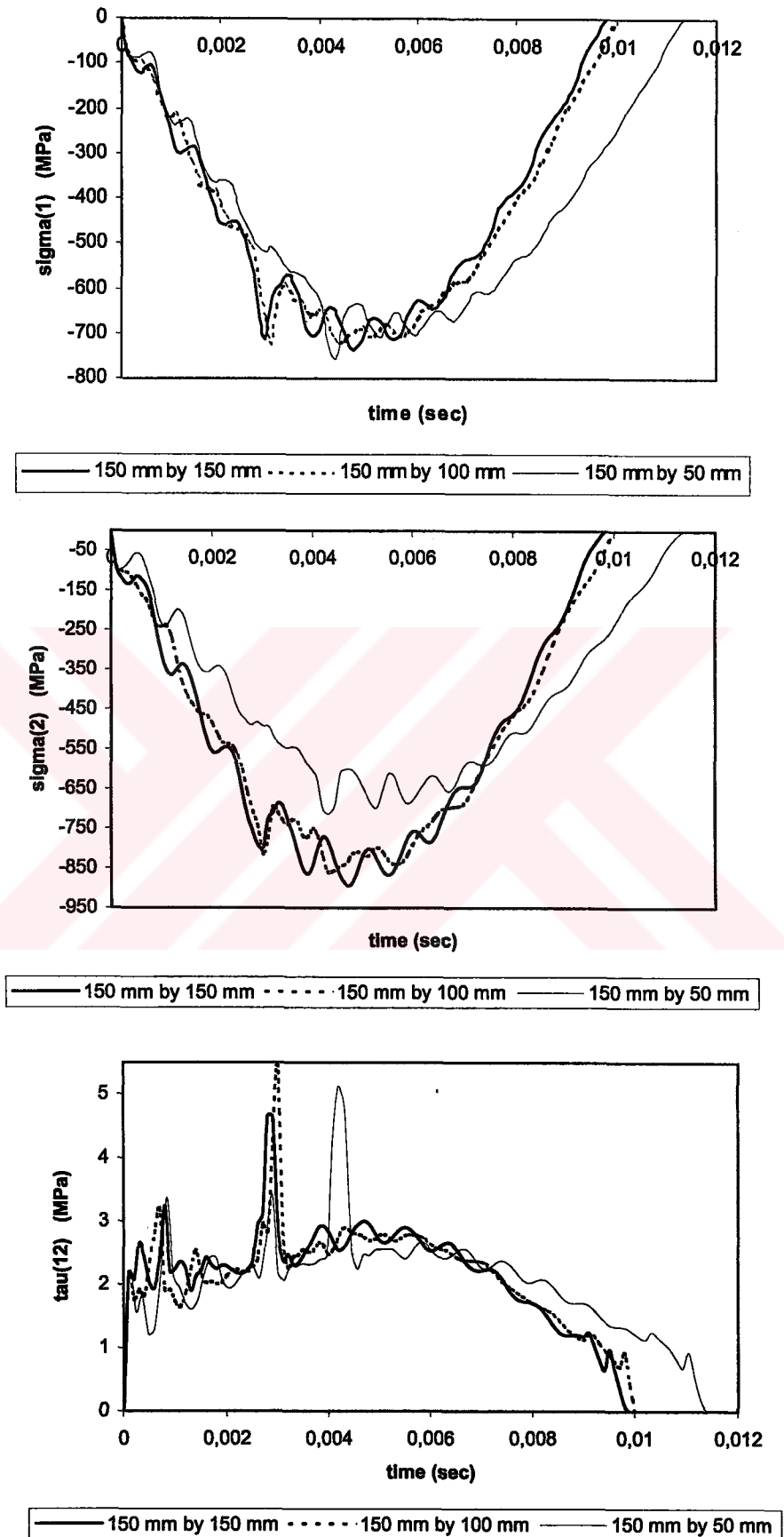
Figure 6.63 History of the stresses σ_1, σ_2 and τ_{12} at a given point (1, 1, 1.4 mm) calculated by 3DIMPACT at three different in-plane dimensions ((0^0,90^0)$_6$, 2600 g and 3 m/sec).

Figure 6.64 History of the stresses τ_{23}, τ_{13} and σ_3 at a given point (1, 1, 1.4 mm) calculated by 3DIMPACT at three different in-plane dimensions $((0^0,90^0)_6$, 2600 g and 3 m/sec).

Figure 6.65 History of the strains ε_1, ε_2 and γ_{12} at a given point (1, 1, 1.4 mm) calculated by 3DIMPACT at three different in-plane dimensions $((0^0,90^0)_6$, 2600 g and 3 m/sec).
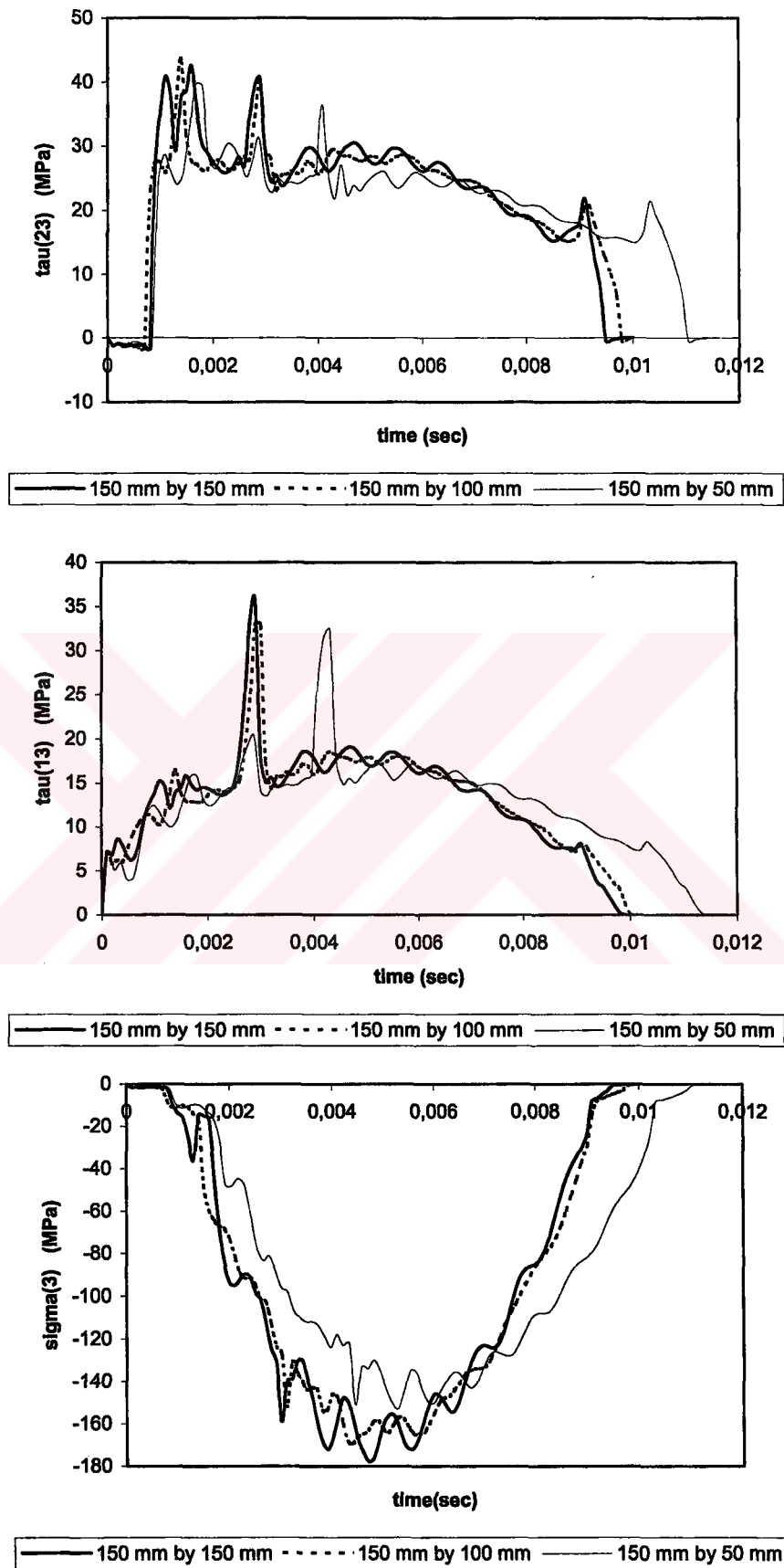
Figure 6.66 History of the strains γ_{23}, γ_{13} and ε_3 at a given point (1, 1, 1.4 mm) calculated by 3DIMPACT at three different in-plane dimensions $((0^0,90^0)_6$, 2600 g and 3 m/sec).
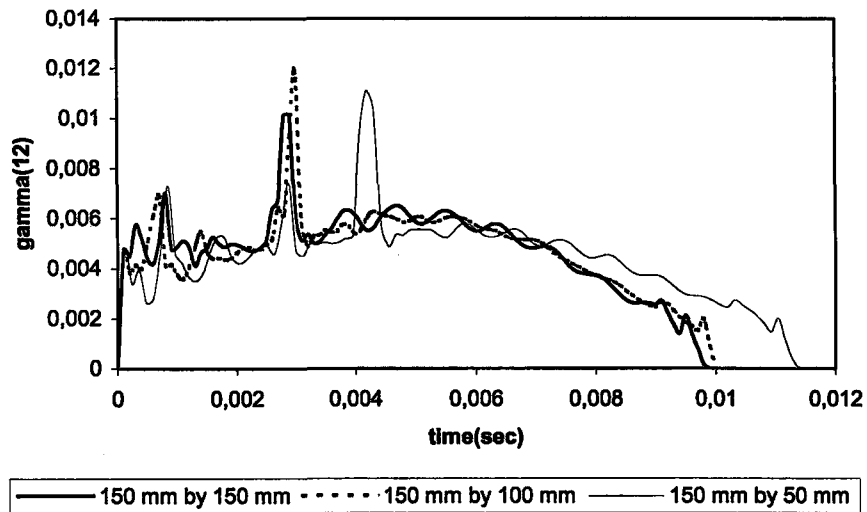
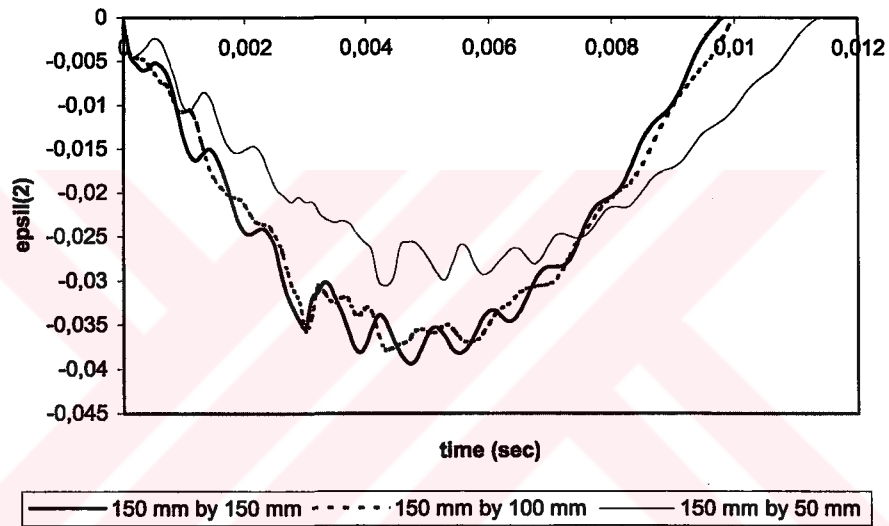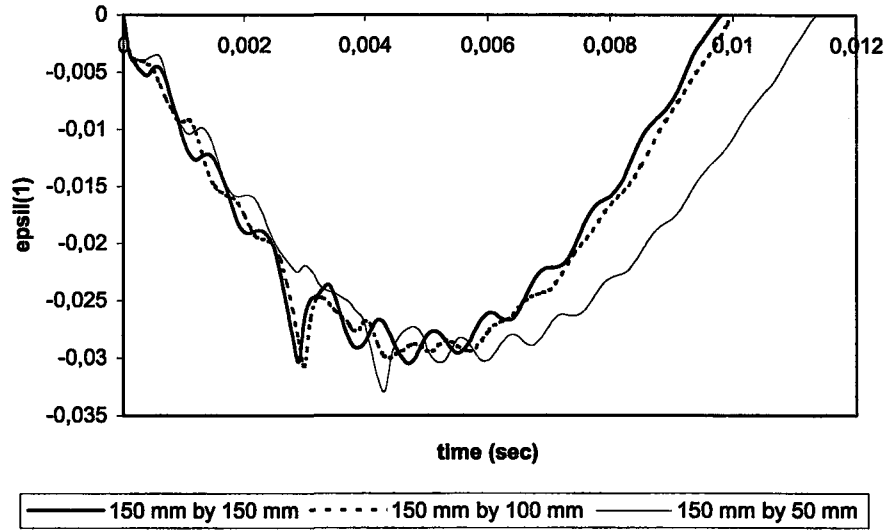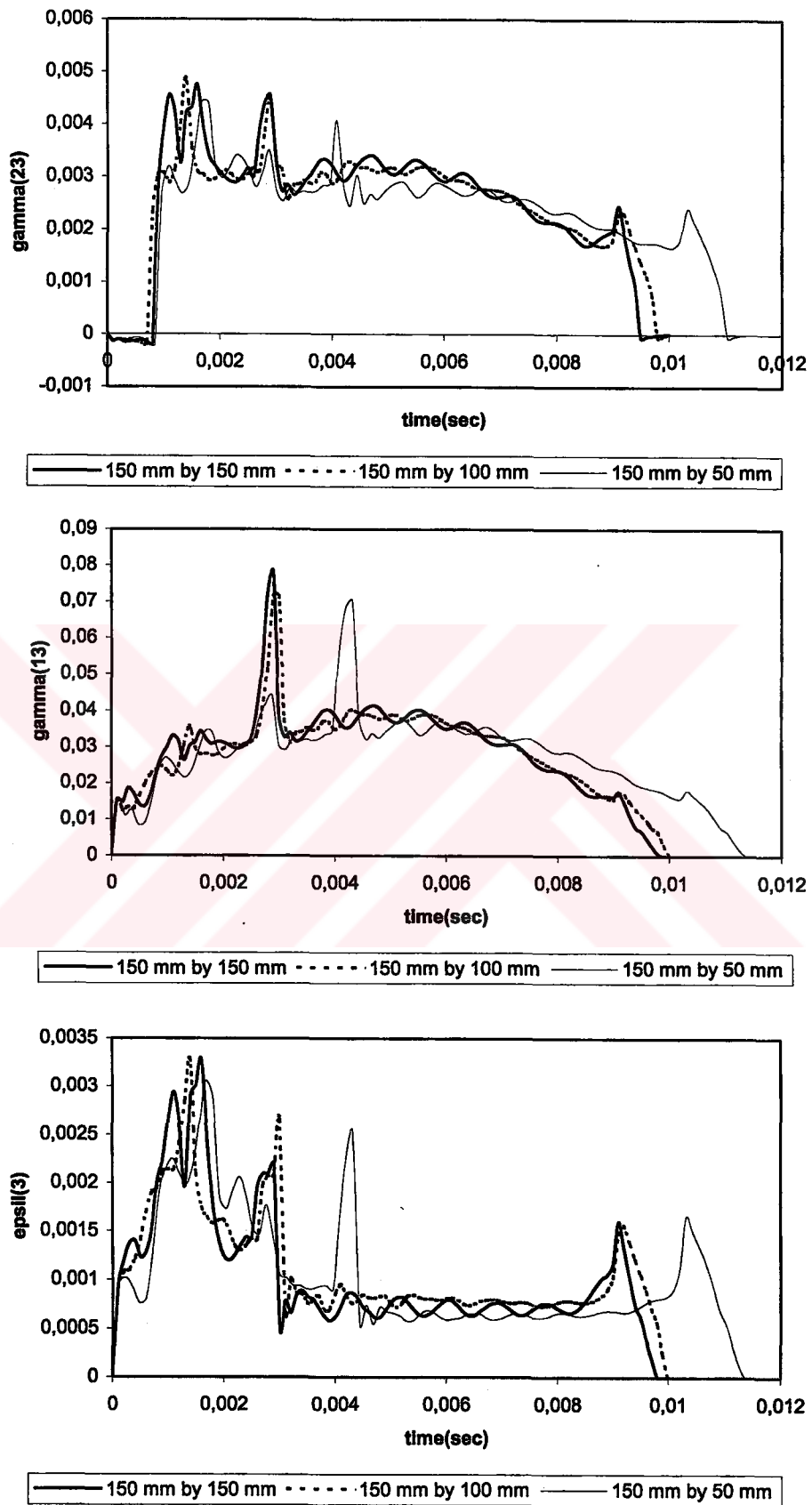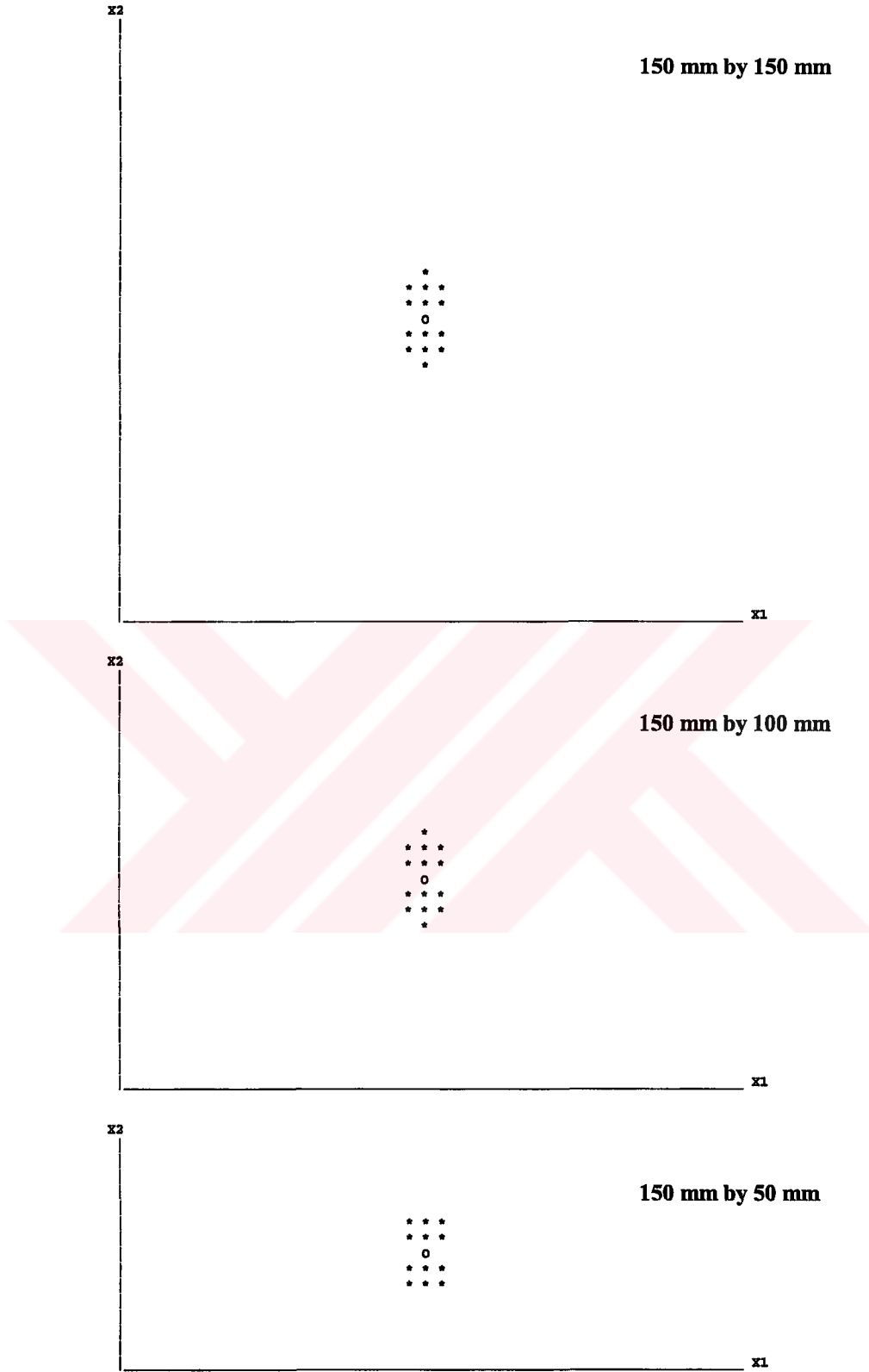**Figure 6.67** Predicted major delaminations at three different in-plane dimensions $((0^0,90^0)_6,$ 2600 g and 3 m/sec).

6.7 Thickness Effects

The impact response of composite laminates changes significantly as the laminate thickness increases. The reason of this behavior is the flexural and contact stiffness varying according to thickness and thereby, causing the impact behavior of a structure to change. Therefore, it is important to determine the impact response of laminated E-glass/epoxy composite plates with respect to thickness. In the present thesis, lay-up of woven fiber laminates are $(0^0,90^0)_6$. Two nominal thicknesses with averages of 1.4 mm and 2.8 mm are used for analyzing the thickness effect. 1.4 mm specimens are called thin laminates while the 2.8 mm specimens are considered as thick laminates.

Figure 6.68 shows the impact characteristics of both thick and thin laminates. It can be concluded that the higher the thickness of the composite laminate, the higher the peak force. But the contact time duration decreases with the increasing thickness. This behavior is essentially the same for all the laminated plate dimensions.

Effect of thickness on center deflection histories of a laminated composite plate is given in Figure 6.69. The in-plane stresses, σ_1, σ_2 and τ_{12} are presented for two different thicknesses in Figure 6.70. The transverse shear stresses τ_{23}, τ_{13} and σ_3 are presented for two different thicknesses in Figure 6.71. The laminate thickness has a significant effect on the normal stresses at the top center of the laminate. For a thicker laminate, normal stresses σ_1 and σ_2, are greatly reduced but the transverse shear stresses τ_{13} and τ_{23} are only slightly less than that of the thinner laminate.

The transient strains are presented in Figures 6.72, 6.73. The numerical simulations of the delamination shape and size at the interface containing the major delamination of the laminates are shown in Figure 6.74. Apparently, delamination in thin laminates is more serious than that in thick laminates. Impact damage behavior changes with the thickness.
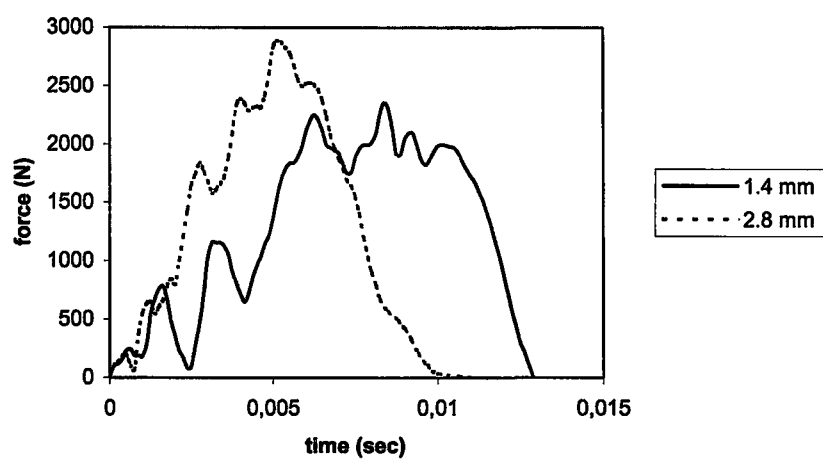
(a)
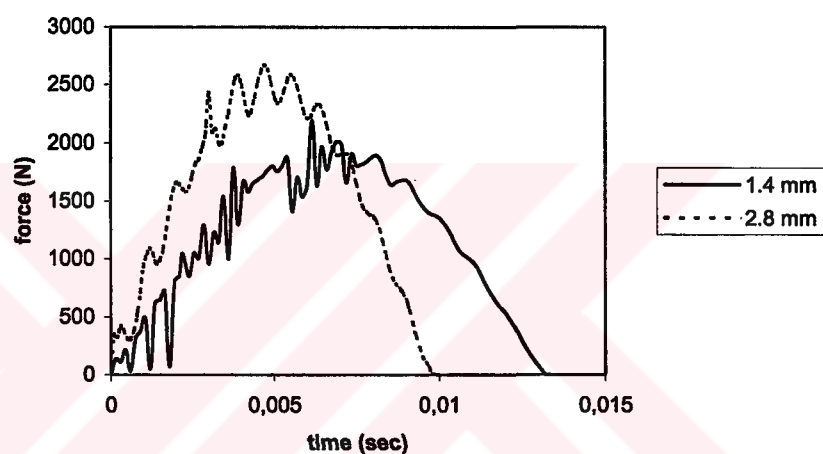
(b)

Figure 6.68 Comparison of force histories at two different thicknesses $((0^0,90^0)_6$, 150 mm by 150 mm, 2600 g and 3 m/sec) **(a)** experimental response **(b)** predicted response.
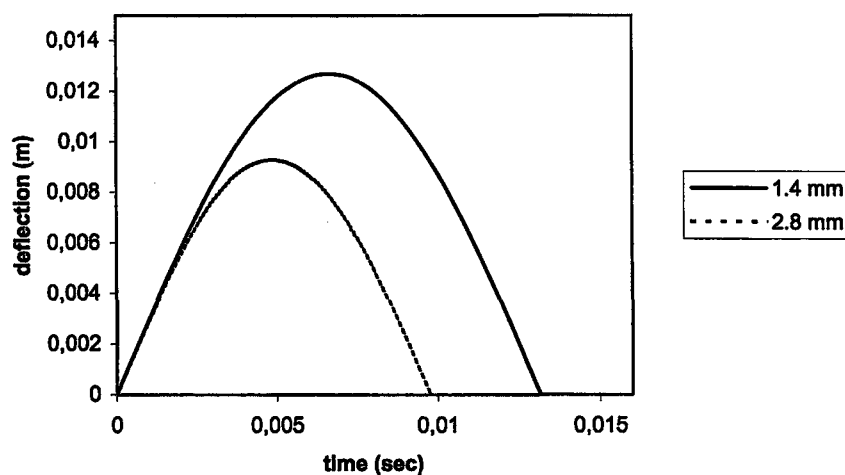

Figure 6.69 Comparison of center deflection histories at two different thicknesses $((0^0,90^0)_6$, 150 mm by 150 mm, 2600 g and 3 m/sec).
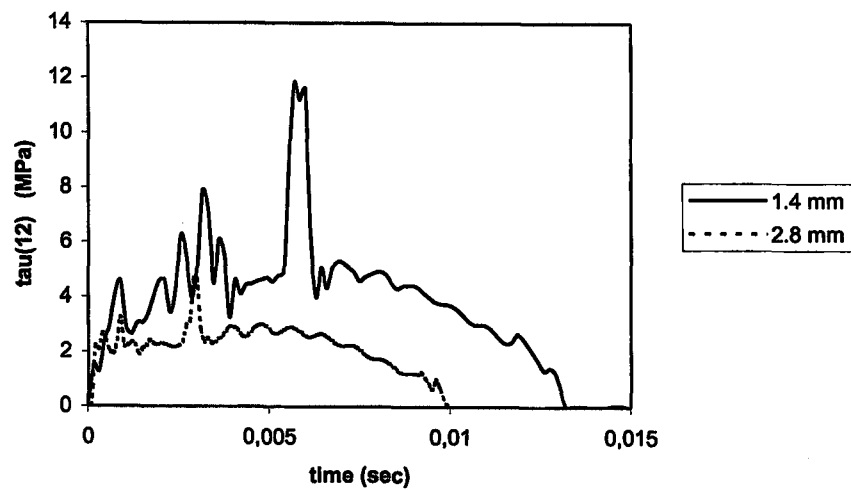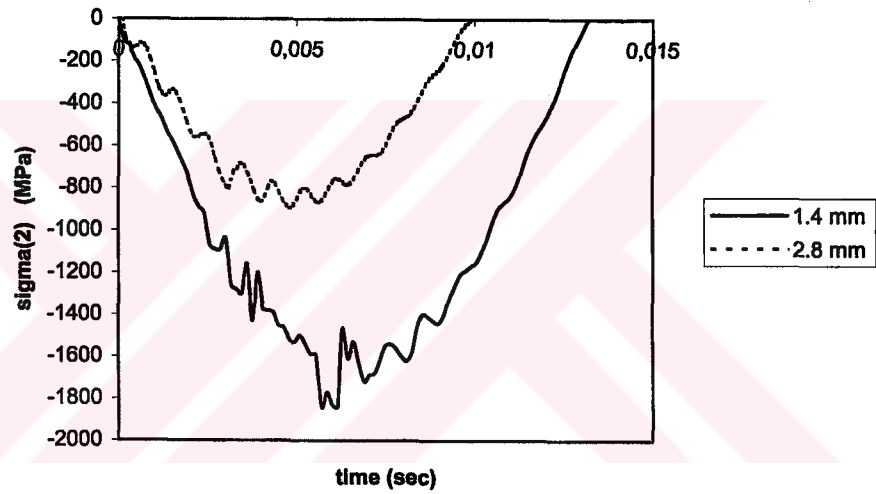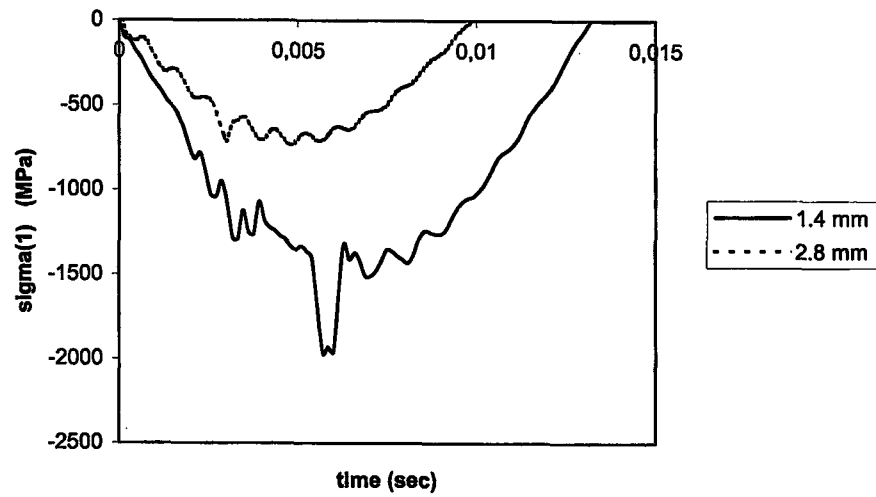
Figure 6.70 History of the stresses σ_1, σ_2 and τ_{12} calculated by 3DIMPACT at two different thicknesses $((0^0,90^0)_6$, 150 mm by 150 mm, 2600 g and 3 m/sec).
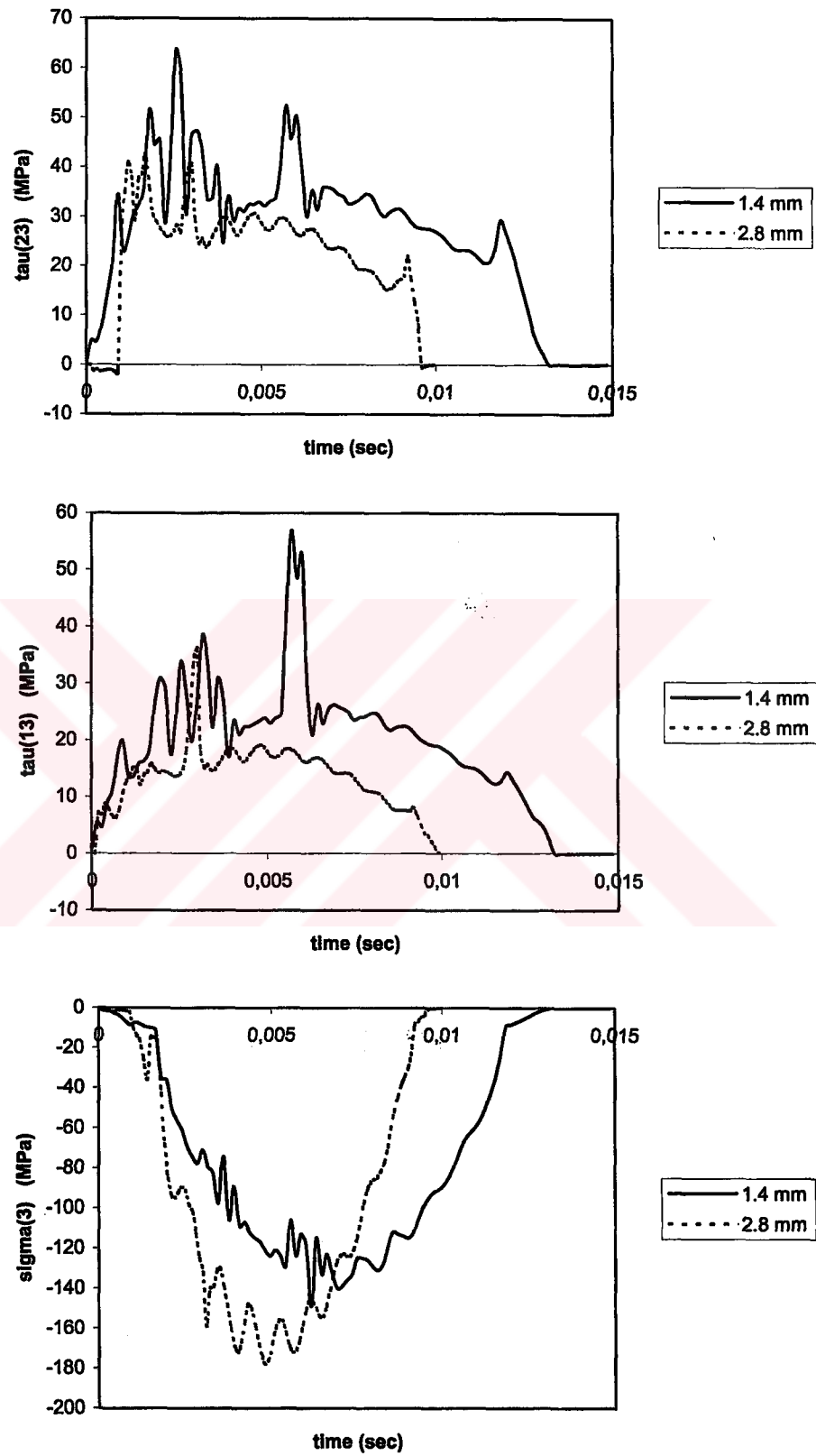
Figure 6.71 History of the stresses τ_{23}, τ_{13} and σ_3 calculated by 3DIMPACT at two different thicknesses $((0^0,90^0)_6$, 150 mm by 150 mm, 2600 g and 3 m/sec).

Figure 6.72 History of the strains ε_1, ε_2 and γ_{12} calculated by 3DIMPACT at two different thicknesses ((0^0,90^0)$_6$, 150 mm by 150 mm, 2600 g and 3 m/sec).
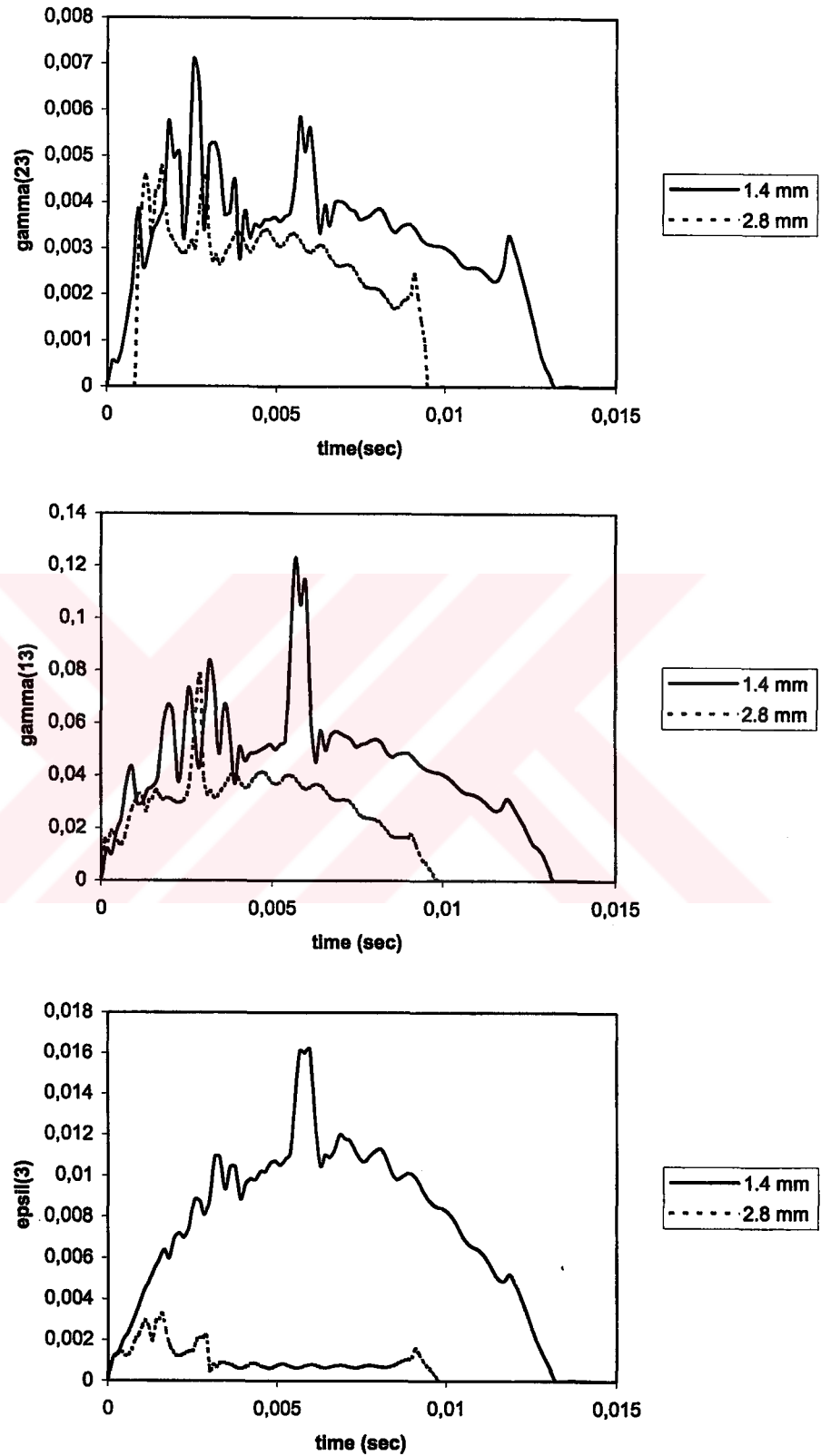
Figure 6.73 History of the strains γ_{23}, γ_{13} and ε_3 calculated by 3DIMPACT at two different thicknesses $((0^0,90^0)_6$, 150 mm by 150 mm, 2600 g and 3 m/sec).
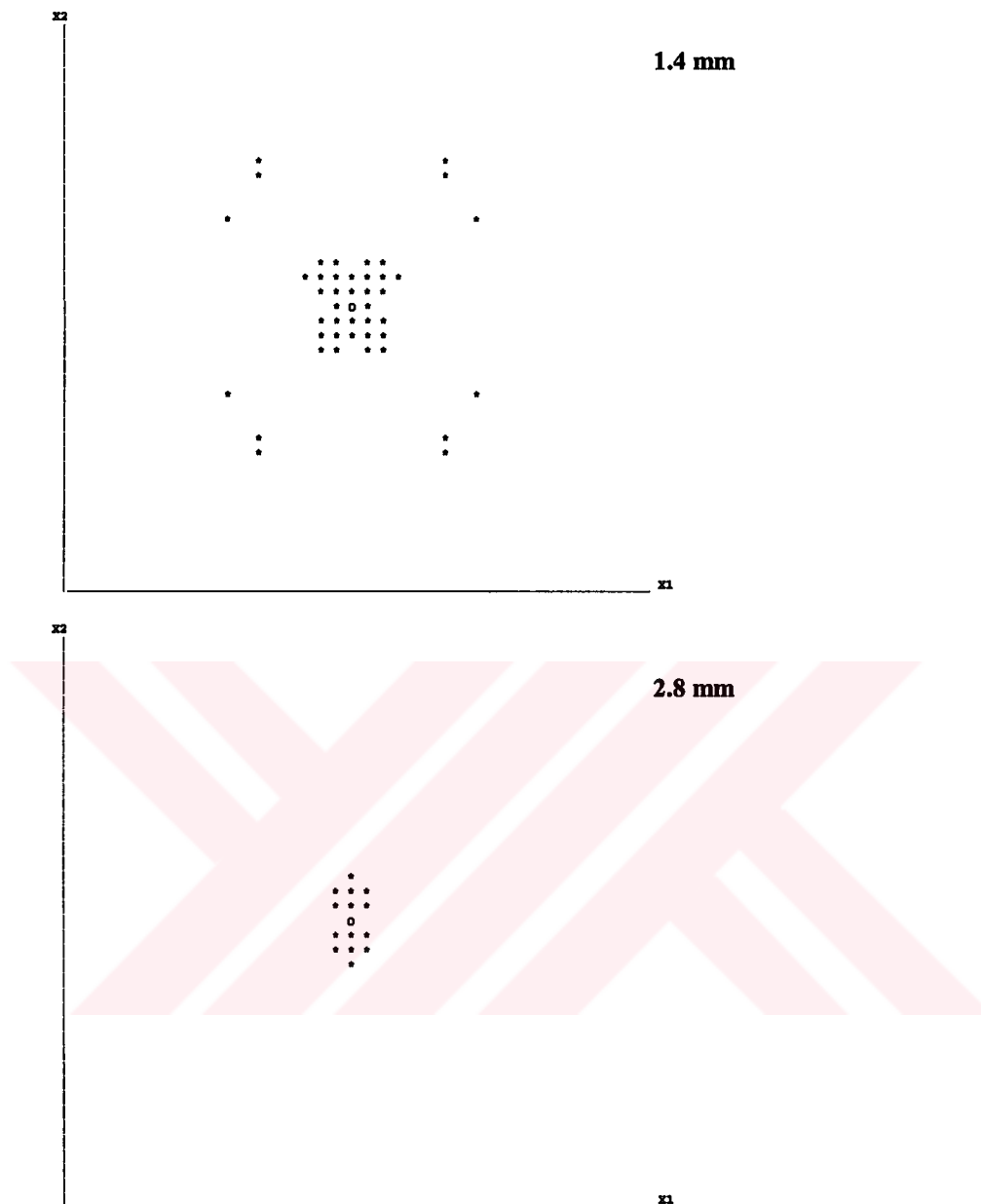
Figure 6.74 Predicted major delaminations at two different thicknesses $((0^0,90^0)_6$, 150 mm by 150 mm, 2600 g and 3 m/sec).

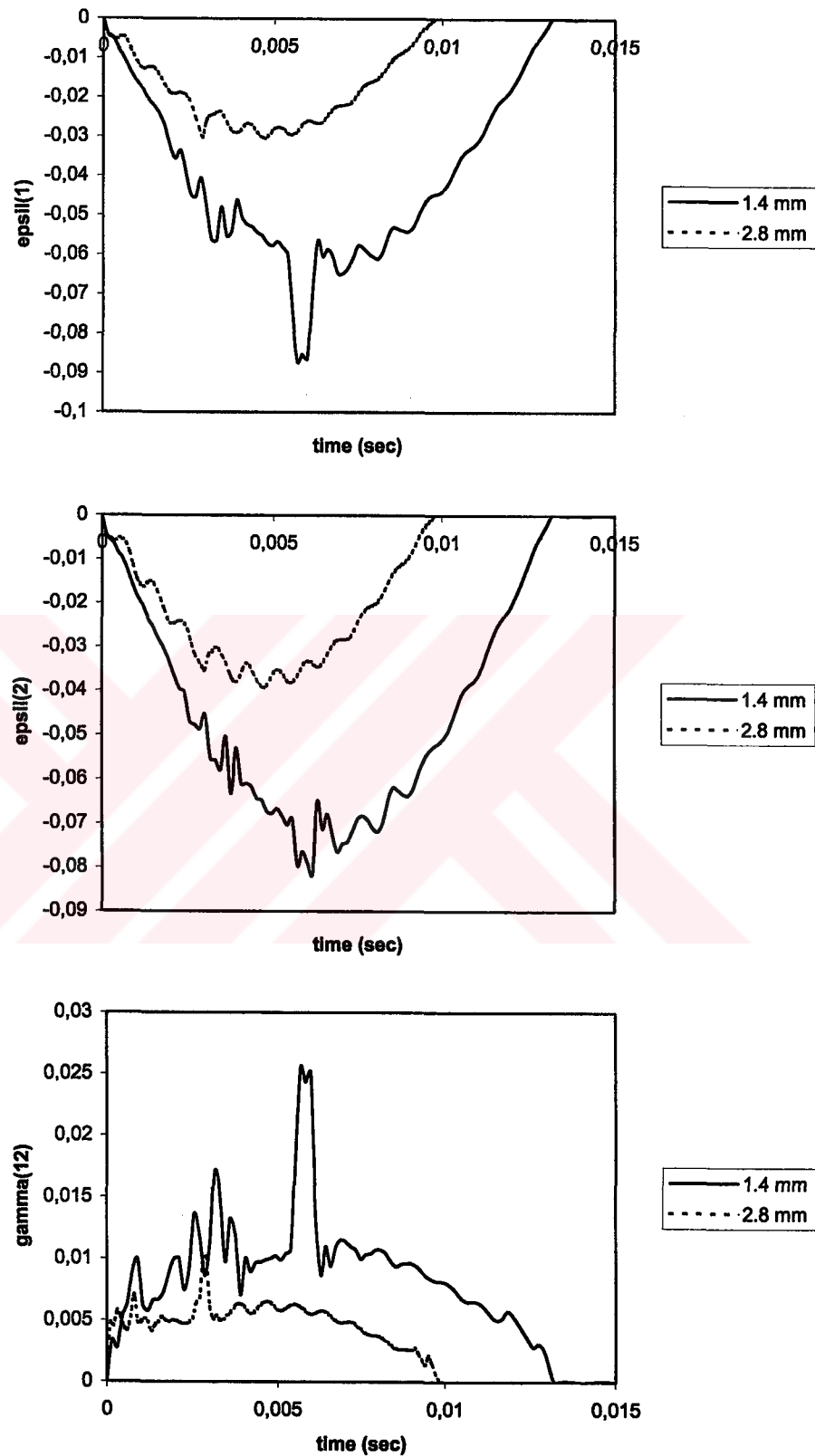In fact, the result that higher the thickness of the specimens have higher peak forces coincides with the fact that the higher thickness of the laminates the stiffer the composite laminate.

The dynamic response, such as the impact force, is greatly influenced by the thickness. The thickness of composite materials is a dominant parameter that governs the dynamic response and damage mode of impacted ones.

CHAPTER SEVEN

CONCLUSIONS AND RECOMMENDATIONS

7.1 Conclusions

The impact behavior of E-glass/epoxy laminated composite plates under low velocities is considered experimentally and numerically. A range of laminated composite plates is impacted under different impact conditions using a drop-weight apparatus. A numerical evaluation of these specimens is also carried out by using 3DIMPACT transient dynamic finite element analysis code. From the results obtained, the main conclusions are as follows:

- The contact force is directly proportional to the impact velocity while the duration of contact is insensitive to it. Concerning the effects of projectile velocity on the dynamic response of an impacted laminate, it is found that the impact forces and center deflections, transient stresses and strains and delaminated area are directly proportional to the projectile velocity.

- The heavier impactor mass would increase the contact force as well as the contact duration. The shape of the force history changes noticeably as the mass varies. The magnitude of contact forces, deflections, stresses and strains, and delaminated area increases as the impactor mass increases. Similarly the duration of contact increases as the mass increases.

- Impact response is dependent on laminate geometries. For unidirectional fiber reinforced laminated composite, the smaller the width of the rectangular composite laminate the higher the contact duration and the highest impact
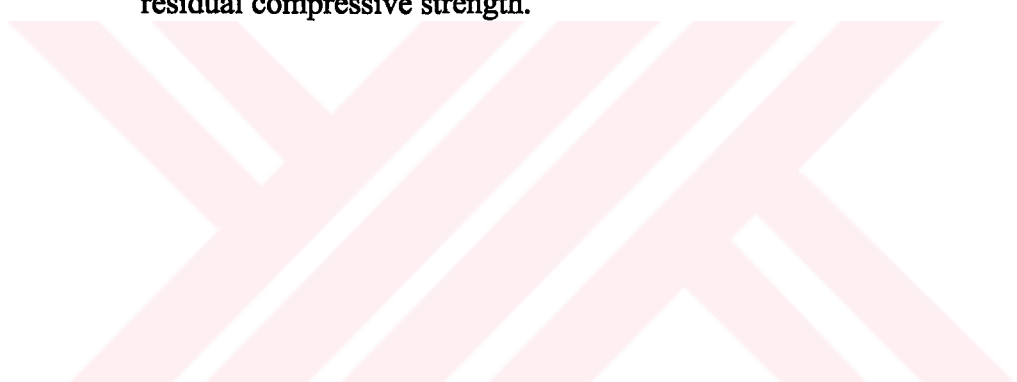
force is obtained for intermediate rectangular specimens (150 mm by 100 mm). For woven reinforced laminates, the result that rectangular specimens with larger widths have higher peak forces coincides with the fact that the larger the width of the laminate dimensions the stiffer the composite laminate.

- The dynamic response, such as the impact force, is greatly influenced by the thickness. The thickness of the composite materials is a dominant parameter that governs the dynamic response and damage mode of impacted ones. The impact response of the composite laminates changes significantly as the laminate thickness increases. The reason of this behavior is the flexural and contact stiffness varying according to thickness and thereby, causing the impact behavior of a structure to change. The higher the thickness of the composite laminate the higher the peak force. But the contact time duration decreases with the increasing thickness. Apparently, delamination in thin laminates is more serious than that in thick laminates. Impact damage behavior changes with the thickness.

7.2 Recommendations

The following recommendations may be listed for further studies on the subject:

- The impact response of various composite materials such as carbon/epoxy or kevlar/epoxy may be evaluated.
- The impact response of various laminate orientations, number of plies and fiber volume fraction may be evaluated.
- The numerical approach for damage initiation and growth may be compared with experimental observations and measurements.
- The dynamic strains of the composite plate under low velocity impact may be measured using strain gage conditioning amplifier.
- High velocity impact may be studied.

- The effect of temperature on the low velocity impact response may be evaluated.

- Effect of low energy impact on the fatigue behavior of composites may be studied. The fatigue behavior of the impacted and unimpacted laminates may be compared.

- The fracture mechanism of impact-induced delamination may be studied in laminated composite under drop-weight impact.

- The effect of impact damage on the subsequent load carrying capability of the laminates may be assessed through a series of in-plane tension tests on damaged specimens.

- Compression after impact (CAI) tests may be performed to measure the residual compressive strength.

CHAPTER EIGHT
REFERENCES

Abatan, A., Hu, H., & Olowokere, D. (1998). Impact resistance modelling of hybrid laminated composites. Journal of Thermoplastic Composite Materials, 11, 249-260.

Abrate, S. (1998). Impact on composite structures. Cambridge, Cambridge University Press.

Aggour, H., & Sun, C.T. (1988). Finite element analysis of a laminated composite plate subjected to circularly distributed central impact loading. Computers & Structures, 28, 729-736.

Aktaş, A., & Karakuzu, R. (1999). Failure analysis of two-dimensional carbon-epoxy composite plate pinned joint. Mech Comp Mater Struc, 6, 347-361.

Asp, L.E., Nilsson, S., & Singh, S. (2001). An experimental investigation of the influence of delamination growth on the residual strength of impacted laminates. Composites: Part A, 32, 1229-1235.

ASTM Standards and Literature References for Composite Materials. (1990). Standard test method for tensile properties of fiber-resin composites D 3039-76. American Society for Testing and Materials, Philadelphia, PA.

ASTM Standards and Literature References for Composite Materials. (1990). Standard test method for compressive properties of unidirectional or cross ply fiber-resin composites D 3410-87. American Society for Testing and Materials, Philadelphia, PA.

ASTM Standards and Literature References for Composite Materials. (1990). D 3846-79. American Society for Testing and Materials, Philadelphia, PA.

Batdorf, S.B. (1989). Note on composite size effects. J Composite Tecnol Res, 45, 35-37.

Bathe, K.J. (1996). Finite element procedures. Newjersey, Printice-Hall.

Belingardi, G., Gugliotta, A., & Vadori, R. (1998). Numerical simulation of fragmentation of composite material plates due to impact. International Journal of Impact Engineering, 21, 335-347.

Besant, T., Davies, G.A.O., & Hitchings, D. (2001). Finite element modelling of low velocity impact of composite sandwich panels. Composites: Part A, 32, 1189-1196.

Birman, V., Chandrashekhara, K., & Sain, S. (1996). An approach to optimization of shape memory alloy hybrid composite plates subjected to low-velocity impact. Composites: Part B, 27B, 439-446.

Bland, P.W., & Dear, J.P. (2001). Observations on the impact behaviour of carbon-fibre reinforced polymers for the qualitative validation of models. Composites: Part A, 32, 1217-1227.

Cairns, D.S., & Lagece, P.A. (1989). Transient response of graphite/epoxy and kevlar /epoxy laminates subjected to impact. AIAA Journal, 27, 1590-1596.

Caprino, G., Lopresto, V., Scarponi, C., & Briotti, G. (1999). Influence of material thickness on the response of carbon-fabric/epoxy panels to low velocity impact. Composites Science and Technology, 59, 2279-2286.

Chandrashekhara, K., & Schroeder, T. (1995). Nonlinear impact analysis of laminated cylindrical and doubly curved shells. Journal of Composite Materials, 29, 2160-2179.

Chandrashekhara, K., Okafor, A.C., & Jiang, Y.P. (1998). Estimation of contact force on composite plates using impact-induced strain and neural networks. Composites: Part B, 29B, 363-370.

Chang, C., & Sun, C.T. (1989). Determining transverse impact on a composite laminate by signal deconvolution. Experimental Mechanics, 29, 414-419.

Chang, F.K., & Lessard, L.B. (1991). Damage tolerance of laminated composites containing an open hole and subjected to compressive loading: Part I-Analysis. Journal of Composite Materials, 25, 2-43.

Chen, J.K., & Sun, C.T. (1985). On the impact of initially stressed composite laminates. Journal of Composite Materials, 19, 490-504.

Choi, H.Y., Downs, R.J., & Chang, F.K. (1991 a). A new approach toward understanding damage mechanisms and mechanics of laminated composites due to

low-velocity impact, Part I-Experiments. Journal of Composite Materials, 25, 992-1011.

Choi, H.Y., Wu, H.Y.T., & Chang, F.K. (1991 b). A new approach toward understanding damage mechanisms and mechanics of laminated composites due to low-velocity impact: Part II- Analysis. Journal of Composite Materials, 25, 1012-1038.

Choi, H.Y., & Chang, F.K. (1992). A model for predicting damage in graphite/epoxy laminated composites resulting from low-velocity point impact. Journal of Composite Materials, 26, 2134-2169.

Choi, I.H., & Hong, C.S. (1994). New approach for simple prediction of impact force history on composite laminates. AIAA Journal, 32, 2067-2072.

Chotard, T.J., & Benzeggagh, M.L. (1998). On the mechanical behaviour of pultruded sections submitted to low-velocity impact. Composites Science and Technology, 58, 839-854.

Christoforou, A.P., & Swanson, S.R. (1991). Analysis of impact response in composite plates. International Journals of Solids and Structures, 27, 161-170.

Christoforou, A.P., & Yiğit, A.S. (1996). Impact of composite structures-the momentum balance method. Journal of Composite Materials, 30, 1068-1087.

Chun, L., & Lam, K.Y. (1998). Dynamic response of fully-clamped laminated composite plates subjected to low-velocity impact of a mass. International Journals of Solids and Structures, 35, 963-979.

Davies, G.A.O., & Zhang, X. (1995). Impact damage prediction in carbon composite structures. International Journal of Impact Engineering, 16, 149-170.

Davies, G.A.O., Hitchings, D., & Zhou, G. (1996). Impact damage and residual strengths of woven fabric glass/polyester laminates. Composites: Part A, 27A, 1147-1156.

Dobyns, A.L. (1981). Analysis of simply-supported orthotropic plates subjected to static and dynamic loads. AIAA Journal, 19, 642-650.

Doyle, J.F. (1987). Determining the contact force during the transverse impact of plates. Experimental Mechanics, 27, 68-72.

Found, M.S., Howard, I.C., & Paran, A.P. (1997). Size effects in thin CFRP panels subjected to impact. Composite Structures, 38, 599-607.

Freitas, M., Silva, A., & Reis, L. (2000). Numerical evaluation of failure mechanisms on composite specimens subjected to impact loading. Composites: Part B, 31, 199-207.

Geubelle, P.H., & Baylor, J.S. (1998). Impact-induced delamination of composites: a 2D simulation. Composites: Part B, 29B, 589-602.

Gong, S.W., & Lam, K.Y. (1999). Transient response of stiffened composite plates subjected to low velocity impact. Composites: Part B, 30, 473-484.

Goo, N.S., & Kim, S.J. (1997). Dynamic contact analysis of laminated composite plates under low-velocity impact. AIAA Journal, 35, 1518-1521.

Green, E.R., & Green, W.A. (1992). Reciprocal relations for dynamic Green's Functions in fibre composite laminates. J Mech Phys Solids, 40, 1495-1506.

Green, E.R. (1993). Response of a fibre composite laminate to a time-varying surface line load. Journal of Applied Mechanics, 60, 217-221.

Hou, J.P., Petrinic, N., Ruiz, C., & Hallett, S.R. (2000). Prediction of impact damage in composite plates. Composites Science and Technology, 60, 273-281.

Hu, N., Sekine, H., Fukunaga, H., & Yao, Z.H. (1999). Impact analysis of composite laminates with multiple delaminations. International Journal of Impact Engineering, 22, 633-648.

Jih, C.J., & Sun, C.T. (1993). Prediction of delamination in composite laminates subjected to low velocity impact. Journal of Composite Materials, 27, 684-701.

Jones, R.M. (1998). Mechanics of composite materials. Kogakusha, Tokyo:McGraw-Hill.

Joshi, S.P., & Sun, C.T. (1985). Impact induced fracture in a laminated composite. Journal of Composite Materials, 19, 51-66.

Kim, J.K., & Sham, M.L. (2000). Impact and delamination failure of woven-fabric composites. Composites Science and Technology, 60, 745-761.

Kim, J.K., & Kang, K.W. (2001). An analysis of impact force in plain-weave glass/epoxy composite plates subjected to transverse impact. Composites Science and Technology, 61, 135-143.

Kistler, L.S., & Waas, A.M. (1998). Impact response of cylindrically curved laminates including a large deformation scaling study. International Journal of Impact Engineering, 21, 61-75.

Kwon, Y.W., & Wojcik, G.W. (1998) Impact study of sandwich composite structures with delamination. Journal of Composite Materials, 32, 406-430.

Lagace, P.A. (1986). Private communication. Department of Aeronautics and Astronautic, Massachusetts Institute of Technology.

Lal, K.M. (1982). Prediction of residual tensile strength of transversely impacted composite laminates. Struct. Solid Mech. NASA CP-2245, pp. 97-111.

Lal, K.M. (1983). Low velocity transverse impact behavior of 8-ply graphite-epoxy laminates. Journal of Reinforced Plastics and Composites, 2, 216-225.

Lee, D.G., & Cheon, S.S. (2001). Impact characteristics of glass fiber composites with respect to fiber volume fraction. Journal of Composite Materials, 35, 27-56.

Lee, J.D., Du, S., & Liebowitz, H. (1984). Three dimensional finite element and dynamic analysis of composite laminate subjected to impact. Computers & Structures, 19, 807-813.

Lee, L.J., Huang, K.Y., & Fann, Y.J. (1993) Dynamic responses of composite sandwich plate impacted by rigid ball. Journal of Composite Materials, 27, 1238-1256.

Lee, Y.S., Kang, K.H., & Park, O. (1997). Response of hybrid laminated composite plates under low-velocity impact. Computers & Structures, 65, 965-974.

Lifshitz, J.M. (1976). Impact strength of angle ply fiber reinforced materials. Journal of Composite Materials, 10, 92-101.

Liu, D., Raju, B.B., & Dang, X. (1998). Size effects on impact response of composite laminates. International Journal of Impact Engineering, 21, 837-854.

Liu, S. (1993). Indentation damage initiation and growth of thick-section and toughened composite materials. ASME Publication, AD-Vol.37, AMD-Vol.179, 103-116.

Liu, S., Kutlu, Z., & Chang, F.K. (1993 a). Matrix cracking and delamination propagation in laminated composites subjected to transversely concentrated loading. Journal of Composite Materials, 27, 436-470.

Liu, S., Kutlu, Z., & Chang, F.K. (1993 b). Matrix cracking-induced stable and unstable delamination propagation in graphite/epoxy laminated composites due to a transversely concentrated load. ASTM STP, 1156, 86-101.

Luo, R.K., Green, E.R., & Morrison, C.J. (1999). Impact damage analysis of composite plates. International Journal of Impact Engineering, 22, 435-447.

Mantena, P.R., Mann, R., & Nori, C. (2001). Low-velocity impact response and dynamic characteristics of glass-resin composites. Journal of Reinforced Plastics and Composites, 20, 513-533.

Mili, F., & Necib, B. (2001). Impact behavior of cross-ply laminated composite plates under low velocities. Composite Structures, 51, 237-244.

Naik, N.K., Sekher, Y.C., & Meduri, S. (2000). Damage in woven-fabric composites subjected to low-velocity impact. Composites Science and Technology, 60, 731-744.

Oguibe, C.N., & Webb, D.C. (1999). Finite-element modelling of the impact response of a laminated composite plate. Composites Science and Technology, 59, 1913-1922.

Olsson, R. (2001). Analytical prediction of large mass impact damage in composite laminates. Composites: Part A, 32, 1207-1215.

Park, S.W., Zhou, M., & Veazie, D.R. (2000). Time-resolved impact response and damage of fiber-reinforced composite laminates. Journal of Composite Materials, 34, 879-904.

Pierson, M.O., & Vaziri, R. (1996). Analytical solution for low-velocity impact response of composite plates. AIAA Journal, 34, 1633-1640.

Prasad, C.B., Ambur, D.R., & Starnes, J.H.Jr. (1994). Response of laminated composite plates to low-speed impact by different impactors. AIAA Journal, 32, 1270-1277.

Qian, Y., & Swanson, S.R. (1990). A comparison of solution techniques for impact response of composite plates. Composite Structures, 14, 177-192.

Ramkumar, R.L., & Chen, P.C. (1982). Low-velocity impact response of laminated plates. AIAA Journal, 21, 1448-1452.

Razi, H., & Kobayashi, A.S. (1993). Delamination in cross-ply laminated composite subjected to low-velocity impact. AIAA Journal, 31, 1498-1502.

Reddy, J.N. (1997). Mechanics of laminated composite plates theory and analysis. Florida, CRC Press.

Rotem, A., & Lifshitz, J.M. (1971). Longitudinal strength of unidirectional fibrous composite under high rate of loading. Proc. 26th Annual Tech. Conf. Soc. Plastics Industry, Reinforced Plastics, Composites Division, Washington, DC, Section 10-G: pp.1-10.

Rydin, R.W., & Karbhari, V.M. (1998). Partitioning energy during low-velocity impact of RTM fiber-reinforced composites. International Journal of Impact Engineering, 21, 773-789.

Sankar, B.V., & Sun, C.T. (1985). Low-velocity impact response of laminated beams subjected to initial stresses. AIAA Journal, 23, 1962-1969.

Sankar, B.V. (1992). Scaling of low-velocity impact for symmetric composite laminates. Journal of Reinforced Plastics Composites, 11, 297-305.

Scarponi, C., Briotti, G., Barboni, R., Marcone, A., & Iannone, M. (1996). Impact testing on composite laminates and sandwich panels. Journal of Composite Materials, 30, 1873-1911.

Shadid, I., Sun, H.T., & Chang, F.K. (1995). Prediction scaling effect on the notched strength of prepreg and fiber tow-placed laminated composites. Journal of Composite Materials, 29, 1063-1095.

Sierakowski, R.L., Nevil, G.E., Ross, A., & Jones, E.R. (1971). Dynamic compressive strength and failure of steel reinforced epoxy composites. Journal of Composite Materials, 5, 362-377.

Sierakowski, R.L., & Chaturvedi, S.K. (1997). Dynamic loading and characterization of fiber-reinforced composites. New York, Wiley.

Siow, Y.P., & Shim, V.P.W. (1998). An experimental study of low velocity impact damage in woven fiber composites. Journal of Composite Materials, 32, 1178-1202.

Sjögren, A., Krasnikovs, A., & Varna, J. (2001). Experimental determination of elastic properties of impact damage in carbon fibre/epoxy laminates. Composites: Part A, 32, 1237-1242.

Sohn, M.S., Hu, X.Z., Kim, J.K., & Walker, L. (2000). Impact damage characterisation of carbon fibre/epoxy composites with multi-layer reinforcement. Composites: Part B, 31, 681-691.

Sridhar, C., & Rao, K.P. (1995). Estimation of low-velocity impact damage in laminated composite circular plates using nonlinear finite element analysis. Computers & Structures, 54, 1183-1189.

Sun, C.T., & Chattopadhyay, S. (1975). Dynamic response of anisotropic laminated plates under initial stress to impact of a mass. ASME Journal of Applied Mechanics, 42, 693-698.

Sun, C.T., & Liou, W.J. (1989). Investigation of laminated composite plates under impact dynamic loading using a three-dimensional hybrid stress finite element method. Computers & Structures, 33, 879-884.

Sun, C.T., & Jih, C.J. (1995). Quasi-static modeling of delamination crack propagation in laminates subjected to low-velocity impact. Composites Science and Technology, 54, 185-191.

Tan, T.M., & Sun, C.T. (1985). Use of statical indentation laws in the impact analysis of laminated composite plates. Journal of Applied Mechanics, 52, 6-12.

Taylor, R.L., Beresford, P.J., & Wilson, E.L. (1976). A non-conforming element for stress analysis. Int. J. Numer. Meth. Engng, 10, 1211-1219.

Wang, C.Y., & Yew, C.H. (1990). Impact damage in composite laminates. Computers & Structures, 37, 967-982.

Wang, H., & Vukhanh, T. (1994). Damage extension in carbon fibre/PEEK cross ply laminates under low velocity impact. Journal of Composite Materials, 28, 684-707.

Whitney, J.M., & Pagano, N.J. (1970). Shear deformation in heterogeneous anisotropic plates. Journal of Applied Mechanics, 37, 1026-1031.

Wilson, E.L., Taylor, R.L., Doherty, W.P., & Ghaboussi, J. (1973). Incompatible displacement models-in numerical and computer methods in structural mechanics (Edited by Fenves, S.J., Perrone, N., Robinson, A.R., & Schnobrich, W.C.). NewYork, Academic Press.

Wu, E., & Shyu, K. (1993). Response of composite laminates to contact loads and relationship to low-velocity impact. Journal of Composite Materials, 27, 1443-1464.

Wu, H.Y.T., & Chang, F.K. (1989). Transient dynamic analysis of laminated composite plates subjected to transverse impact. Computers & Structures, 31, 453-466.

Yang, S.H., & Sun, C.T. (1981). Indentation law for composite laminates. NASA CR-165460.

Yang, S.H., & Sun, C.T. (1982). Indentation law for composite laminate. Composite Materials: Testing and Design (6th Conf) ASTM STP 787.1 ASTM Philadelphia PA, pp. 425-449.

CHAPTER NINE
APPENDIXES

9.1 Contact Force History of the Plate $(0^0/0^0/90^0/90^0)_s$
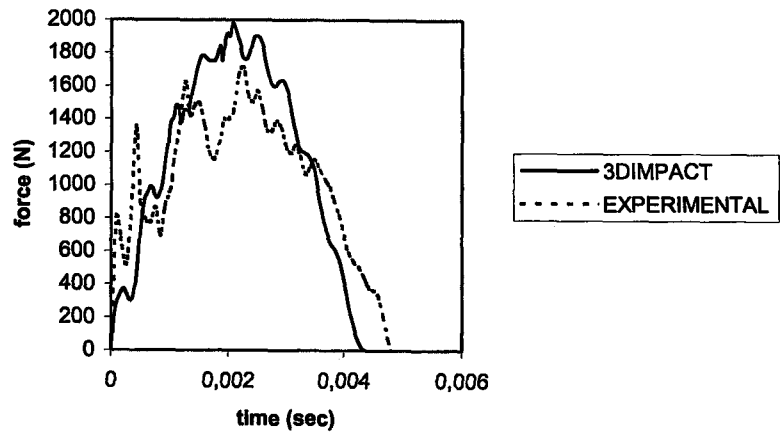
Figure 9.1 Impact force-time history of $(0^0/0^0/90^0/90^0)_s$ laminate under the impact velocity V=1 m/sec and impactor mass m=2600 g (150 mm by 150 mm).
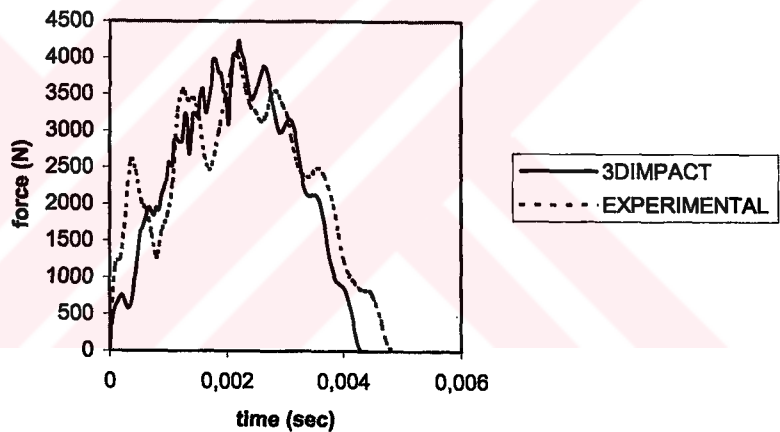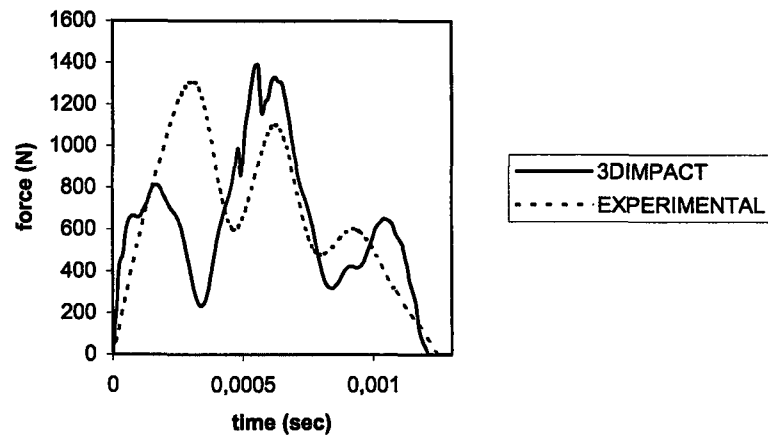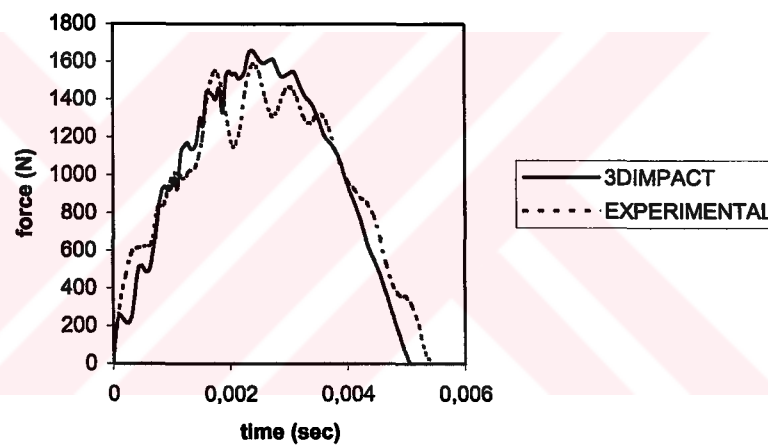

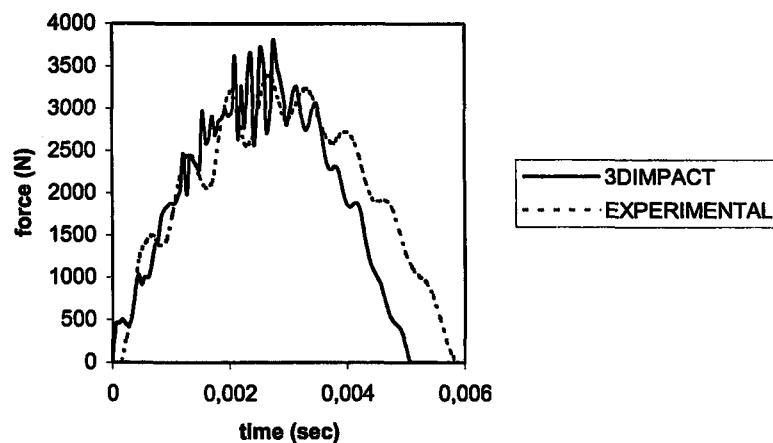
Figure 9.2 Impact force-time history of $(0^0/0^0/90^0/90^0)_s$ laminate under the impact velocity V=2 m/sec and impactor mass m=2600 g (150 mm by 150 mm).
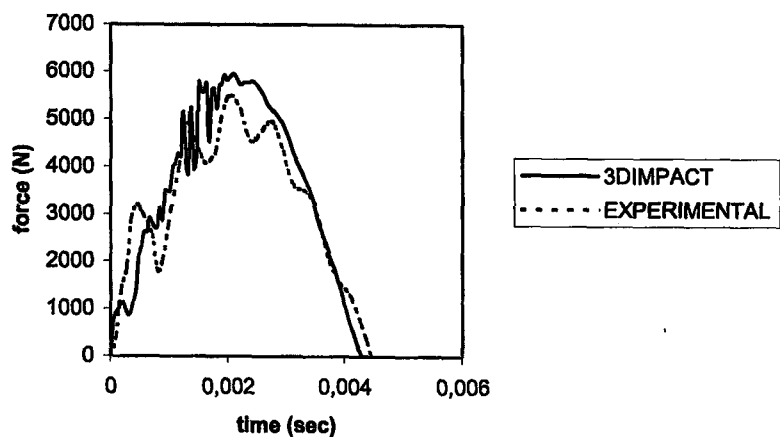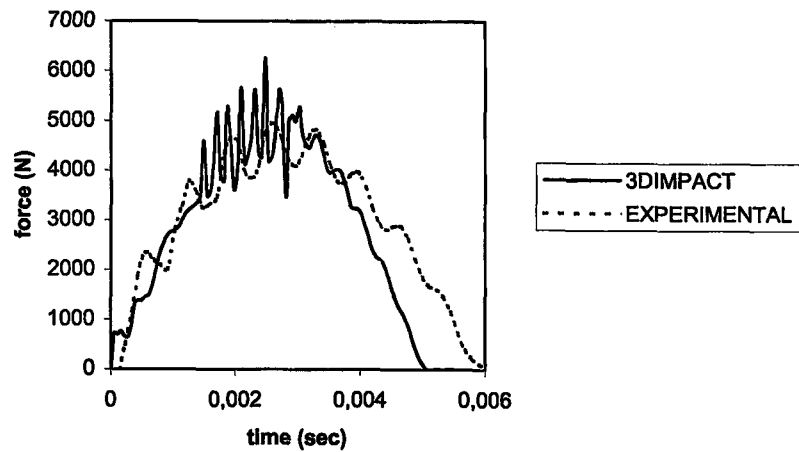

Figure 9.3 Impact force-time history of $(0^0/0^0/90^0/90^0)_s$ laminate under the impact velocity V=3 m/sec and impactor mass m=2600 g (150 mm by 150 mm).
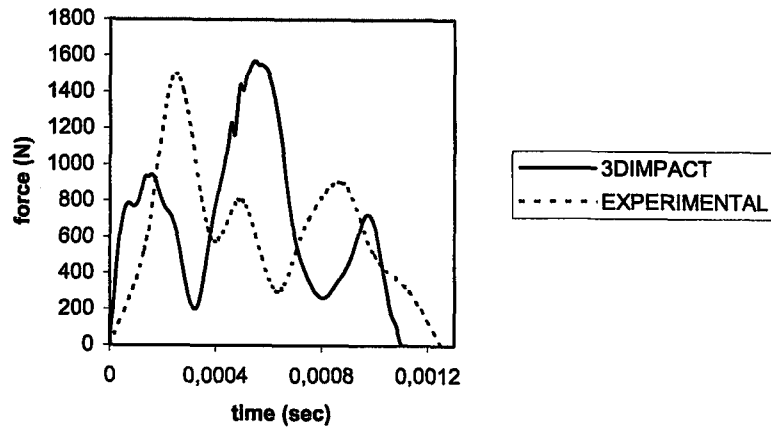
Figure 9.4 Impact force-time history of $(0^0/0^0/90^0/90^0)_s$ laminate under the impact velocity V=3 m/sec and impactor mass m=135 g (150 mm by 150 mm).
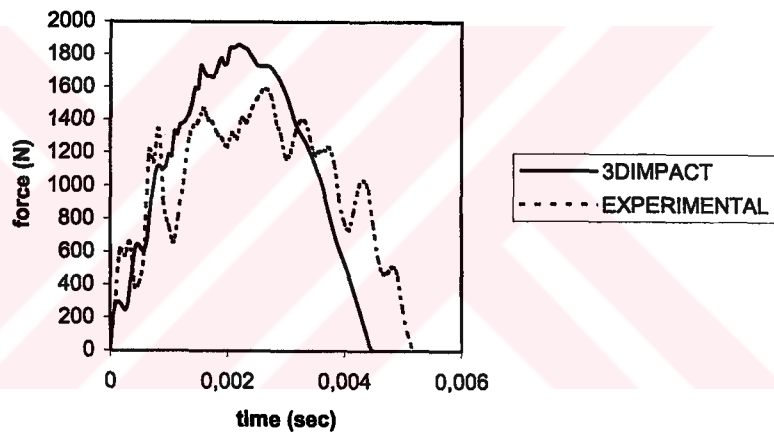
Figure 9.5 Impact force-time history of $(0^0/0^0/90^0/90^0)_s$ laminate under the impact velocity V=1 m/sec and impactor mass m=2600 g (150 mm by 100 mm).
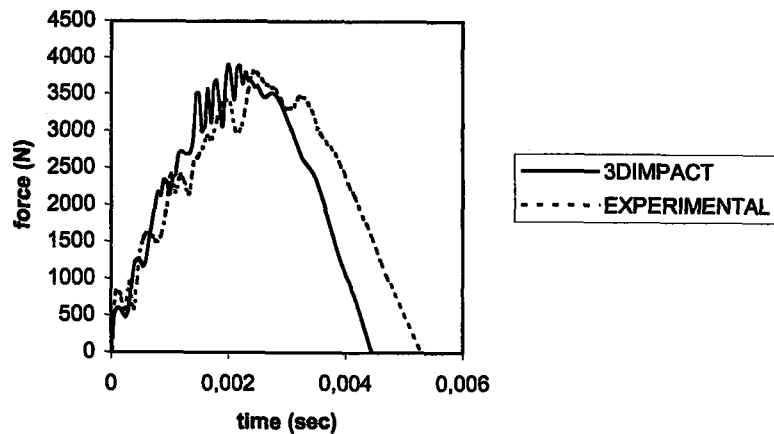
Figure 9.6 Impact force-time history of $(0^0/0^0/90^0/90^0)_s$ laminate under the impact velocity V=2 m/sec and impactor mass m=2600 g (150 mm by 100 mm).
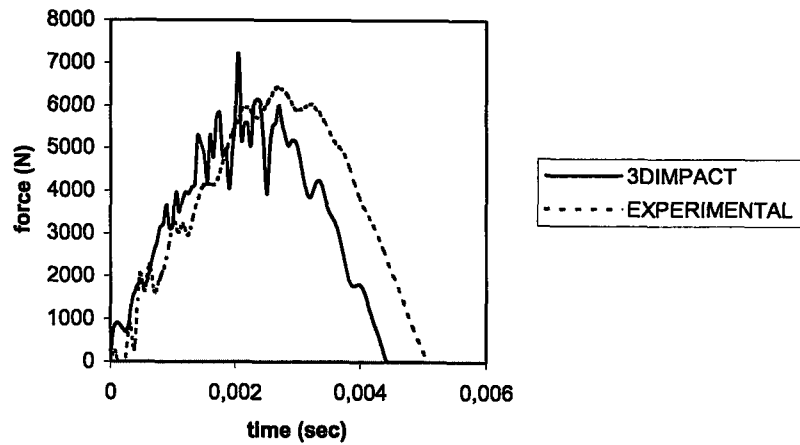
Figure 9.7 Impact force-time history of $(0^0/0^0/90^0/90^0)_s$ laminate under the impact velocity V=3 m/sec and impactor mass m=2600 g (150 mm by 100 mm).
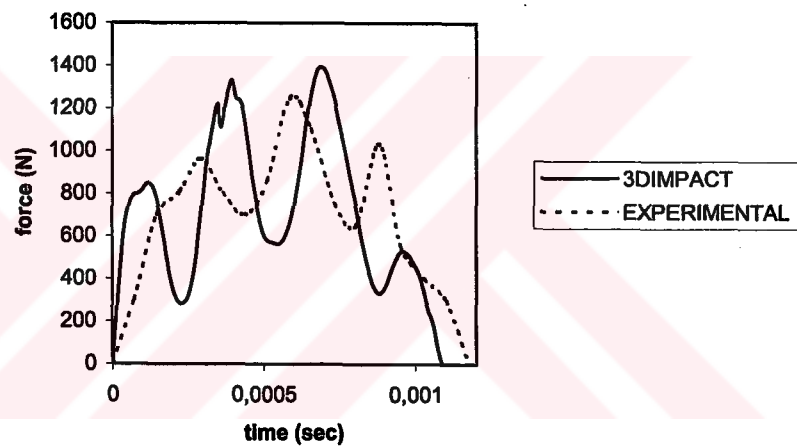
Figure 9.8 Impact force-time history of $(0^0/0^0/90^0/90^0)_s$ laminate under the impact velocity V=3 m/sec and impactor mass m=135 g (150 mm by 100 mm).
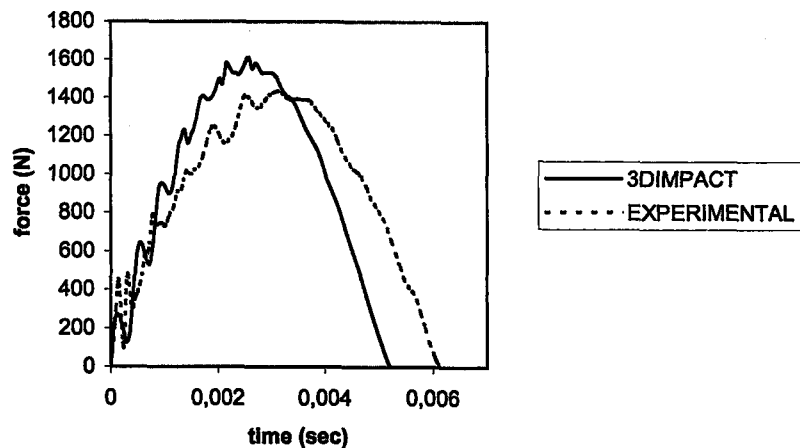
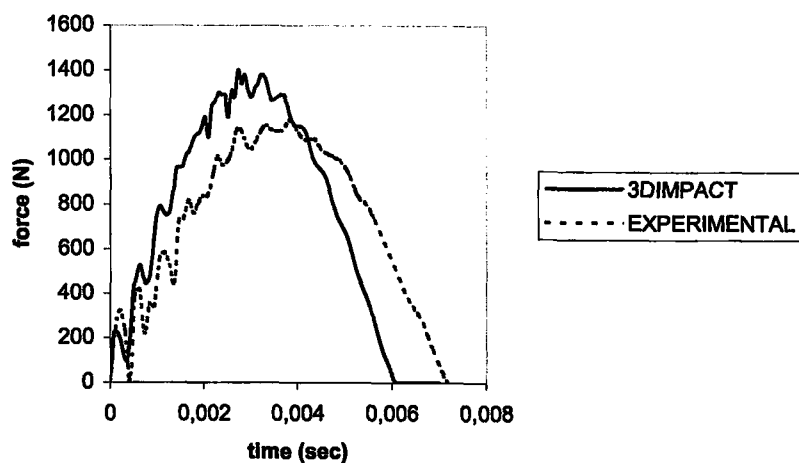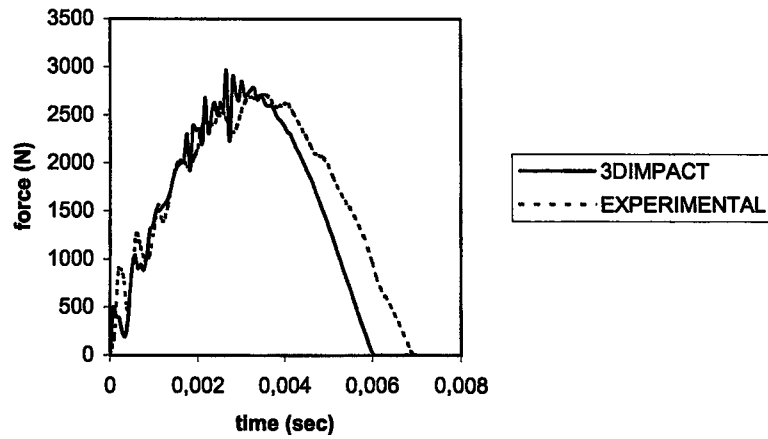**Figure 9.9** Impact force-time history of $(0^0/0^0/90^0/90^0)_s$ laminate under the impact velocity V=1 m/sec and impactor mass m=2600 g (150 mm by 50 mm).
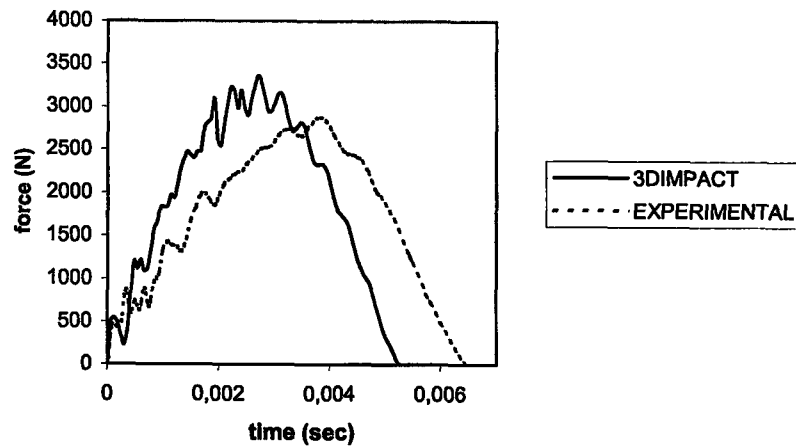
Figure 9.10 Impact force-time history of $(0^0/0^0/90^0/90^0)_s$ laminate under the impact velocity V=2 m/sec and impactor mass m=2600 g (150 mm by 50 mm).
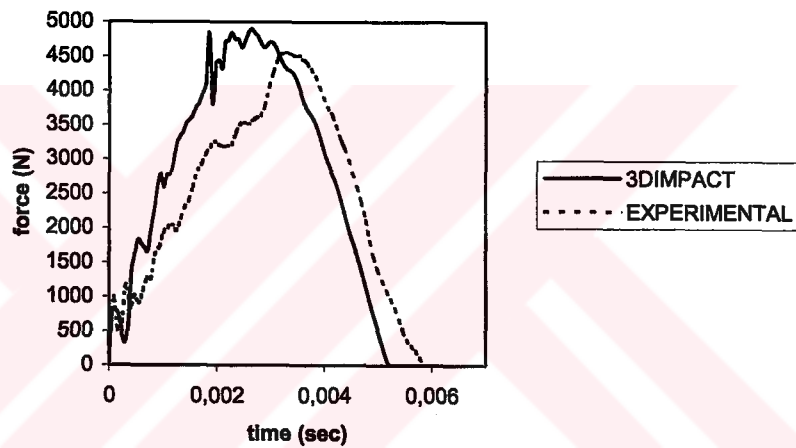
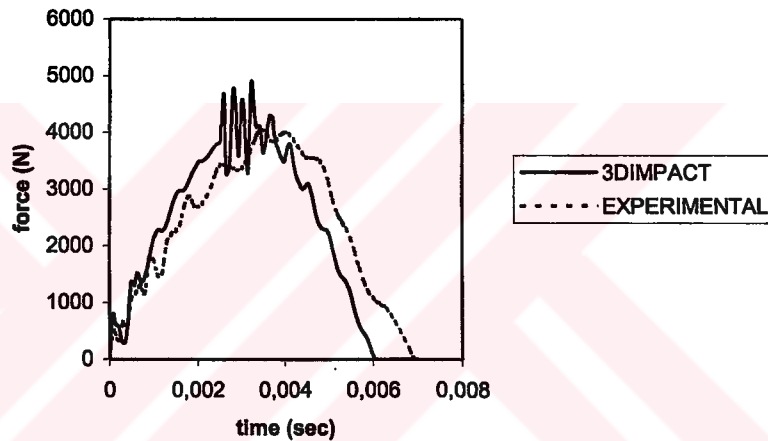**Figure 9.11** Impact force-time history of $(0^0/0^0/90^0/90^0)_s$ laminate under the impact velocity V=3 m/sec and impactor mass m=2600 g (150 mm by 50 mm).
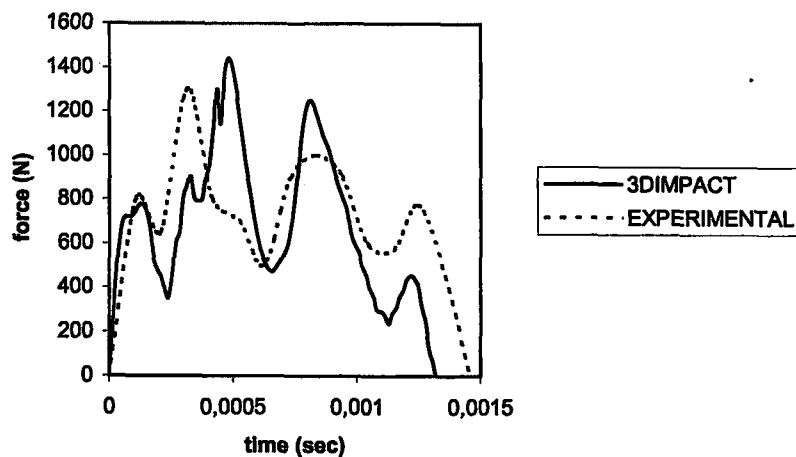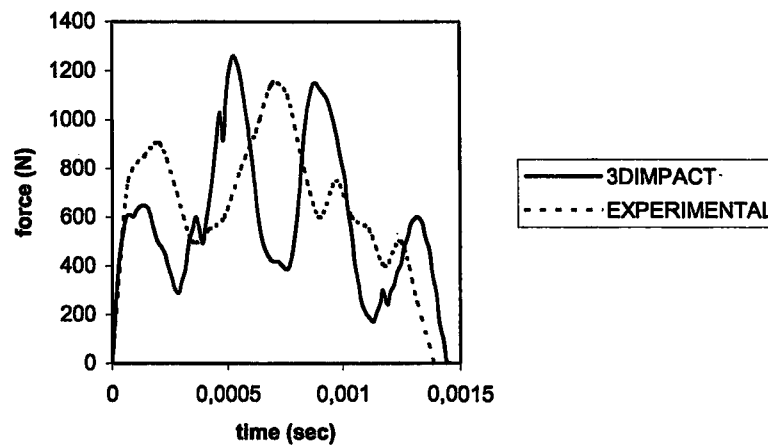

Figure 9.12 Impact force-time history of $(0^0/0^0/90^0/90^0)_s$ laminate under the impact velocity V=3 m/sec and impactor mass m=135 g (150 mm by 50 mm).

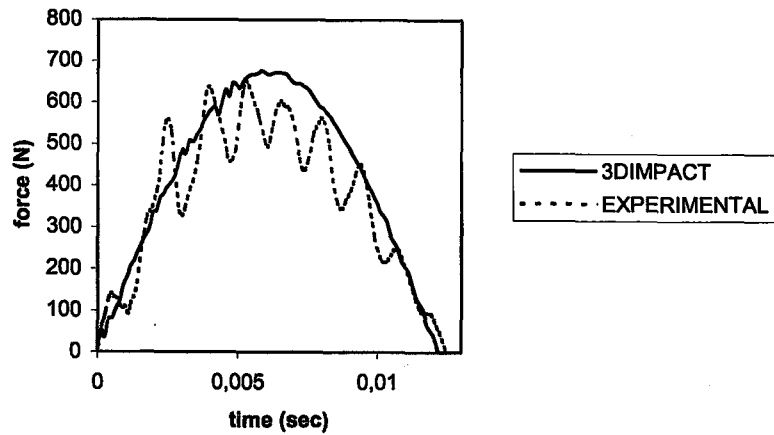## 9.2 Contact Force History of the Plate $(0^{0}/-45^{0}/45^{0})_{s}$
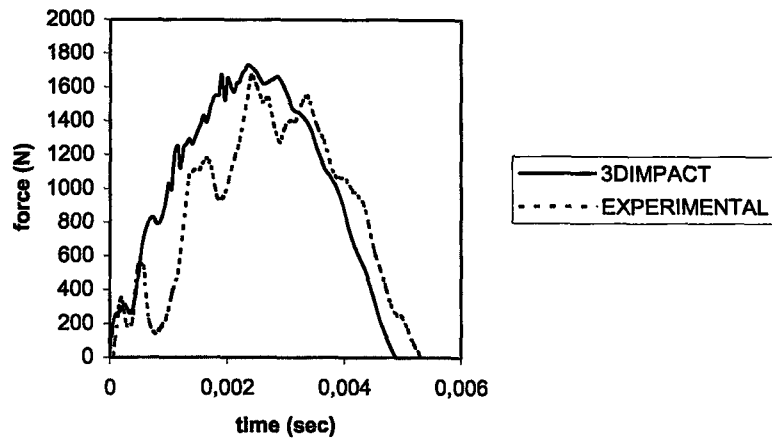
Figure 9.13 Impact force-time history of $(0^{0}/-45^{0}/45^{0})_{s}$ laminate under the impact velocity V=1 m/sec and impactor mass m=2600 g (150 mm by 150 mm).
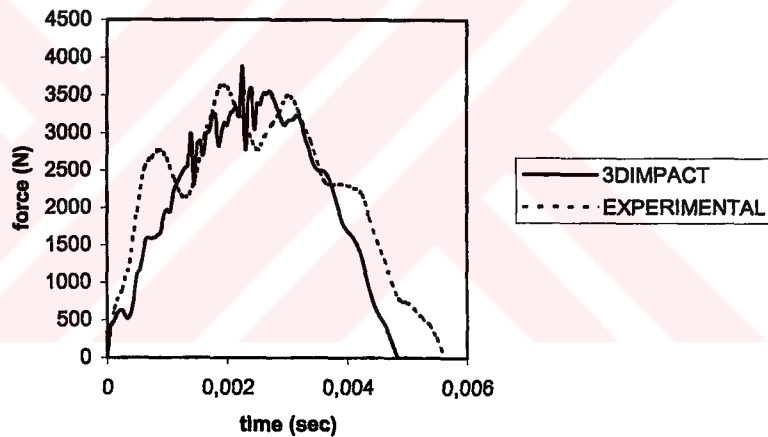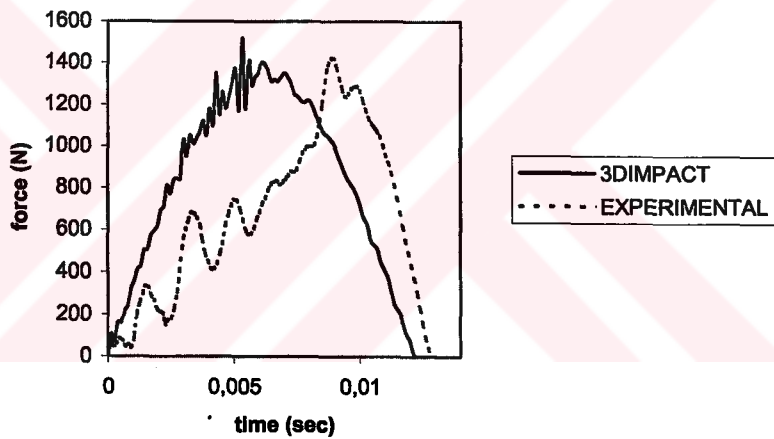

Figure 9.14 Impact force-time history of $(0^{0}/-45^{0}/45^{0})_{s}$ laminate under the impact velocity V=2 m/sec and impactor mass m=2600 g (150 mm by 150 mm).
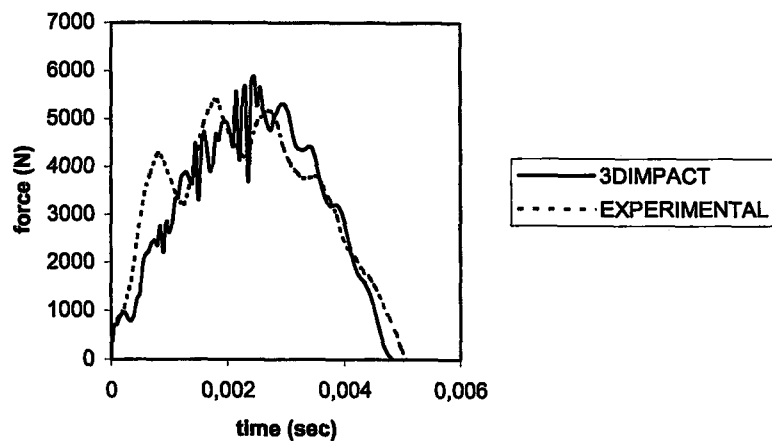
Figure 9.15 Impact force-time history of $(0^{0}/-45^{0}/45^{0})_{s}$ laminate under the impact velocity V=3 m/sec and impactor mass m=2600 g (150 mm by 150 mm).

Figure 9.16 Impact force-time history of $(0^0/-45^0/45^0)_s$ laminate under the impact velocity V=3 m/sec and impactor mass m=135 g (150 mm by 150 mm).
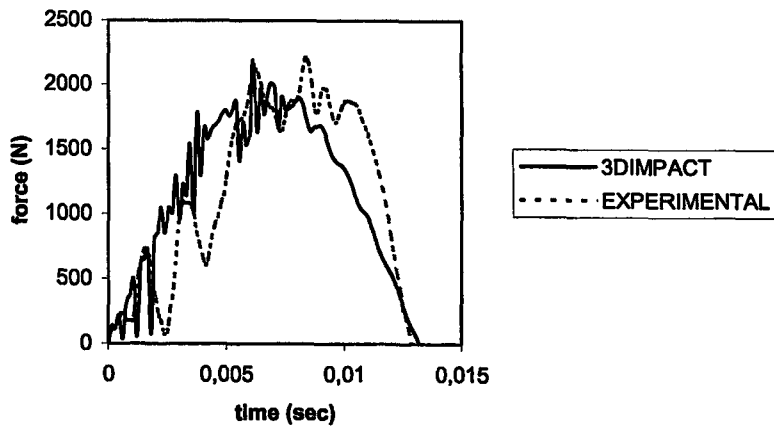

Figure 9.17 Impact force-time history of $(0^0/-45^0/45^0)_s$ laminate under the impact velocity V=1 m/sec and impactor mass m=2600 g (150 mm by 100 mm).
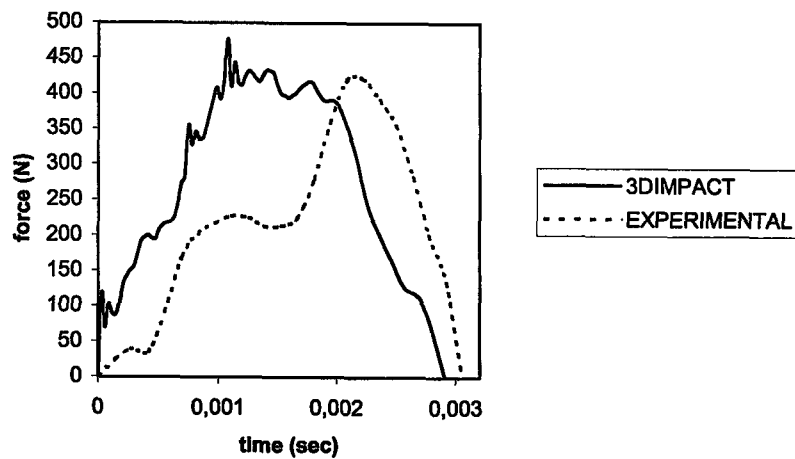

Figure 9.18 Impact force-time history of $(0^0/-45^0/45^0)_s$ laminate under the impact velocity V=2 m/sec and impactor mass m=2600 g (150 mm by 100 mm).
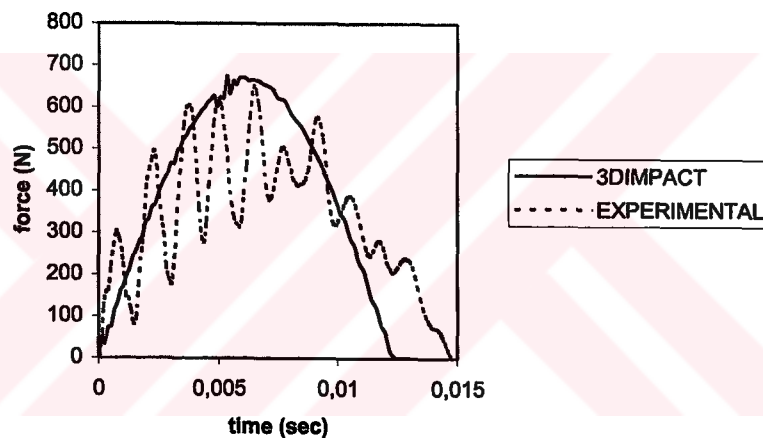
Figure 9.19 Impact force-time history of $(0^0/-45^0/45^0)_s$ laminate under the impact velocity V=3 m/sec and impactor mass m=2600 g (150 mm by 100 mm).
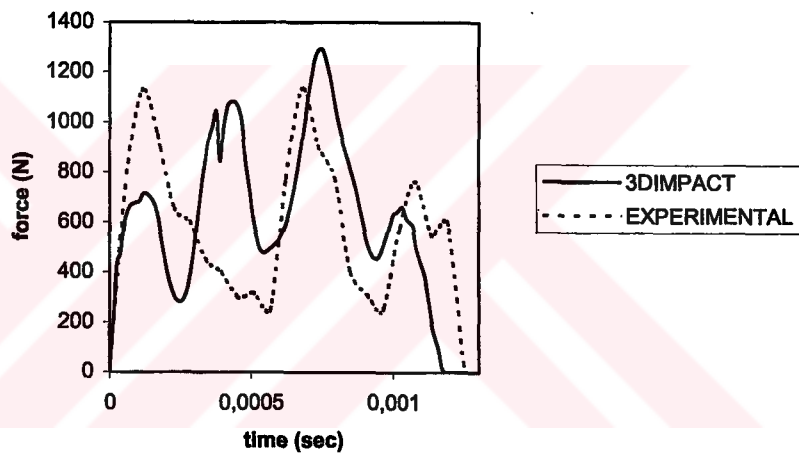
Figure 9.20 Impact force-time history of $(0^0/-45^0/45^0)_s$ laminate under the impact velocity V=3 m/sec and impactor mass m=135 g (150 mm by 100 mm).

Figure 9.21 Impact force-time history of $(0^0/-45^0/45^0)_s$ laminate under the impact velocity V=1 m/sec and impactor mass m=2600 g (150 mm by 50 mm).
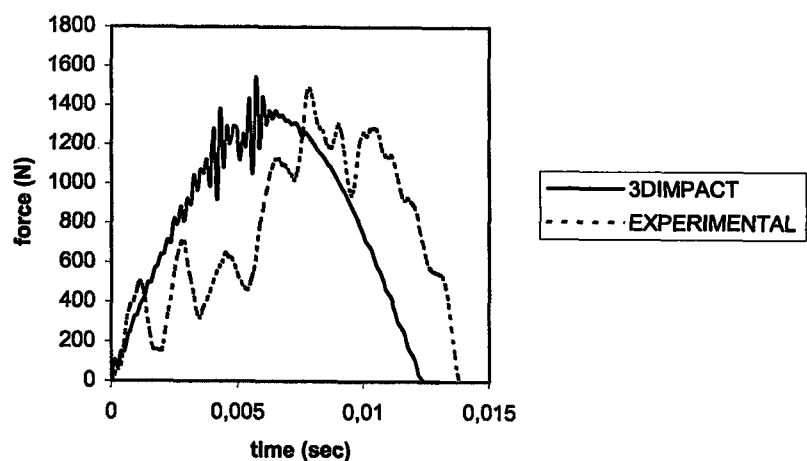
Figure 9.22 Impact force-time history of $(0^0/-45^0/45^0)_s$ laminate under the impact velocity V=2 m/sec and impactor mass m=2600 g (150 mm by 50 mm).
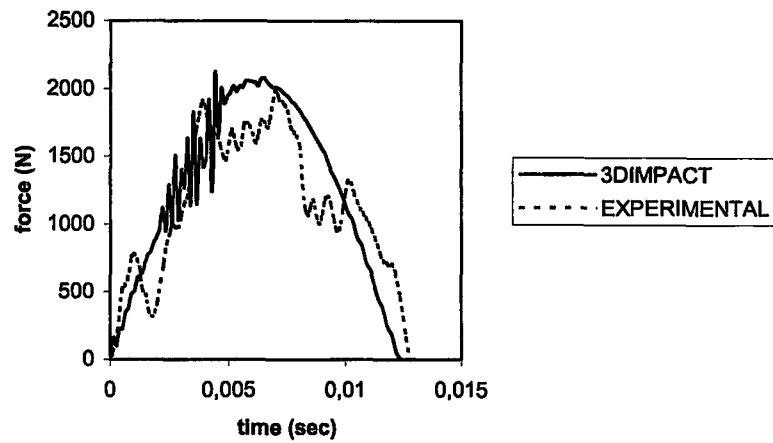

Figure 9.23 Impact force-time history of $(0^0/-45^0/45^0)_s$ laminate under the impact velocity V=3 m/sec and impactor mass m=2600 g (150 mm by 50 mm).

Figure 9.24 Impact force-time history of $(0^0/-45^0/45^0)_s$ laminate under the impact velocity V=3 m/sec and impactor mass m=135 g (150 mm by 50 mm).

9.3 Contact Force History of the Plate $(0^0,90^0)_6$ With Thickness 1.4 mm

Figure 9.25 Impact force-time history of $(0^0,90^0)_6$ laminate under the impact velocity V=1 m/sec and impactor mass m=2600 g (150 mm by 150 mm by 1.4 mm).
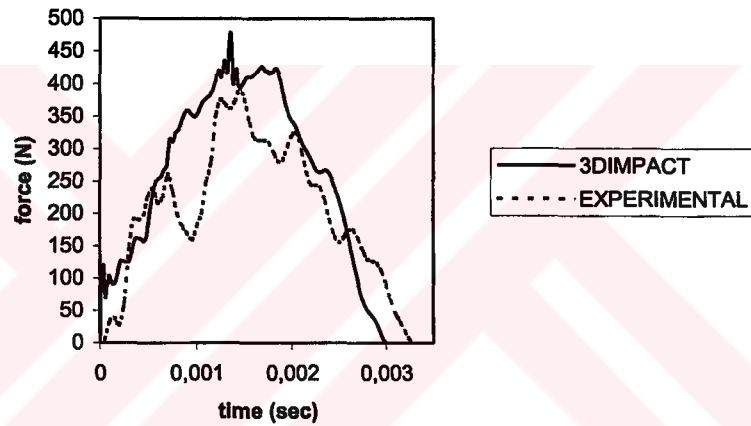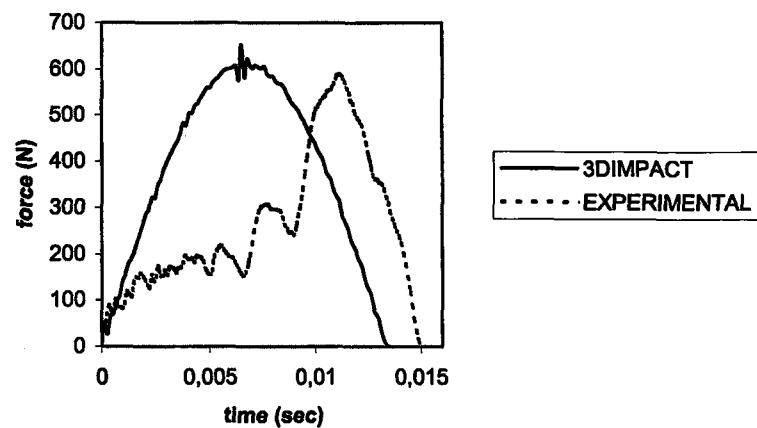
Figure 9.26 Impact force-time history of $(0^0,90^0)_6$ laminate under the impact velocity V=2 m/sec and impactor mass m=2600 g (150 mm by 150 mm by 1.4 mm).

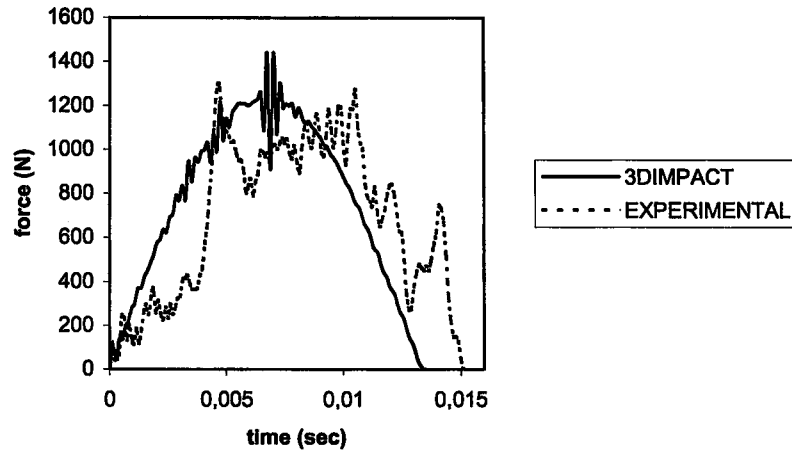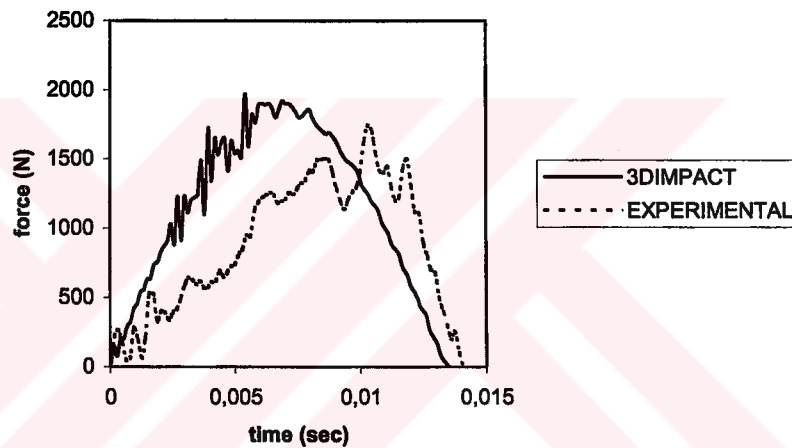**Figure 9.27** Impact force-time history of $(0^0,90^0)_6$ laminate under the impact velocity V=3 m/sec and impactor mass m=2600 g (150 mm by 150 mm by 1.4 mm).

Figure 9.28 Impact force-time history of $(0^0,90^0)_6$ laminate under the impact velocity V=3 m/sec and impactor mass m=135 g (150 mm by 150 mm by 1.4 mm).

Figure 9.29 Impact force-time history of $(0^0,90^0)_6$ laminate under the impact velocity V=1 m/sec and impactor mass m=2600 g (150 mm by 100 mm by 1.4 mm).

Figure 9.30 Impact force-time history of $(0^0,90^0)_6$ laminate under the impact velocity V=2 m/sec and impactor mass m=2600 g (150 mm by 100 mm by 1.4 mm).

Figure 9.31 Impact force-time history of $(0^0,90^0)_6$ laminate under the impact velocity V=3 m/sec and impactor mass m=2600 g (150 mm by 100 mm by 1.4 mm).
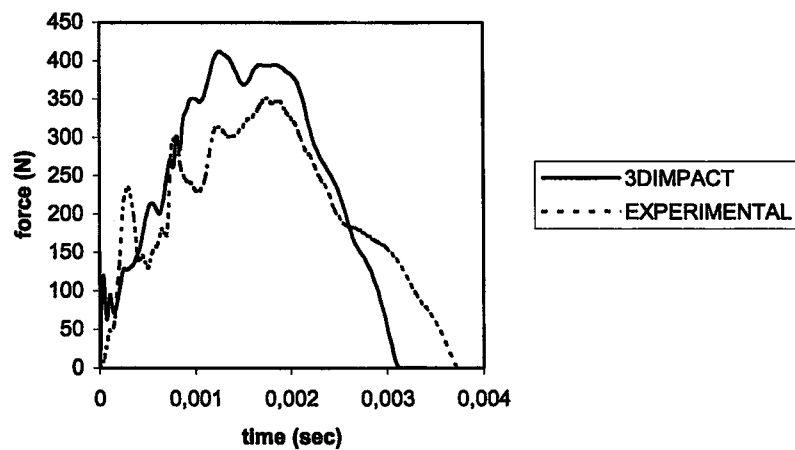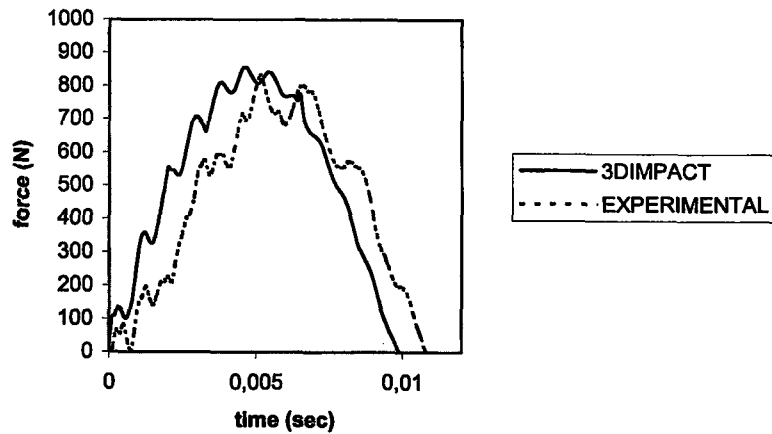

Figure 9.32 Impact force-time history of $(0^0,90^0)_6$ laminate under the impact velocity V=3 m/sec and impactor mass m=135 g (150 mm by 100 mm by 1.4 mm).

Figure 9.33 Impact force-time history of $(0^0,90^0)_6$ laminate under the impact velocity V=1 m/sec and impactor mass m=2600 g (150 mm by 50 mm by 1.4 mm).
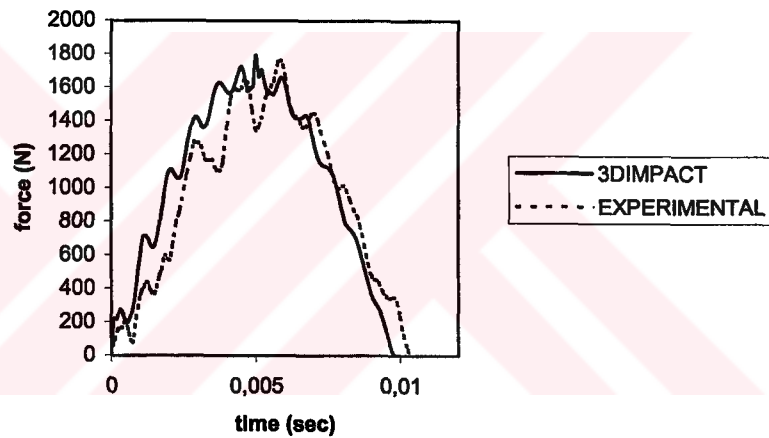
Figure 9.34 Impact force-time history of $(0^0,90^0)_6$ laminate under the impact velocity V=2 m/sec and impactor mass m=2600 g (150 mm by 50 mm by 1.4 mm).
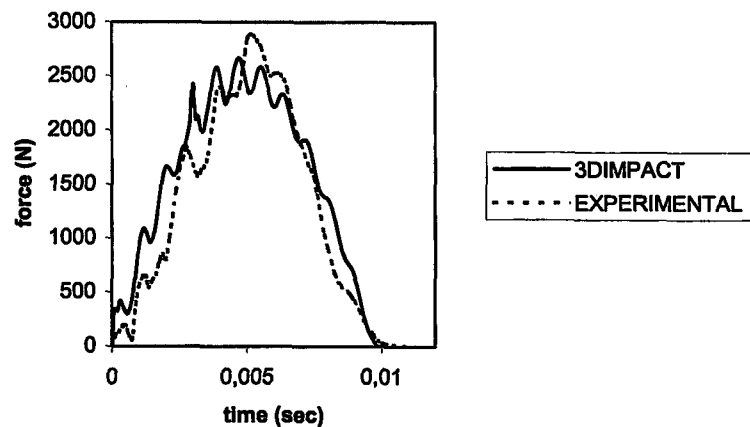

Figure 9.35 Impact force-time history of $(0^0,90^0)_6$ laminate under the impact velocity V=3 m/sec and impactor mass m=2600 g (150 mm by 50 mm by 1.4 mm).
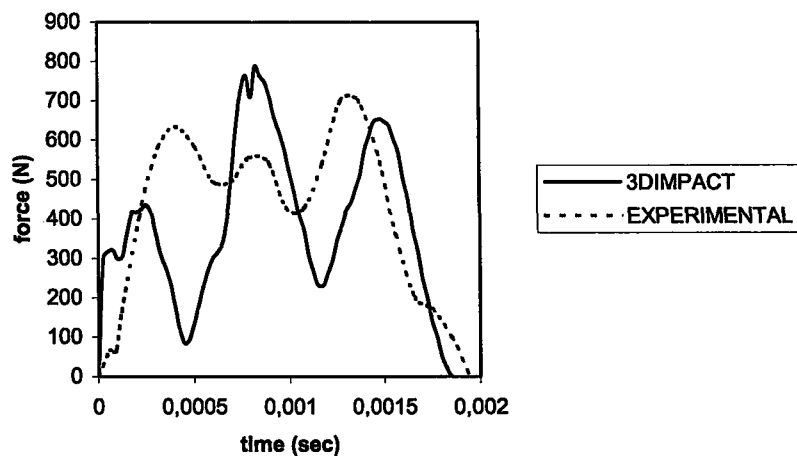

Figure 9.36 Impact force-time history of $(0^0,90^0)_6$ laminate under the impact velocity V=3 m/sec and impactor mass m=135 g (150 mm by 50 mm by 1.4 mm).

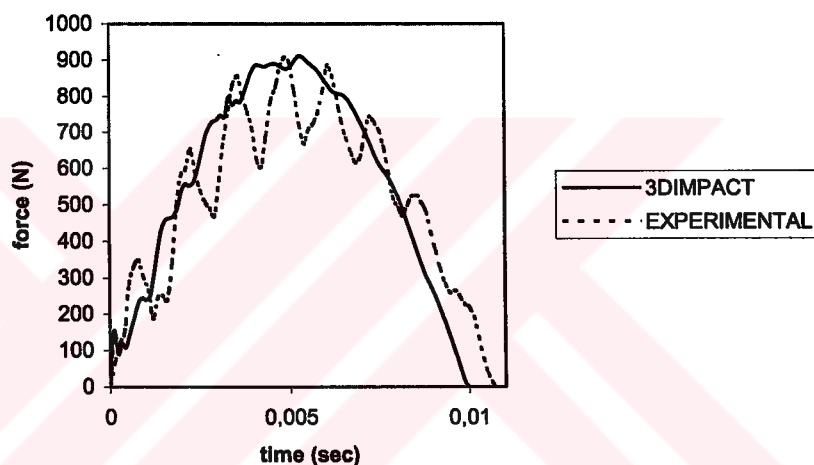## 9.4 Contact Force History of the Plate $(0^0,90^0)_6$ With Thickness 2.8 mm

Figure 9.37 Impact force-time history of $(0^0,90^0)_6$ laminate under the impact velocity V=1 m/sec and impactor mass m=2600 g (150 mm by 150 mm by 2.8 mm).

Figure 9.38 Impact force-time history of $(0^0,90^0)_6$ laminate under the impact velocity V=2 m/sec and impactor mass m=2600 g (150 mm by 150 mm by 2.8 mm).
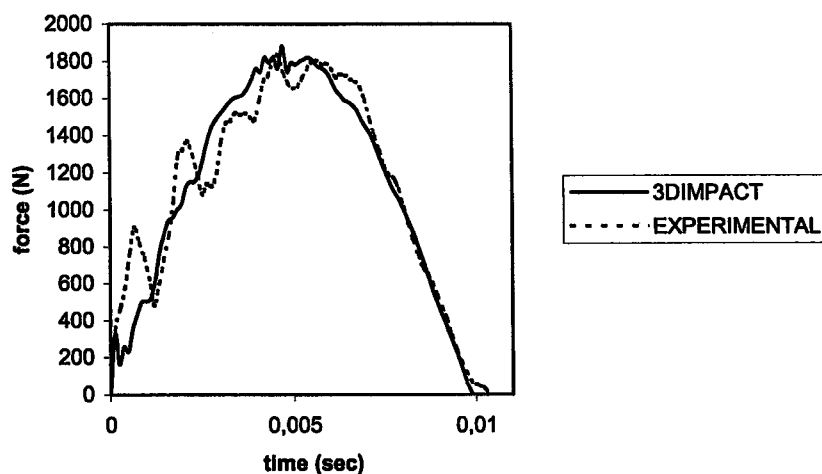

Figure 9.39 Impact force-time history of $(0^0,90^0)_6$ laminate under the impact velocity V=3 m/sec and impactor mass m=2600 g (150 mm by 150 mm by 2.8 mm).

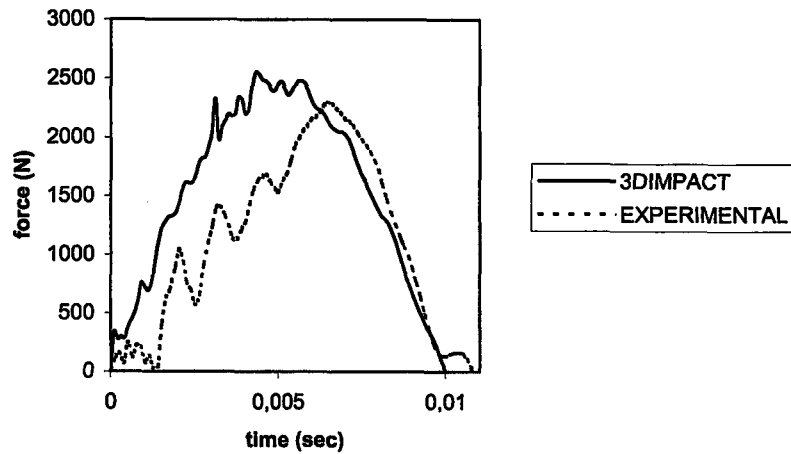**Figure 9.40** Impact force-time history of $(0^0,90^0)_6$ laminate under the impact velocity V=3 m/sec and impactor mass m=135 g (150 mm by 150 mm by 2.8 mm).

Figure 9.41 Impact force-time history of $(0^0,90^0)_6$ laminate under the impact velocity V=1 m/sec and impactor mass m=2600 g (150 mm by 100 mm by 2.8 mm).
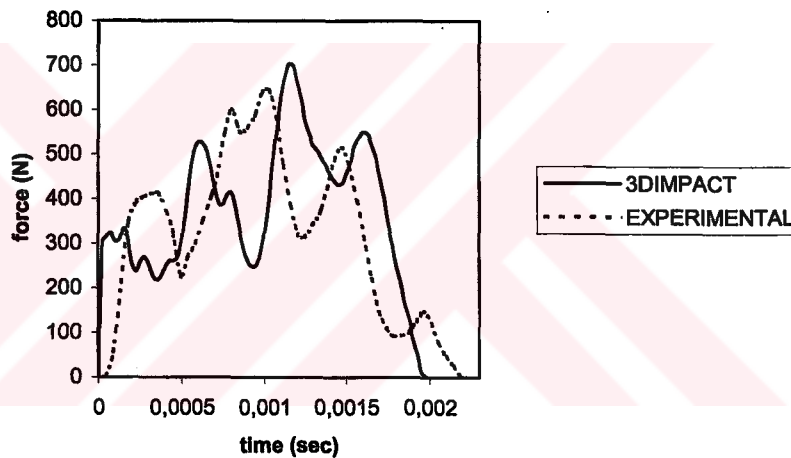

Figure 9.42 Impact force-time history of $(0^0,90^0)_6$ laminate under the impact velocity V=2 m/sec and impactor mass m=2600 g (150 mm by 100 mm by 2.8 mm).

Figure 9.43 Impact force-time history of $(0^0, 90^0)_6$ laminate under the impact velocity V=3 m/sec and impactor mass m=2600 g (150 mm by 100 mm by 2.8 mm).

Figure 9.44 Impact force-time history of $(0^0, 90^0)_6$ laminate under the impact velocity V=3 m/sec and impactor mass m=135 g (150 mm by 100 mm by 2.8 mm).
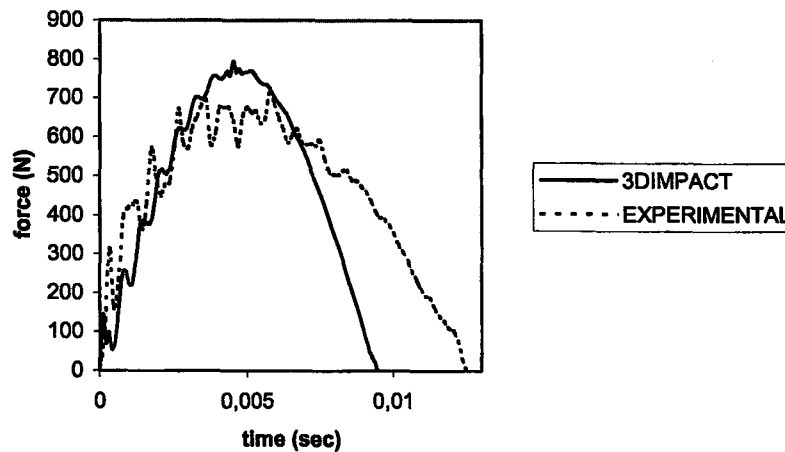

Figure 9.45 Impact force-time history of $(0^0, 90^0)_6$ laminate under the impact velocity V=1 m/sec and impactor mass m=2600 g (150 mm by 50 mm by 2.8 mm).
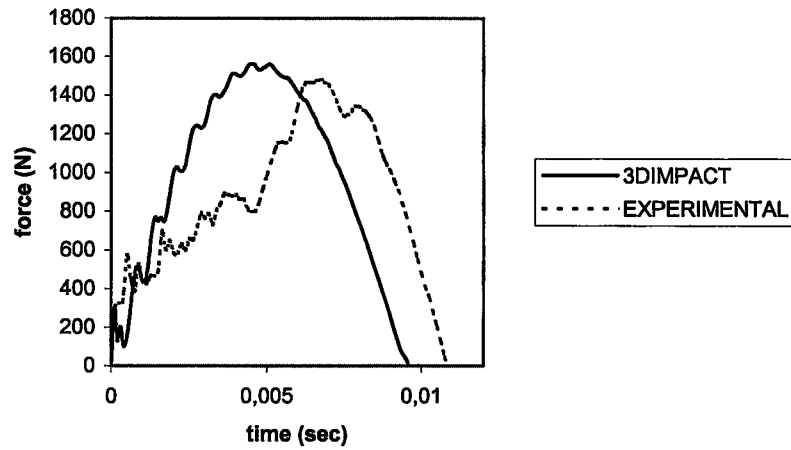
Figure 9.46 Impact force-time history of $(0^0,90^0)_6$ laminate under the impact velocity V=2 m/sec and impactor mass m=2600 g (150 mm by 50 mm by 2.8 mm).
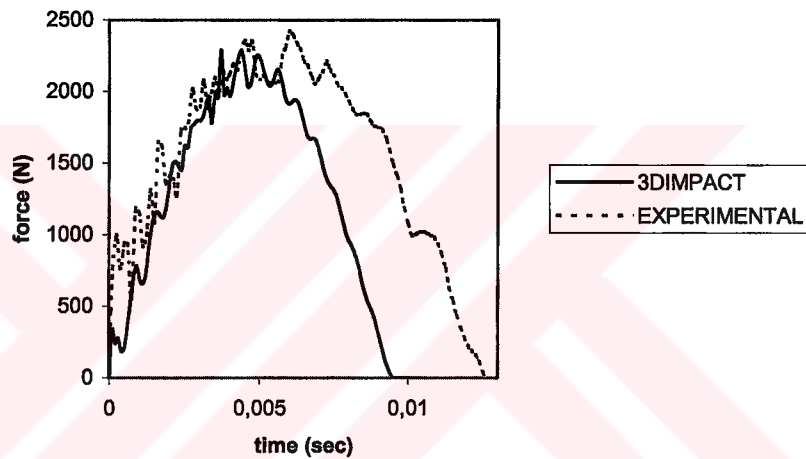

Figure 9.47 Impact force-time history of $(0^0,90^0)_6$ laminate under the impact velocity V=3 m/sec and impactor mass m=2600 g (150 mm by 50 mm by 2.8 mm).
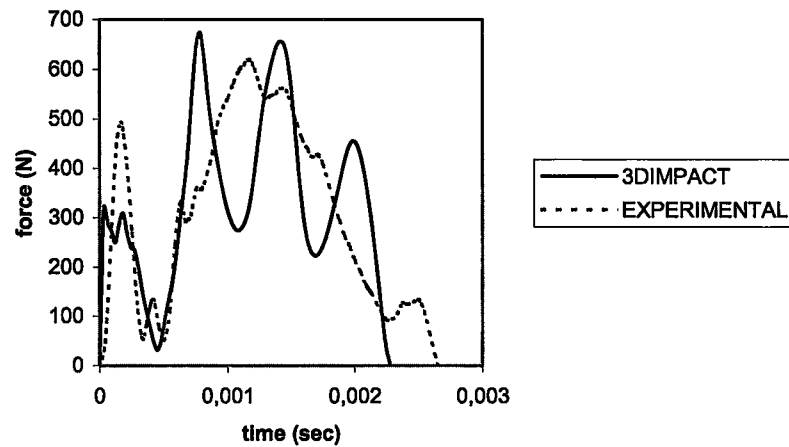

Figure 9.48 Impact force-time history of $(0^0,90^0)_6$ laminate under the impact velocity V=3 m/sec and impactor mass m=135 g (150 mm by 50 mm by 2.8 mm).